

# Dynamics of reaction fronts in porous media

**Paweł Kondratiuk**



**Institute of Theoretical Physics  
Faculty of Physics  
University of Warsaw**

A dissertation submitted to the University of Warsaw  
for the degree of Doctor of Philosophy  
under the supervision of Professor Piotr Szymczak

Warsaw, May 5, 2017



# Acknowledgements

First of all, I would like to express my sincere gratitude to my advisor, Professor Piotr Szymczak, for his support, advice, and extremely friendly attitude. I benefited a lot from his vast scientific expertise. Apart from that, I admire his ability to share his energy and passion with us, his students, which was very motivating and pushing forward.

The numerical part of the thesis could not have been accomplished without numerical codes prepared by Professor Anthony Ladd and his students, to whom I thank a lot. I also thank Prof. Ladd for his friendliness, advice, and fruitful collaboration, especially during his stays in Poland.

I thank all my colleagues, who were doing research in the group of Prof. Szymczak during my presence there: Hanna Trędak, Agnieszka Budek, Karine Petrus, Magdalena Gruzziel, Michał Pecelerowicz, Paweł Żuk, Florian Osselin, Kamil Kwiatkowski, and Filip Dutka. I think we learned a lot from each other.

I warmly thank my Parents for their constant support and emboldening my interest in science.

Last but not least, I owe my utmost gratitude to my wife Katarzyna for her love and support, and my daughter Julianna for being a charming little girl.

# Contents

<b>1</b>	<b>Introduction</b>	<b>3</b>
1.1	Motivation . . . . .	3
1.2	Structure of the thesis . . . . .	7
<b>2</b>	<b>General reactive-infiltration model</b>	<b>9</b>
2.1	Fluid flow through the porous matrix . . . . .	9
2.2	Transport of the aqueous species . . . . .	10
2.3	Evolution of the porous matrix . . . . .	11
2.4	Assumptions and simplifications of the model . . . . .	11
2.4.1	Time scale separation . . . . .	11
2.4.2	Dispersion . . . . .	11
2.4.3	Reaction kinetics . . . . .	12
<b>3</b>	<b>Reactive-infiltration instability in the thin front limit</b>	<b>15</b>
3.1	The infiltration-dissolution system . . . . .	15
3.2	Length scales in a stationary front . . . . .	17
3.3	Thin front approximation . . . . .	19
3.4	Scaling . . . . .	20
3.5	One-dimensional (planar) solutions . . . . .	22
3.6	Instability of the planar dissolution front . . . . .	22
<b>4</b>	<b>Onset of the competition between dissolution fingers</b>	<b>29</b>
<b>5</b>	<b>Nonlinear evolution of the dissolution system</b>	<b>35</b>
<b>6</b>	<b>Stationary dissolution forms</b>	<b>39</b>
6.1	Stationary dissolution fingers . . . . .	40
6.1.1	Two-dimensional stationary dissolution fingers . . . . .	40
6.1.2	Three-dimensional stationary dissolution fingers . . . . .	49
6.1.3	Natural solution pipes . . . . .	53
6.2	Stationary roots . . . . .	54
6.2.1	Two-dimensional stationary roots . . . . .	54
6.2.2	Three-dimensional stationary roots . . . . .	59
<b>7</b>	<b>Dynamics of dissolution-precipitation fronts</b>	<b>63</b>
7.1	Model . . . . .	63
7.2	Scaling . . . . .	65
7.3	One-dimensional solutions . . . . .	66
7.3.1	Mass balance . . . . .	66
7.3.2	Spatial invariants . . . . .	68
7.3.3	One-dimensional profiles . . . . .	70

7.4	Stability of stationary replacement fronts . . . . .	73
7.4.1	Dynamics of the perturbations . . . . .	73
7.4.2	LSA in the limit of negligible dispersion . . . . .	75
7.4.3	LSA in the limit of quick dissolution . . . . .	84
7.5	Analogy to multilayer viscous fingering . . . . .	92
<b>8</b>	<b>Nonlinear evolution of the replacement system</b>	<b>95</b>
8.1	Numerical simulations . . . . .	95
8.2	Comparison with natural patterns . . . . .	98
<b>9</b>	<b>Summary</b>	<b>105</b>
<b>A</b>	<b>Spectral method</b>	<b>115</b>

# Chapter 1

## Introduction

### 1.1 Motivation

Patterns observed in nature frequently originate from instabilities. For example, the Rayleigh-Bénard instability initiates convection cells in a fluid film heated from below. The Kelvin-Helmholtz instability is responsible for the formation of ocean waves and curly clouds at the boundary between two layers of air moving with different velocities, and can be experienced as turbulence during an aircraft flight. Two remarkable examples of the Kelvin-Helmholtz instability can be observed in Fig. 1.1. On the left panel of Fig. 1.1, the instability developed in the atmosphere of the planet Jupiter, at the boundary between its two bands. On the right panel, one can see a similar curly pattern “frozen” in a rock. It is interpreted as a trace of a Kelvin-Helmholtz instability, which occurred after a seismic event in the early stages of diagenesis, when the rock was not yet consolidated [1]. Note that a similar pattern was also preserved in the younger layers of the rock, which suggests that the event which caused the pattern formation reoccurred (although probably with a smaller magnitude). The Saffman-Taylor instability is another remarkable example of an instability. It occurs whenever a less viscous fluid is pushed to replace a more viscous one. As a consequence of this instability, the boundary between the fluid first becomes wavy, and later “fingers” of the less viscous fluid grow and gradually reach further and further into the body of the more viscous fluid. The phenomenon is unwelcome to petroleum engineers, who pump water into oil-bearing reservoirs in order to extract hydrocarbons. A regular water-oil front can only be obtained if some additional substances (e.g. polycarbonates) are added to the water. The mixture is then more viscous than oil, which prevents the Saffman-Taylor instability to occur. Otherwise the front would soon get perturbed and a finger of water would penetrate to the outlet well, leaving the oil behind.

Most of the patterns which arise as a consequence of instabilities cease to exist soon after the driving force disappears. Geological systems are notable exceptions, since the pattern carved in rocks can persist even for millions of years [2, 3]. On the other hand, geological processes often occur on extremely long time scales, and the ongoing evolution of the patterns cannot be directly observed. Some notable examples of geological patterns which are believed to have been formed due to symmetry-breaking instabilities and self-organization are travertine terraces (Fig. 1.2), crystal dendrites (Fig. 1.3), or solution pipes (Fig. 1.4).

Solution pipes, which belong to a wider class of karst forms, are of our specific interest. The formation of solution pipes is an example of a wide range of symmetry-breaking phenomena driven by couplings between fluid infiltration, ion transport in the groundwater flow, and chemical transformation of the rock. Whenever groundwater is out of equilibrium with the porous rocks it is infiltrating, dissolution and precipitation can take place in the pore space. As a result, the chemical composition and morphology of the rock might undergo significant changes, up to



Figure 1.1: (Left) A Kelvin-Helmholtz instability in the atmosphere of Jupiter. Source: Wikimedia Commons. (Right) Dislocated layers of a sedimentary rock in the Lisan Formation, Israel. The pattern is interpreted as a result of a Kelvin-Helmholtz instability. The height of the rock formation presented in the image is 2-3 m. Photo: Author.



Figure 1.2: Travertine terraces in Pamukkale, southern Turkey. The terraces were formed as a result of precipitation of travertine, a calcium carbonate mineral, from hot springs [3]. Source: Wikimedia Commons.

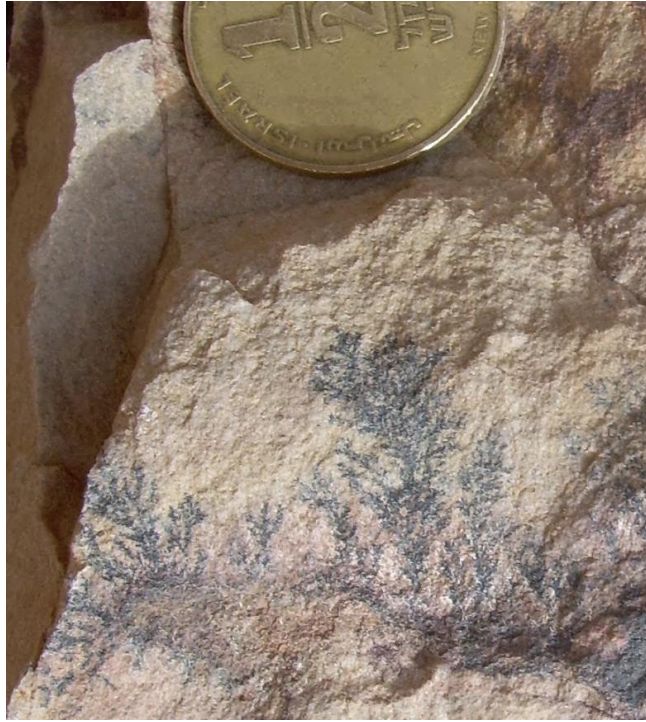


Figure 1.3: A crystal dendrite on an exposed fracture wall. The coin illustrates the scale of the pattern. Photo: Author.

the complete replacement of the parent (primary) rock by a product (secondary) one. Among numerous natural examples of such transformations are dolomitization [7], serpentine carbonation [8], albitization [9] and feldspar alteration [10]. Fluid-mediated replacement reactions have also been studied in the laboratory, although most of the experiments were conducted in the absence of the flow [9].

The replacement of one rock by another one is not instantaneous. Instead, reaction fronts form. These are regions of increased chemical activity, separating the secondary and the primary phase. Reaction fronts propagate in the direction of the flow, but with much lower velocity than that of the infiltrating water [11, 12, 13]. This time scale separation is due to the large molar concentration difference between ions in the fluid phase and the consolidated material in the solid phase.

When the secondary phase is more permeable than the primary phase, reaction fronts are inherently unstable. Even if the reaction front is initially planar, soon small perturbations, which absorb more flow, emerge and grow into finger-like or funnel-like structures. These structures go under various names: “dissolution fingers”, “wormholes”, or “solution pipes” [14, 15, 4]. The mechanism of their formation is referred to in the literature as the *reactive-infiltration instability* [16]. Arguably the most famous example of such a process is the dissolution of a carbonate matrix by an incoming acidic solution, giving rise to a rich variety of karstic forms [17, 18]. However, the opposite situation can also occur, when precipitation of minerals from ions present in the infiltrating fluid decreases the porosity of the rock. In this case the reaction front is stabilized by the permeability decrease [19] and any protrusions in the front get flattened out.

Due to the complex, nonlinear nature of reactive-infiltration processes, analytical results in this field are rather limited. They were focused either on analysis of morphology of one-dimensional reaction fronts [20, 21], or performing linear stability analysis of the fronts, but in the simplest case of a single-component dissolution system [16, 22]. This thesis aims to partly fill this gap by providing strict analytical results beyond these simplest cases.

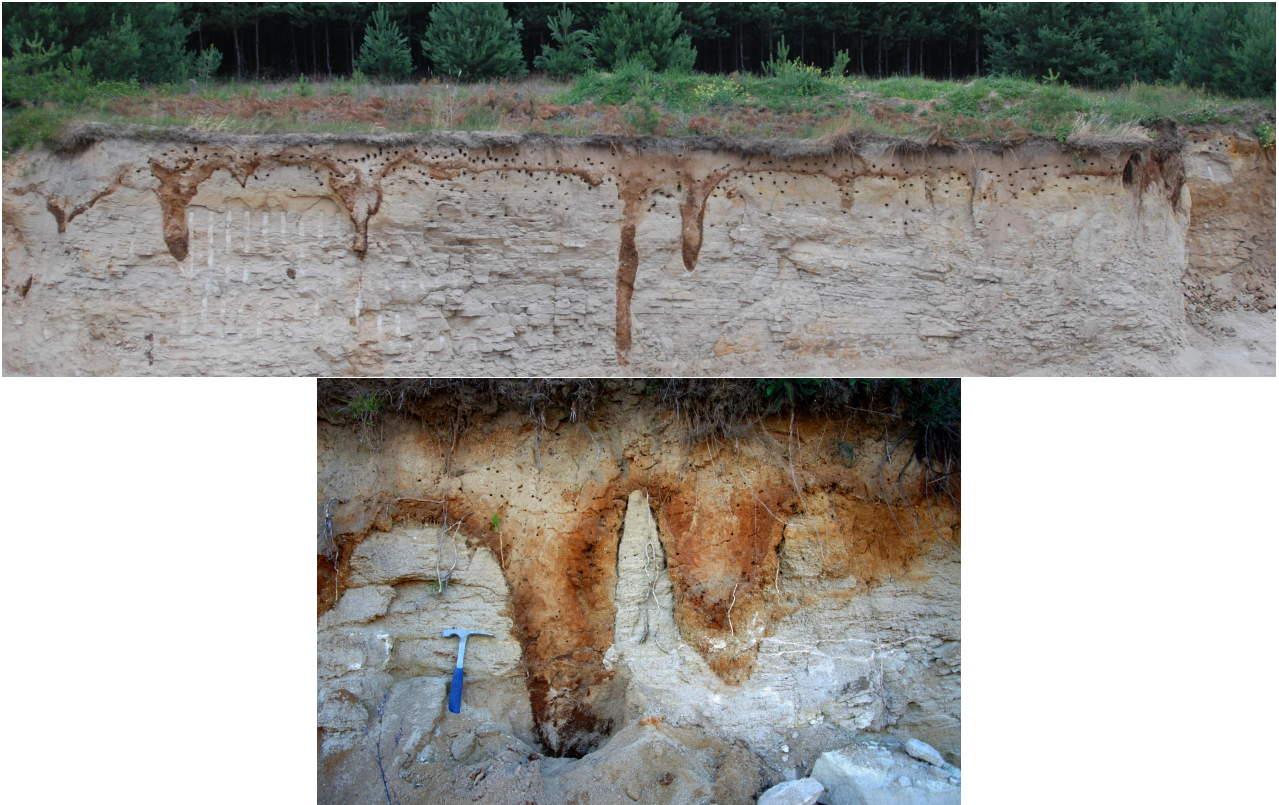


Figure 1.4: (Top) An array of solution pipes in limestone bedrock near Smerdyna (Poland). They are postulated to have been formed by a dissolving action of meltwater during Elsterian deglaciation [4, 5]. The brown rims in the clay filling the pipes are formed as a result of clay and iron oxide accumulation due to the illuviation processes [6]. The clay particles are transferred by water from the upper parts of the soil and then flocculate at the clay-limestone boundary, where the pH changes from mildly acidic to alkaline. The photo is courtesy of dr Łukasz Użarówicz, SGGW. (Bottom) Two solution pipes of a regular, parabolic shape. The length scale is provided by the hammer. The photo is courtesy of prof. Piotr Szymczak, UW.

## 1.2 Structure of the thesis

The thesis is organized as follows. In Chapter 2, we introduce a general large-scale reactive-infiltration model, which will serve as the starting point for the further analysis. In Chapter 3 we derive some classic results of the reactive-infiltration instability, studying linear stability of a thin planar dissolution front. Chapter 3 serves also as an introduction to our own results, which are presented in the subsequent part of the thesis. In Chapter 4 we go beyond linear stability, studying the onset of nonlinear competition between spontaneously developing corrugations in a dissolution front. Chapter 5 presents a typical nonlinear evolution of a single-component reactive-infiltration system. In Chapter 6 asymptotic nonlinear dissolution forms are studied. Chapter 7 is devoted to the dynamics of dissolution-precipitation fronts. Here we study the morphology of planar replacement fronts, and then their stability. Next, in Chapter 8, nonlinear replacement dynamics is studied by numerical simulations. Finally, a summary of the thesis is given in Chapter 9.



# Chapter 2

## General reactive-infiltration model

In the current chapter the model will be introduced, which aims to capture three basic components of the reactive infiltration system — fluid flow, transport of aqueous species, and the porous matrix evolution — as well as couplings between these three phenomena. The length scales considered in this model are much larger than the typical sizes of the pores, which justifies the adoption of the continuum approach: all the physical fields (such as the the Darcy velocity, the matrix porosity, or concentrations of the aqueous species) are treated as continuous fields and represented by continuous functions of both position  $\mathbf{r}$  and time  $t$ .

### 2.1 Fluid flow through the porous matrix

If at least some part of the pore voids are interconnected, the porous rock can be infiltrated by groundwater. In our model we assume that all the pores of the matrix are interconnected and that they are completely filled with the (moving) fluid. Another assumption, of the incompressibility of the fluid, yields the continuity equation which couples the porosity  $\varphi(\mathbf{r}, t)$  with the volumetric Darcy velocity  $\mathbf{u}(\mathbf{r}, t)$ ,

$$\frac{\partial \varphi}{\partial t} + \nabla \cdot \mathbf{u} = 0. \quad (2.1)$$

The fluid flow is driven by the externally imposed pressure difference. The relationship between the Darcy velocity and the pressure gradient over length scales larger than the characteristic pore sizes is given by the celebrated Darcy’s law [23], which states that the fluid flux density is proportional to the pressure gradient,

$$\mathbf{u} = -\frac{K}{\mu} \nabla p. \quad (2.2)$$

In fact,  $\mathbf{u}$  is often referred to as the “Darcy velocity” or the “superficial velocity” in the context of groundwater flow. The proportionality coefficient is the ratio between the porous matrix permeability  $K = K(\mathbf{r}, t)$  and dynamic viscosity of the fluid  $\mu$ . The viscosity of the fluid is assumed to be constant in our model. The law was discovered by Henry Darcy experimentally, but can also be derived from the Navier-Stokes equations, assuming that the flow is incompressible, stationary, and creeping, and that the resisting viscous force is linear in the mean fluid velocity within the pores [24, 25, 26].

The permeability  $K$  is a function of the local properties of the porous matrix. In general it is a tensor field, which may account for anisotropy in rocks (e.g. layering). In our model porosity is the only field which bears information about the local structure of the matrix. Therefore the permeability is assumed to be a scalar field related to the porosity,  $K(\mathbf{r}, t) = K(\varphi(\mathbf{r}, t))$ . There is no universal relationship between the matrix porosity and its permeability. The latter

depends on the type of the rock, mainly through the structure of the pore network. It is however natural to expect that  $K$  should be an increasing function of  $\varphi$ <sup>1</sup>. One of the most common models of permeability is the Kozeny equation [26]. In his theory, Kozeny modeled the porous medium as a bundle of capillary tubes of equal length [28]. After solving the Navier-Stokes equations for such a system, he derived the following expression for permeability:

$$K(\varphi) = \frac{c_0 \varphi^3}{s^2}. \quad (2.3)$$

In the above,  $s$  is the specific surface area (i.e. surface area per a unit volume of the rock), and  $c_0$  is a dimensionless factor which accounts for the structure of the pore network. In this thesis two models of the porosity-permeability relation will be utilized. Assuming that the specific surface area  $s$  is constant, the Kozeny equation (2.3) simplifies to the cubic permeability model,

$$K(\varphi) = K_1 \varphi^3. \quad (2.4)$$

The second porosity-permeability relation will be the the exponential model,

$$K(\varphi) = K_0 e^{V\varphi}, \quad (2.5)$$

which is sometimes used to model hydraulic properties of rocks that are partly soluble [29]. In sandstones, for instance, insoluble grains (typically composed of quartz or feldspar) are often binded together by soluble carbonate cement. Dissolution of the cement hardly changes the porosity of the rock, but its permeability increases significantly. Such a strong response of permeability to porosity changes is well represented by the exponential relation (2.5).

## 2.2 Transport of the aqueous species

In an unconfined flow the aqueous species (typically ions) are transported in the flow both by advection and diffusion. As regards the flow in the pore network, similar transport mechanisms occur. However, the microscopic diffusion is enhanced due to the fact that in the pore network there always exists a number of distinct paths which a single ion can pass through while being transported by the flow [30]. The term “dispersion” was coined to refer to such a mechanism. In general the dispersion coefficient is a tensor depending on the porosity and the fluid flow [31, 30, 26]. Since the chemical reactions occur in porous reservoirs, the continuity equation for the concentration of each species,  $c_i$ , is

$$\frac{\partial(\varphi c_i)}{\partial t} + \nabla \cdot (\mathbf{u} c_i - \underline{\underline{\mathbf{D}}} \nabla c_i) = - \sum_j n_{ij} r_j, \quad (2.6)$$

where  $\underline{\underline{\mathbf{D}}} = \underline{\underline{\mathbf{D}}}(\varphi, \mathbf{u})$  is the dispersion tensor, and the right-hand side represents the reaction terms:  $n_{ij}$ 's are stoichiometric coefficients, while  $r_j = r_j(\{c_k\}, \{v_k\})$  denotes the speed of the  $j$ th reaction (in moles per unit time and per unit volume of the rock), which in general depends on the concentrations of all the aqueous species  $c_k$  and on the volume fractions of the solid phases (minerals)  $v_k$ . The sign convention is such that a “positive” reaction depletes the fluid from the respective species.

---

<sup>1</sup>However, some (rather exotic) counterexamples can be found. Acidic water flushing of fractured argillaceous limestone causes its permeability reduction, despite the fact that the porosity of the sample increases [27]. Apart from carbonates, the rock is composed of a significant (> 20%) amount of clay minerals. The reason of the counterintuitive permeability behaviour is reorganization and localized accumulation of weakly soluble clay particles in the fractures.

## 2.3 Evolution of the porous matrix

The primary porous rock is constituted of a number of minerals, each one occupying some volume fraction  $v_j$ . Obviously, the volume fractions of all the minerals and the porosity should sum up to unity,

$$\sum_i v_i + \varphi = 1. \quad (2.7)$$

As the reactive infiltration proceeds, the chemical reactions transform the porous matrix by dissolving or precipitating minerals. As a result, the volume fractions evolve as

$$\frac{\partial v_i}{\partial t} = n_i \nu_i r_i, \quad (2.8)$$

where  $\nu_i$  is the molar volume of the  $i$ th mineral, and  $n_i$  is the relevant (possibly negative) stoichiometric coefficient. Since (2.7) is satisfied at any time, the evolution of the mineral volume fractions leads to porosity changes.

## 2.4 Assumptions and simplifications of the model

The model presented in Secs. (2.1–2.3) has been posed as quite general. In the current section we introduce some further simplifying assumptions.

### 2.4.1 Time scale separation

The time derivatives occur both in the transport equations (2.6) and in the mineral composition evolution equations (2.8). We are interested in time scales  $T_v$  which are associated with the solid phase evolution,

$$T_v \sim \frac{|v|}{|n||\nu||r|}. \quad (2.9)$$

In the above,  $|x|$  denotes the characteristic values of quantity  $x$ . In fact, the volume fractions  $v_i$  and the stoichiometric coefficients  $n_i$  are of the order of one,  $|v| \sim |n| \sim 1$ , so

$$T_v \sim \frac{1}{|\nu||r|}. \quad (2.10)$$

After a simple scale analysis of Eq. (2.6) one reveals that the term with the time derivative,  $\partial_t(\varphi c_i)$ , is smaller than the reaction term by a factor  $(|\varphi||\nu||c|)^{-1} \sim (|\nu||c|)^{-1}$ . In other words, the time scale at which the concentration converges to a steady state,  $T_c$ , is  $(|\nu||c|)^{-1}$  times smaller than the time scale of the solid phase evolution  $T_v$ . The product  $|\nu||c|$  is small in typical geochemical conditions. For instance, the molar volume of calcite is  $31.20 \text{ cm}^3/\text{mol}$ , while the equilibrium concentration of  $\text{Ca}^{2+}$  during dissolution of calcite by meteoric water at  $25^\circ\text{C}$  is approx.  $5 \cdot 10^{-4} \text{ mol/L}$ , which eventually sets the time scale ratio  $T_c/T_v \sim 2 \cdot 10^{-5}$ .

Similar reasoning applies to the time derivative of the porosity in the fluid continuity equation (2.1). Consequently, the longest time scale is the one corresponding to the porous matrix evolution. Since this is the time scale of our interest, we can neglect the time derivatives in (2.1) and (2.6). From now on, stationarity of these continuity equations will be assumed.

### 2.4.2 Dispersion

The tensor form of the dispersion coefficient accounts for the fact that the dispersive transport might be anisotropic either due to the porous rock anisotropy, or the symmetry violation due

to the flow [32]. Here we disregard the dependence of the dispersion on the flow, and further assuming the isotropy of the medium, reduce the tensor to the scalar,

$$\underline{\underline{\mathbf{D}}}(\varphi, \mathbf{u}) \approx D(\varphi)\mathbb{I}, \quad (2.11)$$

where  $\mathbb{I}$  is a  $3 \times 3$  unit tensor. In the first approximation, such a scalar dispersion coefficient is a product of porosity and molecular diffusivity,  $D = \varphi D_{mol}$  [32]. Thus further on we shall loosen our naming convention and use the terms “dispersion” and “diffusion” interchangeably when referring to the same transport mechanism. Such a convention will be particularly useful in Sec. 3.6 and in Chapter 7, where the word “dispersion” will have to be used in a completely different context of “dispersion curves”.

### 2.4.3 Reaction kinetics

So far we have not proposed any specific form of the reaction kinetics functions,  $r_i = r_i(\{c_k\}, \{v_k\})$ . One of the most successful theories of reaction kinetics was developed by Lasaga and co-workers [33, 34]. The key point is the assumption that the rate of a chemical reaction depends on the extent of supersaturation (or undersaturation). For instance, in case of a single-reaction system, a general form of the reaction rate is

$$\frac{dm}{dt} = -sAe^{-E/(RT)}f(\{a_i\})g(\Delta G_r). \quad (2.12)$$

In the above, we have adapted the notation from Ref. [35]:  $dm/dt$  is the reaction rate (mol/s),  $s$  is the surface area ( $\text{m}^2$ ),  $A$  is the Arrhenius pre-exponential factor ( $\text{mol}/(\text{m}^2 \cdot \text{s})$ ),  $E$  is the activation energy (J/mol),  $T$  is the temperature (K),  $R \approx 8.31$  J/(mol·K) is the gas constant,  $f$  is a function of activities of the ions participating in the reaction, and  $g$  is a dimensionless function of the Gibbs free energy difference between the current state and the equilibrium state. Typically  $f$  is assumed to be a product of the activities,

$$f(\{a_i\}) = \prod_i a_i^{n_i}; \quad (2.13)$$

$g$  is expressed in terms of the saturation index  $\Omega$ ,

$$g(\Delta G_r) = (1 - \Omega^{p_i})^{q_i}, \quad (2.14)$$

where  $p_i$ ,  $q_i$  are fitting parameters; and the saturation index itself is the ratio of the activity product and the chemical equilibrium constant.

However, even in laboratory experiments it is often difficult to measure the reaction rate and find the fitting parameters. Sometimes the values reported in the literature can vary significantly, even by a few orders of magnitude (compare, for instance, the data for gypsum dissolution in Refs. [36] and [37]). Another issue is that dissolution and precipitation are often surface processes and the (effective) specific surface area of the porous medium has to be taken into account [38]. Alas, this quantity is quite difficult to measure. In fact, the surface of a porous mater can be self-similar (fractal) across a few orders of magnitude and thus the reactive surface area itself might be ill-defined for a certain class of natural porous materials.

In order to bypass these apparent difficulties, scientists working on reactive flows in porous media and related topics often take the reductionist approach and propose simple, yet at least qualitatively reasonable models of chemical kinetics [34]. Chemical reaction rates are often supposed to depend on the concentration of one species only. The assumption is justified whenever one of the reactions is significantly slower than the others and its rate limits the rate of the overall process [39]. Moreover, the reaction kinetics is often approximated by a linear

or power function [40]. On the other hand, experimental measurements suggest that some chemical reactions, such as dissolution of pure gypsum by distilled water, in fact do follow linear or power-law kinetics [34, 36, 37, 41].

Luckily, the problem of choosing the appropriate reaction kinetics model becomes in some cases irrelevant. In the case of reactive flows, one can assume that the fluid, which is initially in chemical equilibrium with a rock it is flushing through, instantaneously equilibrates with the other one once passing the boundary between these two porous media. Consequently, all the chemical activity is concentrated in an infinitely thin reaction front, which is the surface between the two porous rocks. The velocity of the reaction front can then be found from the mass balance between the incoming and outgoing ions. Such an approach, dubbed the thin-front approximation, is justified if the length scales of interest are significantly larger than the thickness(es) of the reaction front(s) (which are closely related to the penetration lengths of the relevant species transported in the flow [42]).

In Chapters 3–6 of this thesis the thin front approximation is applied. Then, in Chapter 7, linear kinetics models are utilized.



# Chapter 3

## Reactive-infiltration instability in the thin front limit

The simplest and classical example of the reactive-infiltration system has only one chemical reaction. One of the minerals in the primary rock undergoes dissolution by a single reactant brought by the flow. Such a system has been proved to exhibit a certain type of instability, dubbed the “reactive-infiltration instability” — an infinitely wide planar dissolution front is always unstable with respect to its arbitrarily small perturbation. The instability leads to the spontaneous front breakup and, in the next stages of the evolution, to the formation of highly-porous channels, which serve as dominant flow paths. Since the pioneering work of Chadam et al. [43], the reactive-infiltration instability has been studied by a number of authors [16, 22, 40]. In this chapter we briefly discuss the most important results of the theory, derived previously by other authors. We concentrate on the thin-front limit, since it will be relevant for the next three chapters.

### 3.1 The infiltration-dissolution system

Figure 3.1 schematically presents our system of interest: a porous rock being gradually dissolved by a solvent brought by groundwater flow. Let us briefly recall the model of such a system, discussed in more detail previously. The groundwater flow is governed by the Darcy’s law,

$$\mathbf{u} = -\frac{K(\varphi)}{\mu} \nabla p, \quad (3.1)$$

where  $\mathbf{u}$  is the Darcy velocity (i.e. the volumetric fluid flux density),  $K = K(\varphi)$  is the rock permeability,  $\mu = \text{const}$  is the fluid viscosity, and  $p$  is the fluid pressure. As argued in Sec. 2.4, to a good approximation the Darcy velocity is a sourceless field,

$$\nabla \cdot \mathbf{u} = 0. \quad (3.2)$$

Only one chemical reaction occurs in the system: primary mineral  $M_P$  is dissolved by the incoming reactant  $X$ ,



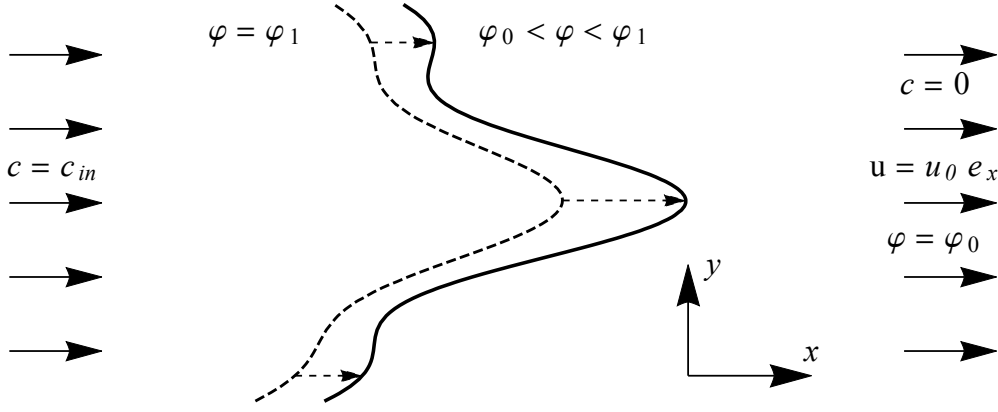


Figure 3.1: Geometry of the system: a reactive fluid is injected from the left side and dissolves the porous matrix through chemical reactions. The reaction front separates the dissolved, upstream domain of porosity  $\varphi_1$  and the partly dissolved, downstream domain of a varying porosity  $\varphi$  ( $\varphi_0 < \varphi < \varphi_1$ ). As time proceeds, the reaction front migrates, which is schematically represented by the transition from the dashed-line domain boundary to the solid-line boundary.

In the above,  $n$  is a stoichiometric coefficient and  $A_P$  represents the products of the reaction<sup>1</sup>. We assume that the reaction rate is independent from the concentration of  $A_P$ , and track the reactant  $X$  only. Its concentration will be denoted by  $c$ . The transport of the reactant is described by the advection-dispersion-reaction equation

$$\nabla \cdot (\mathbf{u}c - D(\varphi)\nabla c) = -nr(c, \varphi), \quad (3.6)$$

where  $D = D(\varphi)$  is the scalar dispersion coefficient. The solid phase content in the rock decreases as the soluble mineral undergoes dissolution,

$$\frac{\partial v}{\partial t} = -\frac{\partial \varphi}{\partial t} = -\nu r(c, \varphi), \quad (3.7)$$

where  $\nu$  is the molar volume of the soluble mineral.

As discussed in Sec. 2.4.3, a choice of an appropriate model of chemical kinetics,  $r(c, \varphi)$ , is a highly nontrivial task. For simplicity, let us choose a model, in which the dissolution is a first order reaction:  $r \propto c$ . Additionally, the reaction ceases when there is no soluble material (i.e. when porosity is maximal). The simplest model which has both of these features is

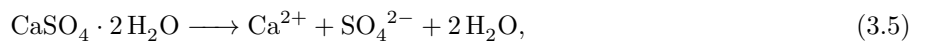
$$r = \alpha c \Theta(v) = \alpha c \Theta(\varphi_1 - \varphi), \quad (3.8)$$

where  $\alpha$  is the kinetic constant and  $\Theta$  is the Heaviside step function. Dissolution is a surface process, but the specific surface area  $s$  is assumed to be constant and is incorporated into  $\alpha$ . This assumption is coherent with the previously made assumption that the surface area is constant, which led to the simplification of the Kozeny equation (2.3) to the cubic porosity-permeability relation (2.4). Nevertheless, one should bear in mind that it is a simplification.

<sup>1</sup>For instance, dissolution of calcite by acidic fluids follows this scheme, as it can be represented by the following reaction,



After a slight modification, the model presented in this chapter can be also used to model another class of dissolution processes, in which the rate of dissolution depends on the concentration of the products only. Here, dissolution of gypsum by distilled water,



can be given as an example [36].

A more rigorous approach would have to take into account variation of the surface area with porosity,  $s = s(\varphi)$ . An appropriate choice of the  $s(\varphi)$  dependence is, however, a difficult task. Limestone dissolution experiments suggest that such a function is not monotonic: it increases for small  $\varphi$  (onset of the dissolution) and decreases for large  $\varphi$  (late stages of the dissolution) [44]. On the other hand, by examining linear stability of planar dissolution fronts it can be shown that the choice of a specific  $s(\varphi)$  function changes the dissolution system dynamics only quantitatively, not qualitatively [40].

Equations (3.1–3.7) are supplemented by boundary conditions on the velocity and concentration field. Far downstream (at  $x \rightarrow \infty$ )

$$\mathbf{u}(x \rightarrow \infty) = u_0 \mathbf{e}_x, \quad c(x \rightarrow \infty) = 0, \quad (3.9)$$

which accounts for the fact that far from the dissolution front the flow becomes uniform and the reactant concentration approaches the value given by chemical equilibrium. The conditions far upstream ( $x \rightarrow -\infty$ ) are somewhat more subtle. If the reaction front assumes such a form that sufficiently far upstream everything is dissolved, then it is possible to impose

$$\partial_x u_x(x \rightarrow -\infty) = 0 \quad (3.10)$$

on the flow field and

$$c(x \rightarrow -\infty) = c_{in} \quad (3.11)$$

on the concentration field; the former representing the condition that the flow becomes uniform far upstream, the latter corresponding to the reactant concentration imposed at the inlet.

However, if the undissolved phase extends towards  $x \rightarrow -\infty$  (as it is the case for a solitary dissolution finger surrounded by an undissolved matrix), then the condition analogous to (3.11) should be imposed only within the finger, and not on the entire  $x \rightarrow -\infty$  line. We will come back to this issue later on in Chapter 6.

Formally, equations (3.1–3.8) have to be also supplemented by the initial condition of the form

$$\varphi(x, y, z, t = t_0) = \varphi_{init}(x, y, z). \quad (3.12)$$

Let  $\varphi_0$  and  $\varphi_1$  denote the porosities the primary (undissolved) and the secondary (dissolved) rock. Obviously,  $\varphi_1 > \varphi_0$ . We demand that the initial porosity distribution has well-defined asymptotes: the rock downstream is undissolved,  $\varphi_{init}(x \rightarrow \infty) = \varphi_0$ , and the rock upstream is completely dissolved,  $\varphi_{init}(x \rightarrow -\infty) = \varphi_1$ . An exactly stationary front demands an infinite time to develop, thus we formally select  $t_0 \rightarrow -\infty$  as the starting point of the system evolution.

In course of the evolution, as the porous matrix is infiltrated by an incoming flux of reactive fluid, a reaction front develops. It divides the area which is completely dissolved (of final porosity  $\varphi_1$ ) from the region which is not yet completely dissolved (of  $\varphi < \varphi_1$ ) and propagates through the rock. All the chemical activity is concentrated in the vicinity of the front.

## 3.2 Length scales in a stationary front

Let us consider a one-dimensional case: all the fields depend only on time  $t$  and one spatial coordinate,  $x$ . Incompressibility of the Darcy velocity (3.2) along with the boundary condition (3.9) immediately yield

$$u_x = u_0 = \text{const.} \quad (3.13)$$

During its evolution, the front approaches a stationary state, when the fields depend on a single variable,  $x' = x - Ut$ . The front velocity  $U$  is to be determined. Let  $x' = 0$  denote the rightmost position where porosity is maximal:  $\varphi(x' < 0) = \varphi_1$  and  $\varphi(x' > 0) < \varphi_1$ . There is

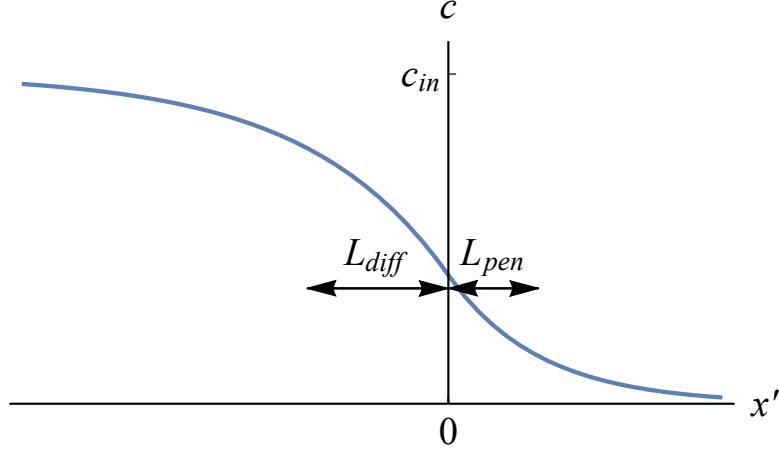


Figure 3.2: Length scales of a stationary dissolution front. Upstream ( $x' < 0$ ) the reactant concentration decays exponentially in the vicinity of the front, with the characteristic length scale  $L_{diff}$ . Downstream ( $x' > 0$ ) it also decreases since the reactant is consumed in the dissolution reaction. The characteristic penetration length is denoted by  $L_{pen}$ .

no soluble material in the upstream ( $x' < 0$ ) domain, and the reaction term  $r$  vanishes there. Eq. (3.6) yields

$$\partial_{x'}(u_0 c - D(\varphi_1) \partial_{x'} c) = 0, \quad x' < 0, \quad (3.14)$$

and can be easily solved as

$$c(x') = c_{in} + C_1 \exp\left(\frac{u_0 x'}{D(\varphi_1)}\right). \quad (3.15)$$

The concentration profiles decays exponentially near the dissolution front ( $x' = 0$ ). The characteristic length of the decay (see Fig. 3.2) is

$$L_{diff} = \frac{D(\varphi_1)}{u_0}. \quad (3.16)$$

Downstream the transport-reaction equation reads

$$\partial_{x'}(u_0 c - D(\varphi) \partial_{x'} c) = -\alpha c, \quad x' > 0. \quad (3.17)$$

Due to presence of the nonlinear dispersion factor, the equation cannot be solved unless it is coupled with the porosity evolution equation (3.7). However, an approximate analysis can be still performed if we assume that the dispersion factor  $D(\varphi)$  is approximately constant. Due to continuity, it has to be of the same order of magnitude as its counterpart upstream,  $D(\varphi) \approx D(\varphi_1) = \text{const}$ . Then Eq. (3.17) can be easily solved to yield

$$c(x') = C_2 \exp(x'/L_{pen}), \quad (3.18)$$

where

$$L_{pen} = \frac{2D(\varphi_1)}{\sqrt{u_0^2 + 4\alpha D(\varphi_1)} - u_0} \quad (3.19)$$

is the downstream penetration length of the reactant. The  $C_{1,2}$  constants can be found from continuity of  $c$  and  $\partial_{x'} c$  across  $x' = 0$ .

The ratio of  $L_{diff}$  and  $L_{pen}$  is equal to

$$\frac{L_{diff}}{L_{pen}} = \frac{\sqrt{1 + 4H} - 1}{2}, \quad (3.20)$$

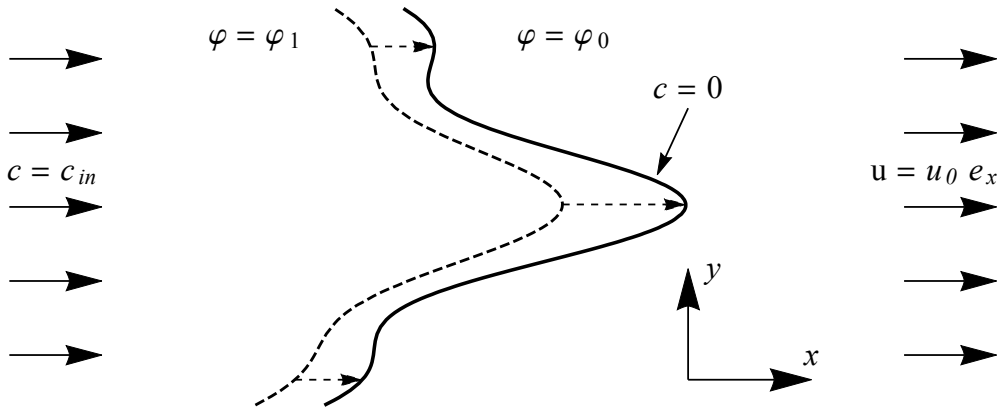


Figure 3.3: Geometry of the system: a reactive fluid is injected from the left side and dissolves the porous matrix through chemical reactions. The reaction front separates the dissolved, upstream domain ( $\Omega$ ) of porosity  $\varphi_1$  and the undissolved, downstream domain ( $\bar{\Omega}$ ) of porosity  $\varphi_0$ , complementary to  $\Omega$ . As time proceeds, the reaction front migrates, which is schematically represented by the transition from the dashed-line domain boundary to the solid-line boundary.

where

$$H = \frac{\alpha D(\varphi_1)}{u_0^2} \quad (3.21)$$

is a dimensionless coefficient [42]. For  $H \gg 1$  the upstream diffusive decay length is much larger than the downstream penetration length,  $L_{diff} \gg L_{pen}$ , and vice versa.

### 3.3 Thin front approximation

In the following analysis we will make one more approximation, mainly that the penetration length  $L_{pen}$  is significantly smaller than any other length scale of our interest. All the chemical activity is then concentrated in the region of negligible thickness just at the reaction front. This “thin front” approximation is justified whenever  $H$  is much larger than unity,  $H \gg 1$ . In this case  $L_{pen} \ll L_{diff}$ .

Once the reaction front is formed, it divides two distinct regions. Upstream of the front, all the soluble material has dissolved and the porosity is constant,  $\varphi = \varphi_1$ . Ahead of the front the matrix has not been dissolved yet and the porosity is still equal to its initial value,  $\varphi = \varphi_0$ . The thickness of the reaction front in our approximation is zero, so in fact the porosity changes discontinuously at the front from  $\varphi_1$  to  $\varphi_0$ . As a consequence, we obtain a Stefan-like problem in which the rock is divided into two domains: the dissolved, upstream domain (denoted by  $\Omega$ ) of porosity  $\varphi_1$  and the undissolved, downstream domain (complementary to  $\Omega$  and denoted by  $\bar{\Omega}$ ) of porosity  $\varphi_0$ . The system is illustrated in Fig. 3.3.

In both domains the porosity (and hence permeability) is constant, so Eqs. (3.1–3.2) can be combined to yield the Laplace equation for the pressure,

$$\nabla^2 p = 0, \quad (3.22)$$

in either  $\Omega$  or  $\bar{\Omega}$ . The thin-front approximation implies infinitely fast equilibration of the reactant concentration,

$$c|_{\partial\Omega} = 0, \quad (3.23)$$

where  $\partial\Omega$  denotes the reaction front. In the downstream domain ( $\bar{\Omega}$ ) the reactant concentration is constant,  $c = 0$ . In the upstream domain ( $\Omega$ ), it satisfies the advection-dispersion equation (3.6),

$$\nabla \cdot (\mathbf{u}c - D(\varphi_1)\nabla c) = 0, \quad (3.24)$$

where  $\mathbf{u} = -K(\varphi_1)\mu^{-1}\nabla p$ . Since the porosity jump at the front is discontinuous, the evolution equation (3.7) has to be replaced by an equation for the reaction front velocity. Combining Eqs. (3.6–3.7), we obtain

$$\nabla \cdot (\mathbf{u}c - D(\varphi)\nabla c) = -\frac{n}{\nu}\frac{\partial\varphi}{\partial t}. \quad (3.25)$$

Let us choose a particular time moment  $t_1$  and consider a small rectangle  $R$  centered at a point  $\mathbf{r}_f$  located at the reaction front. The two sides of this rectangle will be aligned with the vectors normal ( $\mathbf{e}_n$ ) and tangential ( $\mathbf{e}_t$ ) to the front:  $R = \{\mathbf{r} : -\epsilon_n < (\mathbf{r} - \mathbf{r}_f) \cdot \mathbf{e}_n < \epsilon_n, -\epsilon_t < (\mathbf{r} - \mathbf{r}_f) \cdot \mathbf{e}_t < \epsilon_t\}$ . The normal vector  $\mathbf{e}_n$  will point downstream ( $\mathbf{e}_n \cdot \mathbf{e}_\xi > 0$ ). Integrating both sides of (3.25) over  $R$ , and using the Gauss's theorem, we obtain

$$\iint_R d\xi d\eta \nabla \cdot (\mathbf{u}c - D(\varphi)\nabla c) = -\frac{n}{\nu} \iint_R d\xi d\eta \frac{\partial\varphi}{\partial t}, \quad (3.26)$$

$$\mathbf{e}_n \cdot (\mathbf{u}c - D(\varphi)\nabla c)|_{\mathbf{r}_f - \epsilon_n \mathbf{e}_n}^{\mathbf{r}_f + \epsilon_n \mathbf{e}_n} = -\frac{n}{\nu} \frac{d}{dt} \int_{[\mathbf{r}_f - \epsilon_n \mathbf{e}_n, \mathbf{r}_f + \epsilon_n \mathbf{e}_n]} dl \varphi. \quad (3.27)$$

The left-hand side of Eq. (3.27) is the difference of the reactant fluxes at both sides of the front. The right-hand side of Eq. (3.27) is the (rescaled by  $n/\nu$ ) rate at which the local integral of porosity changes, and is directly related to the local front velocity  $\mathbf{U}$ . Taking the limit  $\epsilon_n \rightarrow 0$ , in the thin-front approximation one obtains

$$D(\varphi_1)\mathbf{e}_n \cdot \nabla c|_{\partial\Omega^-} = -\frac{n}{\nu}\mathbf{e}_n \cdot \mathbf{U}(\varphi_1 - \varphi_0). \quad (3.28)$$

The left-hand side of Eq. (3.28) is the diffusive flux of the reactant, incoming to the front. The outgoing diffusive reactant flux and advective fluxes vanish, since  $c = 0$  at the front and downstream from the front. In Eq. (3.28) only normal components are compared with each other. Since the tangential components are both zero, Eq. (3.28) can be written as

$$\mathbf{U} = -\frac{\nu}{n(\varphi_1 - \varphi_0)} D(\varphi_1)\nabla c \Big|_{\partial\Omega^-} = -\frac{\gamma}{c_{in}} D(\varphi_1)\nabla c \Big|_{\partial\Omega^-}, \quad (3.29)$$

where the acid capacity number  $\gamma \equiv \nu c_{in}/(n(\varphi_1 - \varphi_0))$  is defined as the volume of rock (of molar volume  $\nu$ ) that is completely dissolved by a unit volume of reactant (of molar concentration  $c_{in}$ ).

Similarly as before the thin-front approximation was introduced, both the pressure and the normal component of the Darcy velocity need to be continuous across the reaction front  $\partial\Omega$ :

$$p|_{\partial\Omega(t)^-} = p|_{\partial\Omega(t)^+}, \quad (3.30)$$

$$u_n|_{\partial\Omega(t)^-} = u_n|_{\partial\Omega(t)^+} \quad (3.31)$$

Lastly let us note that the thin-front approximation was derived assuming that the reaction is a first-order one, but similar reasoning can be applied for other chemical kinetics as well. After taking the thin-front limit, the equations of the dynamics become independent of the chemical kinetics. In principle, Eq. (3.29) for the front velocity results solely from mass balance between the incoming reactant and the soluble material.

### 3.4 Scaling

Equations (3.22–3.24, 3.29) can be simplified by scaling the velocity, concentration, and porosity fields by their characteristic values,

$$\hat{\mathbf{u}} = \frac{\mathbf{u}}{u_0}, \quad \hat{c} = \frac{c}{c_{in}}, \quad \hat{\varphi} = \frac{\varphi - \varphi_0}{\varphi_1 - \varphi_0}, \quad (3.32)$$

where the scaled, dimensionless variables are marked by hats. Additionally, we want to scale the spatial coordinates by some length  $L$ , characterizing the system, and time by  $T = L/(\gamma u_0)$ ,

$$\hat{\mathbf{r}} = \mathbf{r}/L, \quad \hat{t} = t/T. \quad (3.33)$$

Using  $L$ , we can scale the pressure as follows

$$\hat{p} = \frac{K(\varphi_0)}{u_0 \mu L} p. \quad (3.34)$$

In this thesis two length scales will be considered. In this chapter and in the following one, the diffusive length  $L_{diff}$  (3.16) will be chosen as the length scale,

$$L = L_{diff} = \frac{D(\varphi_1)}{u_0}. \quad (3.35)$$

In fact, it is the only length scale which can be naturally derived from the parameters of the model in the thin front limit. In Chapter 6, where the stationary geometry of the front will be of our interest, another length scale will be chosen. We will come back to this issue later on.

With these scalings, the governing equations take the form

$$\hat{\nabla}^2 \hat{p} = 0 \quad \mathbf{r} \in \Omega(\hat{t}) \quad (3.36)$$

$$\kappa \hat{\nabla} \hat{p} \cdot \hat{\nabla} \hat{c} + \hat{\nabla}^2 \hat{c} = 0 \quad \mathbf{r} \in \Omega(\hat{t}) \quad (3.37)$$

in the upstream region and

$$\hat{\nabla}^2 \hat{p} = 0 \quad \mathbf{r} \in \bar{\Omega}(\hat{t}) \quad (3.38)$$

$$\hat{c} = 0 \quad \mathbf{r} \in \bar{\Omega}(\hat{t}) \quad (3.39)$$

in the downstream one. In the above,

$$\kappa \equiv \frac{K(\varphi_1)}{K(\varphi_0)} \quad (3.40)$$

is the ratio of permeabilities of the domains. In typical geological conditions the permeability is an increasing function of porosity, thus  $\kappa > 1$ . The boundary conditions (3.9–3.11) in the scaled variables take the form

$$\hat{\mathbf{u}}(x \rightarrow \infty) = \mathbf{e}_x, \quad \hat{c}(x \rightarrow \infty) = 0, \quad (3.41)$$

and

$$(\partial_x \hat{u}_x)(x \rightarrow -\infty) = 0, \quad \hat{c}(x \rightarrow -\infty) = 1, \quad (3.42)$$

which, as before, need to be supplemented by the continuity conditions for the pressure  $\hat{p}$  and the normal component of the velocity  $\hat{u}_n$  across the interface<sup>2</sup> at the boundary (reaction front)  $\partial\Omega$ . Finally, the condition (3.29) for the front advancement velocity takes the form

$$\hat{U}_n = -(\hat{\nabla} \hat{c})_n \quad (3.43)$$

Noting that at the reaction front the concentration satisfies a purely kinematic condition

$$\hat{\mathbf{U}} \cdot \hat{\nabla} \hat{c} + \frac{\partial \hat{c}}{\partial \hat{t}} = 0, \quad (3.44)$$

one can rewrite (3.43) in terms of  $\hat{c}$  only:

$$\frac{\partial \hat{c}}{\partial \hat{t}} - |\hat{\nabla} \hat{c}|^2 = 0 \quad \mathbf{r} \in \partial\Omega(\hat{t}) \quad (3.45)$$

---

<sup>2</sup>Note that  $\hat{\mathbf{u}} = -\kappa \hat{\nabla} \hat{p}$  in  $\Omega$  and  $\hat{\mathbf{u}} = -\hat{\nabla} \hat{p}$  in  $\bar{\Omega}$ .

### 3.5 One-dimensional (planar) solutions

It is relatively straightforward to derive the one-dimensional solutions of Eqs. (3.36–3.39), corresponding to the planar reactive front propagating with a constant velocity,  $U_0$ . Assuming that both  $\hat{c}$  and  $\hat{p}$  are functions of  $\hat{x}$  and  $\hat{t}$  only, leads to

$$\hat{p}_0(\xi) = \begin{cases} -\kappa^{-1}\xi & \xi < 0 \\ -\xi & \xi > 0, \end{cases} \quad (3.46)$$

where  $\xi = \hat{x} - \hat{U}_0\hat{t}$  is the coordinate moving with the front, and  $\xi = 0$  denotes the front position. For the concentration we get an exponentially decaying, diffusive profile

$$\hat{c}_0(\xi) = \begin{cases} 1 - e^\xi & \xi < 0 \\ 0 & \xi > 0. \end{cases} \quad (3.47)$$

Finally, inserting the above into the front velocity condition (3.43) we obtain the result  $\hat{U}_0 = 1$ , i.e. in the chosen units the planar reaction front advances with a unit velocity along the flow direction. Note that the dimensional planar front velocity is

$$U_0 = \gamma u_0 = \frac{c_{in} \nu u_0}{n(\varphi_1 - \varphi_0)}, \quad (3.48)$$

which in fact could have been derived simply by considering mass balance between the incoming reactant and the dissolved mineral.

### 3.6 Instability of the planar dissolution front

As already shown in the 1980s [43, 16], the planar dissolution front is unstable with respect to arbitrarily small perturbations. The origin of this instability, dubbed the “reactive-infiltration instability”, can be understood intuitively. Suppose that a small protrusion developed in the initially planar reaction front (solid line in Fig. 3.4). Such a bump is more permeable than its neighbourhood, and focuses the fluid flow. Consequently, the bump is exposed to a higher reactant flux, which further promotes its dissolution, and the reaction front propagates faster there (dashed line in Fig. 3.4). The bump gets amplified. To sum up, the reactive-infiltration instability is a consequence of the existence of the positive feedback loop between the flow, the reactant transport and porosity generation in course of dissolution. In this section, performing linear stability analysis of the one-dimensional stationary solutions (3.46–3.48) of equations (3.36–3.39), we show that the planar dissolution front is unstable. The derivation is equivalent to the one presented in the classical Ref. [43]. For simplicity, we will consider a two-dimensional case. It is most convenient to work in the reference frame moving with the front, i.e. having applied the following transformation from  $(\hat{x}, \hat{y}, \hat{t})$  to  $(\xi, \eta, \tau)$ ,

$$\xi = \hat{x} - \hat{U}_0\hat{t} \quad (3.49)$$

$$\eta = \hat{y} \quad (3.50)$$

$$\tau = \hat{t}. \quad (3.51)$$

The stability analysis proceeds by assuming that the dissolution front (initially located at  $\xi = 0$ ) is perturbed by a small perturbation  $\zeta(\eta, \tau) \ll 1$ , so that the front position is given by

$$\xi = \zeta(\eta, \tau). \quad (3.52)$$

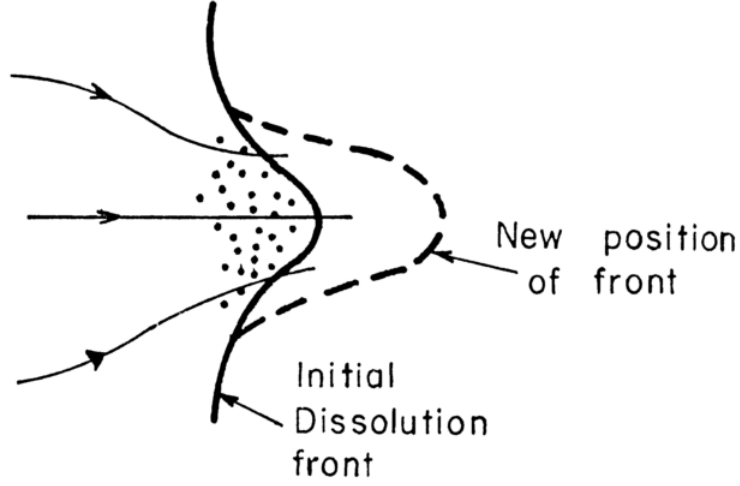


Figure 3.4: An arbitrarily small bump in the dissolution front attracts more flow than its neighbourhood and gets amplified, as its dissolution is increased. Source: [16].

The perturbation of the front causes similar, infinitesimal perturbations of the pressure and the concentration fields,

$$\hat{p}^{\pm}(\xi, \eta, \tau) = \hat{p}_0^{\pm}(\xi) + \tilde{p}^{\pm}(\xi, \eta, \tau) \quad (3.53)$$

$$\hat{c}(\xi, \eta, \tau) = \hat{c}_0(\xi) + \tilde{c}(\xi, \eta, \tau), \quad (3.54)$$

where the  $\pm$  superscript denotes, respectively, the downstream ( $\xi > \zeta$ ) and upstream ( $\xi < \zeta$ ) domains<sup>3</sup>, and the tildes denote the perturbations to the base solutions. The perturbed fields are then inserted to the equations of dynamics (3.36–3.39), yielding

$$\hat{\nabla}^2(\hat{p}_0^{\pm} + \tilde{p}^{\pm}) = 0, \quad (3.55)$$

$$\kappa \hat{\nabla}(\hat{p}_0^{-} + \tilde{p}^{-}) \cdot \hat{\nabla}(\hat{c}_0 + \tilde{c}) + \hat{\nabla}^2(\hat{c}_0 + \tilde{c}) = 0. \quad (3.56)$$

Noting that the unperturbed solutions satisfy the original equations and disregarding terms which are smaller than linear in the perturbations, the problem simplifies to

$$\hat{\nabla}^2 \tilde{p}^{\pm} = 0 \quad (3.57)$$

$$-\partial_{\xi} \tilde{c} - \kappa e^{\xi} \partial_{\xi} \tilde{p}^{-} + \hat{\nabla}^2 \tilde{c} = 0. \quad (3.58)$$

The boundary conditions follow from the ones for the general formulation of the problem,

$$\partial_{\xi}^2 \tilde{p}^{-} \Big|_{\xi \rightarrow -\infty} = 0, \quad \partial_{\xi} \tilde{p}^{+} \Big|_{\xi \rightarrow \infty} = 0, \quad (3.59)$$

$$\tilde{c} \Big|_{\xi \rightarrow -\infty} = 0. \quad (3.60)$$

At the reaction front the pressure, the normal component of the Darcy velocity, and the concentration should be continuous,

$$(\hat{p}_0^{-} + \tilde{p}^{-})_{\xi=\zeta} = (\hat{p}_0^{+} + \tilde{p}^{+})_{\xi=\zeta+} \quad (3.61)$$

$$-\kappa \hat{\nabla}(\hat{p}_0^{-} + \tilde{p}^{-}) \cdot (\hat{\mathbf{n}}_0 + \tilde{\mathbf{n}}) \Big|_{\xi=\zeta} = -\hat{\nabla}(\hat{p}_0^{+} + \tilde{p}^{+}) \cdot (\hat{\mathbf{n}}_0 + \tilde{\mathbf{n}}) \Big|_{\xi=\zeta} \quad (3.62)$$

$$(\hat{c}_0 + \tilde{c})_{\xi=\zeta} = 0, \quad (3.63)$$

<sup>3</sup>The concentration field is nontrivial only in the upstream domain, thus a similar indexing would be redundant here.

which, after linearization in the perturbations, yields

$$(\tilde{p}^- - \kappa^{-1}\zeta)_{\xi=0} = (\tilde{p}^+ - \zeta)_{\xi=0} \quad (3.64)$$

$$(-\kappa\partial_\xi\tilde{p}^-)_{\xi=0} = (-\partial_\xi\tilde{p}^+)_{\xi=0} \quad (3.65)$$

$$(\tilde{c} - \zeta)_{\xi=0} = 0. \quad (3.66)$$

So far we have not assumed any specific form of the perturbations, which we shall do now. It is most convenient to choose a perturbation which is harmonic in the direction perpendicular to the dominant flow direction,

$$\zeta(\eta, \tau) = a(\tau) \sin(\hat{k}\eta). \quad (3.67)$$

Similarly, the pressure and concentration field perturbations are also supposed to be composed of the sinusoidal factor and the  $(\xi, \tau)$ -dependent amplitude,

$$\tilde{p}^\pm(\xi, \eta, \tau) = a_p^\pm(\xi, \tau) \sin(\hat{k}\eta) \quad (3.68)$$

$$\tilde{c}(\xi, \eta, \tau) = a_c(\xi, \tau) \sin(\hat{k}\eta). \quad (3.69)$$

The Laplace equations for the pressure can be immediately solved to yield the general solution

$$a_p^\pm(\xi, \tau) = C_1^\pm(\tau)e^{-\hat{k}\xi} + C_2^\pm(\tau)e^{\hat{k}\xi} \quad (3.70)$$

in either of the domains. The far-field conditions for the pressure (3.59) allow us to find two of the integration constants (which are equal to zero), thus

$$a_p^-(\xi, \tau) = C_2^-(\tau)e^{\hat{k}\xi}, \quad a_p^+(\xi, \tau) = C_1^+(\tau)e^{-\hat{k}\xi}. \quad (3.71)$$

The continuity conditions for the pressure and the normal Darcy velocity are sufficient to find the remaining two of the integration constants,

$$C_2^-(\tau) = a(\tau) \frac{\kappa^{-1} - 1}{\kappa + 1}, \quad C_1^+(\tau) = a(\tau) \frac{\kappa - 1}{\kappa + 1}. \quad (3.72)$$

Now the perturbed transport equation reads

$$-\partial_\xi a_c(\xi, \tau) + a(\tau) \frac{\kappa - 1}{\kappa + 1} \hat{k} e^{(\hat{k}+1)\xi} + (\partial_\xi^2 - \hat{k}^2) a_c(\xi, \tau) = 0 \quad (3.73)$$

and can be solved analytically as

$$a_c(\xi, \tau) = C_3(\tau) e^{\frac{1}{2}(\sqrt{4\hat{k}^2+1}+1)\xi} - a(\tau) \frac{\kappa - 1}{\kappa + 1} e^{(\hat{k}+1)\xi} \quad (3.74)$$

(where we have already made use of the concentration-vanishing far-field condition at  $\xi \rightarrow -\infty$ , Eq. (3.60)). The continuity condition for the concentration (3.66) allows us to determine the last integration constant,

$$C_3(\tau) = a(\tau) \frac{2\kappa}{\kappa + 1}, \quad (3.75)$$

and find  $a_c$ ,

$$a_c(\xi, \tau) = \frac{a(\tau)}{\kappa + 1} \left( 2\kappa e^{\frac{1}{2}(\sqrt{4\hat{k}^2+1}+1)\xi} + (1 - \kappa) e^{(\hat{k}+1)\xi} \right). \quad (3.76)$$

Note that for each Fourier mode, both the pressure and the concentration perturbations can be factorized as products of functions of single variables:  $\xi$ ,  $\eta$ , and  $\tau$ .

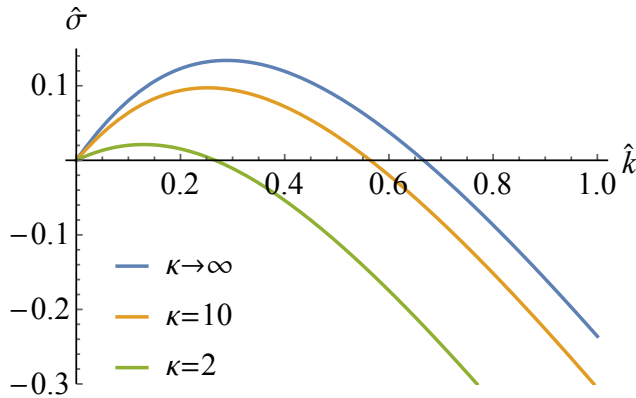


Figure 3.5: Dispersion curves characterizing the stability of a dissolution front in the thin-front limit, as given by Eq. (3.80), for  $\kappa = \infty, 10, 2$  (top to bottom). The front gets more unstable as the permeability contrast  $\kappa$  increases.

As the last step of our analysis, we use the front propagation condition (3.45) to determine the form of the time growth function  $a(\tau)$ . The linearized condition (3.45) reads

$$(\partial_\tau - \partial_\xi)\tilde{c} - 2\tilde{c}'_0\partial_\xi\tilde{c} + (-\tilde{c}'_0 - 1(\tilde{c}'_0)^2)' \zeta \Big|_{\xi=0} = 0 \quad (3.77)$$

which, after some simplifications, gives the first-order equation for the growth function  $a(\tau)$ ,

$$(\kappa + 1)\dot{a}(\tau) = a(\tau) \left( \kappa \left( 1 - \sqrt{4\hat{k}^2 + 1} \right) + (\kappa - 1)\hat{k} \right). \quad (3.78)$$

The solution of Eq. (3.78) is the exponential function

$$a(\tau) = a(0)e^{\hat{\sigma}\tau}, \quad (3.79)$$

where the growth factor  $\hat{\sigma}$  is equal to

$$\hat{\sigma}(\hat{k}; \kappa) = \frac{(\kappa - 1)\hat{k} - \kappa \left( \sqrt{4\hat{k}^2 + 1} - 1 \right)}{\kappa + 1}. \quad (3.80)$$

Expression (3.80) is analogous to Eq. (VIII.3) from [16] and to Eq. (5.1) from [40]. However, the notation of these authors is different from ours. In principle, their definition of the permeability contrast (denoted by  $\Gamma$  in both [16] and [40]) is the inverse of ours.

Eq. (3.80) gives the dispersion relation, i.e. the relation between the rate of growth of a small sinusoidal perturbation of the dissolution front, and its wavenumber. The permeability ratio  $\kappa$  is a parameter here. Let us recall that for dissolution the permeability ratio  $\kappa$  is always larger than unity. The dispersion curves are illustrated in Fig. 3.5. In any case the infinitely long perturbations are marginally stable,

$$\hat{\sigma}(\hat{k} = 0) = 0. \quad (3.81)$$

This is expected, since an infinitely long-wave perturbation is a mere translation of the front. Since the domain which we consider is infinite in the  $x$  direction, such a translation should not affect the system. (In the case of finite-length domains, however, the zero-wavenumber perturbation can be unstable [40]). Therefore stability of long-wave perturbations can be assessed by studying the first derivative of  $\hat{\sigma}(\hat{k})$  at  $\hat{k} = 0$ ,

$$\hat{\sigma}'(\hat{k}) \Big|_{\hat{k}=0} = \frac{\kappa - 1}{\kappa + 1}. \quad (3.82)$$

Long-wave perturbations are unstable whenever  $\kappa > 1$  (i.e. when the secondary phase is more permeable than the primary phase). In the case of equal permeabilities across the front ( $\kappa = 1$ ),  $\hat{\sigma}'(\hat{k} = 0) = 0$  and the second derivative has to be evaluated at  $\hat{k} = 0$  to assess the front stability. As it turns out,

$$\hat{\sigma}''(\hat{k}; \kappa = 1) \Big|_{\hat{k}=0} = -2 < 0, \quad (3.83)$$

so in the marginal case of  $\kappa = 1$ , the front is stable with respect to long-wave perturbations.

For a given  $\kappa$  (except for the limiting case of  $\kappa = 1$ ) a dispersion relation has a single maximum. The most unstable mode corresponds to the wavenumber

$$\hat{k}_* = \frac{\kappa - 1}{\sqrt{\kappa + 1}\sqrt{12\kappa - 4}}. \quad (3.84)$$

The critical wavenumber, above which all the modes are stable (due to diffusion, which stabilizes the front) is equal to

$$\hat{k}_{cr} = \frac{2(\kappa - 1)\kappa}{3\kappa^2 + 2\kappa - 1}. \quad (3.85)$$

Consequently, the most unstable and the critical wavelength are equal to

$$\hat{\lambda}_* = \frac{2\pi\sqrt{\kappa + 1}\sqrt{12\kappa - 4}}{\kappa - 1}, \quad (3.86)$$

$$\hat{\lambda}_{cr} = \frac{\pi(3\kappa^2 + 2\kappa - 1)}{(\kappa - 1)\kappa}. \quad (3.87)$$

The front gets more unstable as the permeability contrast increases. The limit of large permeability contrast ( $\kappa \rightarrow \infty$ ) is finite,

$$\hat{\sigma}(\hat{k}; \kappa \rightarrow \infty) = \hat{k} - \sqrt{4\hat{k}^2 + 1} + 1. \quad (3.88)$$

In this case, the most unstable mode and the critical mode are, respectively,

$$\lim_{\kappa \rightarrow \infty} \hat{k}_* = \frac{1}{2\sqrt{3}}, \quad \lim_{\kappa \rightarrow \infty} \hat{\lambda}_* = 4\sqrt{3}\pi \quad (3.89)$$

$$\lim_{\kappa \rightarrow \infty} \hat{k}_{cr} = \frac{2}{3}, \quad \lim_{\kappa \rightarrow \infty} \hat{\lambda}_{cr} = 3\pi. \quad (3.90)$$

In the dimensional length units, the most unstable and the critical wavelengths are

$$\lambda_* = \frac{2\pi\sqrt{\kappa + 1}\sqrt{12\kappa - 4}}{(\kappa - 1)} \frac{D(\varphi_1)}{u_0}, \quad (3.91)$$

$$\lambda_{cr} = \frac{\pi(3\kappa^2 + 2\kappa - 1)}{(\kappa - 1)\kappa} \frac{D(\varphi_1)}{u_0}. \quad (3.92)$$

Fig. 3.6 shows the domains of stable and unstable perturbation waves, with the length scale chosen as  $L_{diff}$ .

In this section we were assuming that our system is two-dimensional. A linear stability analysis in 3D is fully analogous to the 2D one. One would have to assume that the front perturbation is

$$\xi = \zeta(\eta_1, \eta_2, \tau) = a(\tau) \sin(\hat{k}_1\eta_1 + \hat{k}_2\eta_2), \quad (3.93)$$

where  $(\xi, \eta_1, \eta_2)$  are the three orthogonal spatial coordinates. In fact, such a three-dimensional LSA can be reduced to the two-dimensional one, since the perturbation (3.93) can be posed as

$$\xi = \zeta(\eta, \tau) = a(\tau) \sin(\hat{k}\eta), \quad (3.94)$$

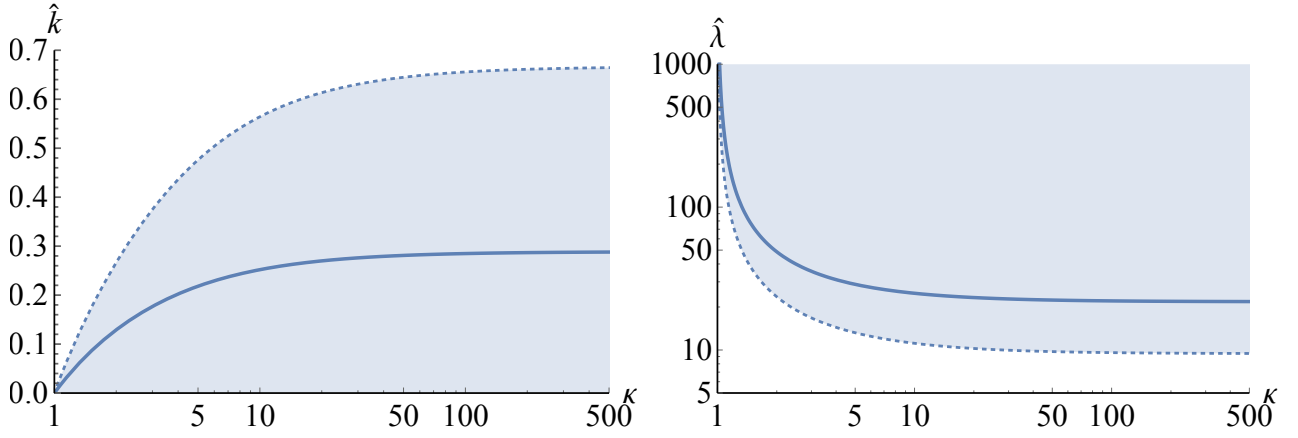


Figure 3.6: Domains of unstable (shaded; long waves) and stable (not shaded; short waves) perturbation modes for varying  $\kappa$ , illustrated in terms of the wavenumber (left) or the wavelength (right). The dotted and the solid lines correspond to, respectively, the critical and the most unstable wavenumber/wavelength. As the permeability contrast  $\kappa$  increases, the unstable domain grows and the most unstable perturbation mode shifts towards shorter waves.

where  $\hat{k} = \sqrt{\hat{k}_1^2 + \hat{k}_2^2}$  and  $\eta = (\hat{k}_1\eta_1 + \hat{k}_2\eta_2)/\hat{k}$ .

Lastly, let us note that in the preceding stability analysis we were assuming that the unperturbed reaction front is infinitely long (in the  $y$  direction). For finite-size domains, waves longer than the system width cannot develop. Since it is the long-wave part of the spectrum which is unstable, the finite width of the system stabilizes the front. In principle, if the width of the system is lower than  $\lambda_{cr}$ , Eq. (3.92), the reaction front is linearly stable.



# Chapter 4

## Onset of the competition between dissolution fingers

The linear stability analysis presented in Chapter 3 allows one to predict the growth rate of an arbitrary harmonic mode of a small perturbation of the dissolution front. Since the amplitudes of the unstable modes grow exponentially, the fastest-growing mode would quickly outgrow the other ones. Thus soon after a spontaneous front breakup, the perturbed front should be almost sinusoidal, with the characteristic wavelength equal to the one characterizing the linearly fastest growing mode. The linear theory, however, does not provide any information about nonlinear effects associated with interactions between protrusions of finite amplitude. Due to complexity of the problem, strict analytical results in the nonlinear regime are very limited. The only relevant study which we are aware of, was a weakly nonlinear analysis by Chadam et al. [45]. The authors analyzed nonlinear effects in the vicinity of the critical mode,  $k_{cr}$ . They showed that modes of slightly longer wavelengths than the critical mode,  $k \lesssim k_{cr}$ , are stabilized by nonlinear effects.

In the current chapter we also develop a weakly nonlinear theory for the reactive-infiltration model, but we concentrate on different phenomena. We conjecture that one of the first effects of nonlinearities in the dynamics would be competition between the protrusions — slightly larger protrusions would attract more reactant flux than the shorter ones, and amplify faster. (Note that a similar mechanism is responsible for the reactive-infiltration instability itself). Our weakly nonlinear analysis thus aims to capture the onset of competition between spontaneously forming protrusions.

Similarly as in Chapter 3 we will consider the thin-front limit ( $H \gg 1$ ), in which the problem is analytically solvable. The model of the system is again given by Eqs. (3.36–3.39) and (3.45) with the appropriate matching conditions across the interface. As in Chapter 3, we will consider small perturbations to the planar stationary solutions (3.46–3.47). Now, however, the reaction front is perturbed by two harmonic modes, so that its position is given by

$$\xi = \zeta(\eta, \tau) = a_1(\tau) \cos(\hat{k}_1 \eta) + a_2(\tau) \cos(\hat{k}_2 \eta + \delta). \quad (4.1)$$

Here,  $a_1, a_2 = O(\epsilon)$ , with  $\epsilon$  being a small parameter. The limitation to just two harmonic modes might seem controversial, but in fact it is based on reasonable assumptions. Firstly, we wish to consider the mode which in the linear theory is the fastest growing one. Let us then set (after (3.84))

$$\hat{k}_1 = \hat{k}_* = \frac{\kappa - 1}{2\sqrt{(\kappa + 1)(3\kappa - 1)}}. \quad (4.2)$$

Additionally, since the couplings are strongest between neighbouring protrusions, it should be expected that the first effect of their competition would be suppression of every second protrusion by its neighbours, which is shown schematically in Fig. 4.1. Such an effect is connected

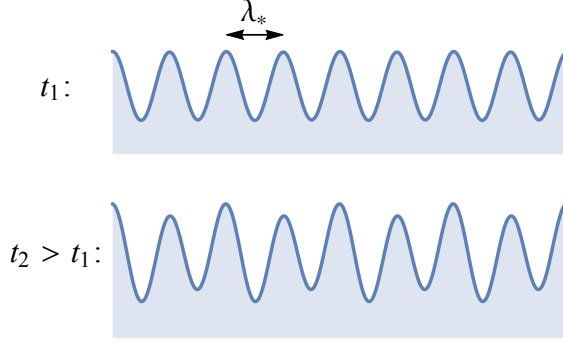


Figure 4.1: Schematic illustration of the first effects of the nonlinearities in the dissolution front dynamics. The dissolution front has spontaneously developed as (almost) sinusoidal, with the characteristic wavelength of the fastest-growing mode (top panel). However, soon the competition between the protrusions starts to play a significant role in the front evolution. Since the competition is stronger at smaller distances, every second protrusion outgrows its neighbours (bottom panel). The amplitudes are not drawn up to the scale in this schematic picture. In reality, they are much smaller than the wavelengths at this stage of the evolution. Also, the vertical scales are different in the panels: the amplitudes at time  $t_2$  are larger than those at time  $t_1$ , since the protrusions are constantly growing.

with the amplification of the first subharmonic mode of  $\hat{k}_*$ . Therefore we set

$$\hat{k}_2 = \hat{k}_*/2. \quad (4.3)$$

We conjecture that the interplay between these two harmonic modes is the dominant nonlinear effect at the onset of the reactive-infiltration instability development.

The idea of our study is due to Huang et al. [46], who were studying the onset of the competition between protrusions developing during Laplacian growth. In their analysis, they also considered weak coupling between just two harmonic modes, whose wavelengths differ by a factor of two. A more extensive weakly nonlinear study of Laplacian growth was conducted by Miranda & Widom [47], who proved that indeed a two-mode approximation is a relevant one.

Due to the front perturbation, the pressure and the concentration fields are also perturbed,

$$\tilde{p}(\xi, \eta, \tau) = f_p(\xi)\alpha_p(\tau) \cos(\hat{k}_*\eta) + g_p(\xi)\beta_p(\tau) \cos\left(\frac{1}{2}\hat{k}_*\eta + \delta\right), \quad (4.4)$$

$$\tilde{c}(\xi, \eta, \tau) = f_c(\xi)\alpha_c(\tau) \cos(\hat{k}_*\eta) + g_c(\xi)\beta_c(\tau) \cos\left(\frac{1}{2}\hat{k}_*\eta + \delta\right). \quad (4.5)$$

The pressure field satisfies the Laplace equation, and its perturbations should vanish far from the front, at  $\xi \rightarrow \pm\infty$ . We immediately find the spatial part of the pressure perturbation amplitudes,

$$f_p(\xi) = C_1 e^{\hat{k}_*\xi}, \quad g_p(\xi) = C_2 e^{\hat{k}_*\xi/2}, \quad \xi < 0 \quad (4.6)$$

$$f_p(\xi) = C_3 e^{-\hat{k}_*\xi}, \quad g_p(\xi) = C_4 e^{-\hat{k}_*\xi/2}, \quad \xi > 0. \quad (4.7)$$

Since we aim to describe quantitatively the onset of the competition between the fingers, the continuity conditions at the dissolution front need to be evaluated up to the second order in  $\epsilon$ . The nonlinear couplings cause the development of higher harmonics, but in the following analysis we shall disregard them, projecting the boundary conditions and the solutions of ODEs onto the two initial modes. The pressure and normal velocity equality across the reaction

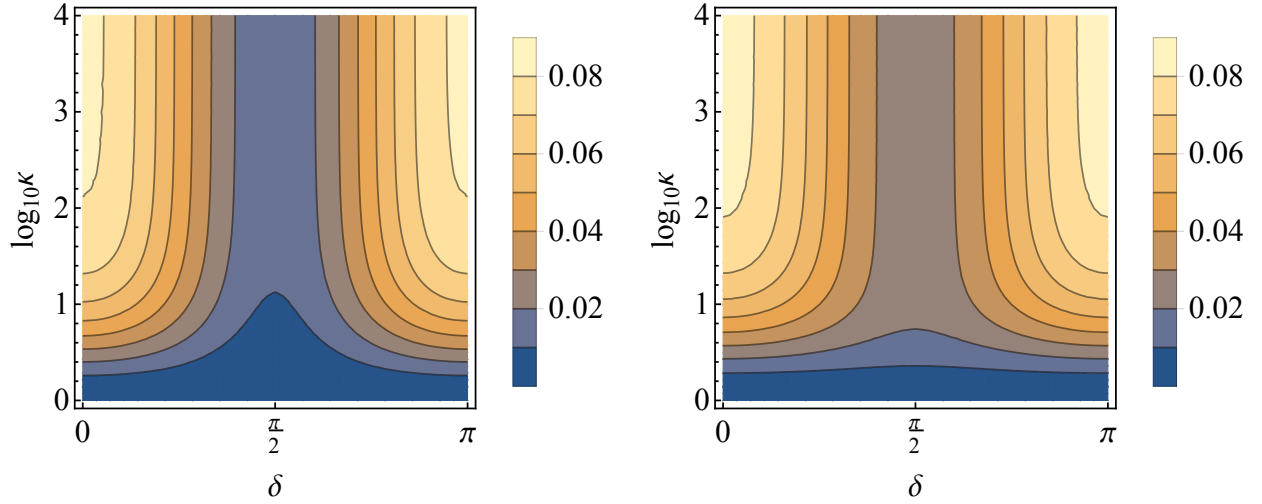


Figure 4.2: Coupling coefficients  $\mu_{1,2}^*$  as functions of  $\kappa$  and  $\delta$ . Both are positive, which leads to the nonlinear effect of suppressing the shorter mode and enhancing the longer one.

front allows one to find the  $C_{1,\dots,4}$  coefficients (up to  $O(\epsilon^2)$ ). Then the transport equation, accompanied by the condition of the concentration vanishing at the reaction front, yields  $f_c(\xi)$  and  $g_c(\xi)$ , which are rather lengthy linear combinations of exponential functions. Finally, the front evolution equation allows one to derive the system of two first-order ODEs, which describes the evolution of the two modes. The ODEs are of the form

$$\dot{a}_1 = \sigma_1^* a_1 - \mu_1^* a_2^2, \quad (4.8a)$$

$$\dot{a}_2 = \sigma_2^* a_2 + \mu_2^* a_1 a_2, \quad (4.8b)$$

which is equivalent to the analogous result obtained for a simpler system of Laplacian growth [46]. Not surprisingly, the  $\sigma_{1,2}^*$  coefficients are given by the standard (linear) dispersion relation (3.80),

$$\sigma_1^* = \hat{\sigma}(\hat{k} = \hat{k}_*) = \frac{2\kappa - \sqrt{(\kappa+1)(3\kappa-1)}}{2(\kappa+1)}, \quad (4.9)$$

$$\sigma_2^* = \hat{\sigma}(\hat{k} = \hat{k}_*/2) = \frac{\kappa \left( \kappa + 4\sqrt{(\kappa+1)(3\kappa-1)} - 2\sqrt{\kappa(13\kappa+6)} - 3 - 2 \right) + 1}{4(\kappa+1)^{3/2}\sqrt{3\kappa-1}}. \quad (4.10)$$

The coupling coefficients,  $\mu_{1,2}^* = \mu_{1,2}^*(\kappa, \delta)$ , have quite complicated functional forms and we shall not quote the exact formulas. Figs. 4.2 and 4.3 illustrate their dependence on  $\kappa$  and  $\delta$ .

In the limit of large permeability contrast between the dissolved and undissolved domains,  $\kappa \rightarrow \infty$ ,

$$\lim_{\kappa \rightarrow \infty} \sigma_1^* = \left( 1 - \frac{\sqrt{3}}{2} \right) \approx 0.134 \quad (4.11)$$

$$\lim_{\kappa \rightarrow \infty} \sigma_2^* = \frac{1}{12} \left( 12 + \sqrt{3} - 2\sqrt{39} \right) \approx 0.104 \quad (4.12)$$

$$\begin{aligned} \lim_{\kappa \rightarrow \infty} \mu_1^* &= \frac{2(5\sqrt{3}-7)(1+\sqrt{13})\cos(2\delta) - 90\sqrt{3} - \sqrt{13} + 6\sqrt{39} + 143}{96(1+\sqrt{13})} \\ &\approx (0.047 + 0.035 \cos(2\delta)) \end{aligned} \quad (4.13)$$

$$\begin{aligned} \lim_{\kappa \rightarrow \infty} \mu_2^* &= \frac{(-845 + 117\sqrt{3} - 29\sqrt{13} + 147\sqrt{39})\cos(2\delta) - 754\sqrt{3} + 387\sqrt{13} + 104\sqrt{39} - 429}{48(2+3\sqrt{3})(13+\sqrt{13})} \\ &\approx (0.054 + 0.030 \cos(2\delta)). \end{aligned} \quad (4.14)$$

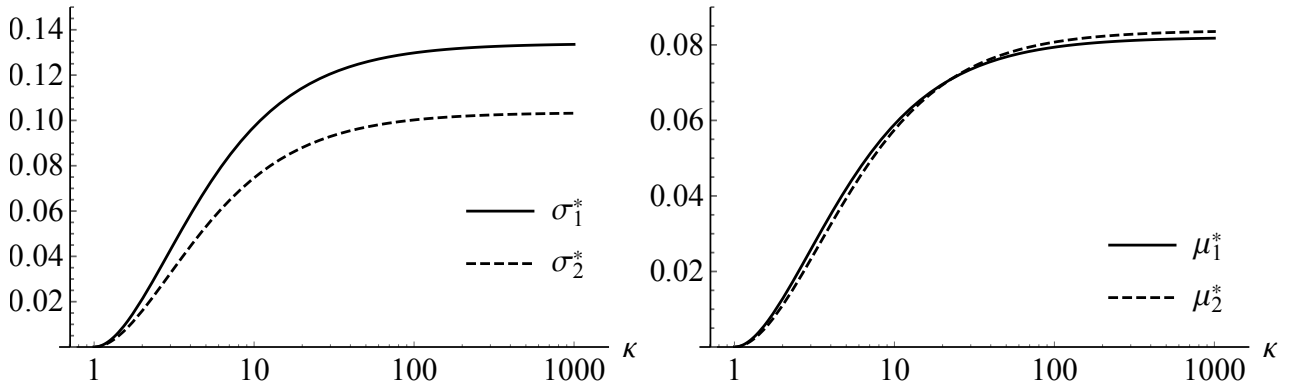


Figure 4.3: Coefficients appearing in the two-mode evolution dynamics, Eq. (4.8), for  $\delta = 0$ , and  $\kappa$  varying from 1 to  $10^3$ . (Left) One-mode growth rates  $\sigma_{1,2}^*$ . Both are positive (i.e. both modes are unstable), but the shorter mode (no. 1) grows (linearly) faster. (Right) Coupling coefficients  $\mu_{1,2}^*$ .

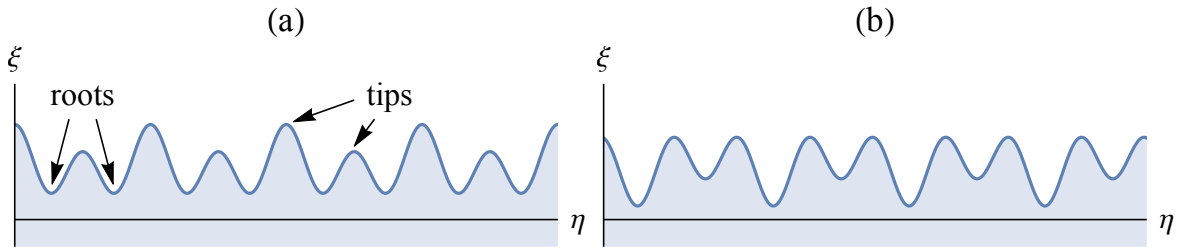


Figure 4.4: The shape of the reaction front (solid line) is a linear combination of two modes:  $\xi_f = \xi_0 \cos(\hat{k}\eta) + 0.5 \xi_0 \cos(\hat{k}\eta/2 + \delta)$  (the subharmonic model has a twice smaller amplitude than the base mode). The  $\delta$  parameter is equal to: (a)  $\delta = n\pi$ ,  $n \in \mathbb{Z}$ ; (b)  $\delta = n\pi + \pi/2$ ,  $n \in \mathbb{Z}$ . The shaded region represents the dissolved domain, and the white region above is undissolved.

Note that the competition is strongest for  $2\delta = 2n\pi$  and weakest for  $2\delta = 2n\pi + \pi$ . It has a straightforward interpretation. In each case adding the subharmonic mode to the base mode has a slightly different effect on the shape of the reaction front. In the first case the  $\xi$  coordinates of the tips of the protrusions take two different values, and every second one reaches further downstream than its neighbours. At the same time, their bases (the roots) are at the same level along the  $\xi$  axis (Fig. 4.4a). The second case is opposite, with the tips at the same level and the roots on two distinct levels (Fig. 4.4b). In case of uncorrelated noise, no value of  $\delta$  is preselected. A whole continuum of subharmonic modes characterized by different values of  $\delta$  can then develop. However, as our analysis shows, there is one particular solution, which grows fastest. Nonlinear couplings are strongest for  $\delta = 0$ , and this particular subharmonic mode is going to dominate. It has a straightforward impact on the shape of the front. As can be deduced from Fig. 4.4, selection of  $\delta = 0$  means that the  $x$  coordinates of the tips of the bumps are much more dispersed than the  $x$  coordinates of their bases. Interestingly, analogous results were obtained during the weakly nonlinear analysis of Laplacian growth [47].

Numerical solutions of the system of ODEs (4.8) are shown in Fig. 4.5. As one can note, both modes initially grow exponentially — the nonlinear effects are weak. The  $\hat{k}_*$  mode, i.e. the linearly most unstable one, grows faster. However, when the modes have sufficiently large amplitudes, the nonlinear effects arise, which suppress this mode and enhance the (twice) longer one. Physically, every second bump in the front is screened by its neighbours. Alas, the theory was developed as only slightly nonlinear and should not be expected to give quantitatively proper results for  $a_{1,2} \sim 1$  (i.e. when the dimensional amplitudes are  $\sim L_{diff}$ ). However, qualitatively the picture should be correct.

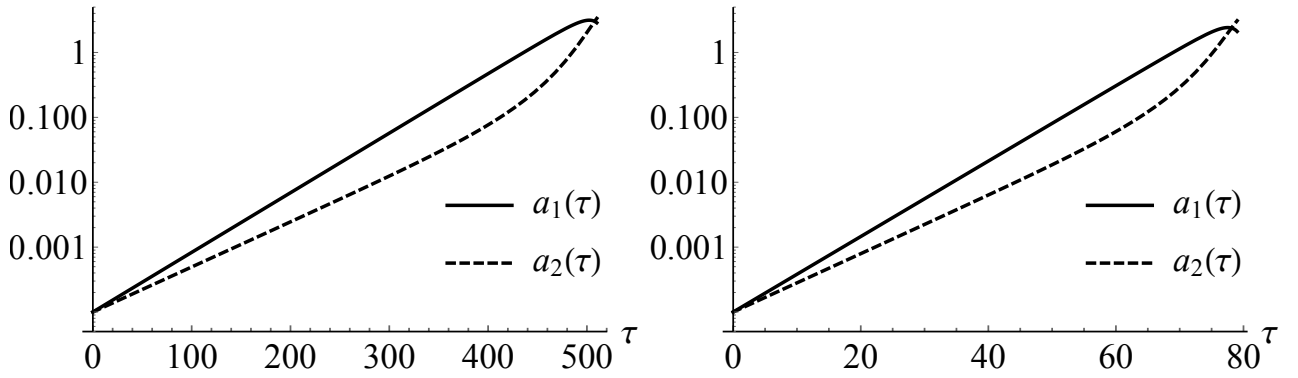


Figure 4.5: Growth of the linearly fastest growing mode,  $\hat{k}_*$ , and its first subharmonic, for  $\delta = 0$ , and  $\kappa = 2$  (left) or  $\kappa \rightarrow \infty$  (right). The results for larger times should be rather treated as qualitative, since the theory is valid only for small perturbations ( $|a_1|, |a_2| \ll 1$ ).

As an additional result of the presented analysis, we are able to estimate the moment when the nonlinear effects become important. It happens when the amplitudes of the modes become comparable with the upstream diffusive length,  $a_i \approx 1$ . If the initial amplitudes of the modes are all equal to  $a_i(\tau = 0) = \epsilon$ , then the characteristic length of the linear growth period is given by

$$\tau_{cr} = -\frac{\ln \epsilon}{\sigma_1^*}. \quad (4.15)$$

The critical time  $\tau_{cr}$  is the time required for the linearly dominant mode to increase its amplitude from  $a_1 = \epsilon$  to  $a_1 = 1$ , assuming that there are no couplings between the modes.



# Chapter 5

## Nonlinear evolution of the dissolution system

In Chapter 3 we have shown that a (planar) dissolution front is unstable with respect to arbitrarily small perturbations. As a consequence, in the presence of noise it is going to break up into a wavy, quasi-sinusoidal front, with a well-defined characteristic distance between the individual protrusions. Next, in Chapter 4 we have shown that these protrusions start to screen each other while competing for the flow and the solvent flux. The further, fully-nonlinear regime of the system dynamics is difficult to study analytically. Some insight into the full dynamics of the system is provided by numerical simulations of the reactive-infiltration dynamics [32, 48, 49]. In the current chapter we present some of the main results of these numerical studies. The conclusions are illustrated by a numerical simulation of the system given by Eqs. (3.1–3.12) (Fig. 5.1).

The initial state of the porous medium is (Fig. 5.1a)

$$\varphi(x, y, t = 0) = \varphi_1 \Theta(-x + x_0) + (\varphi_0 + \eta(x, y)) \Theta(x - x_0), \quad (5.1)$$

where  $\varphi_0$  ( $\varphi_1$ ) is the porosity of the undissolved (dissolved) matrix, and  $\eta$  is a noise. We assume that  $\eta$  is an uncorrelated Gaussian noise of zero mean and standard deviation equal to  $\sqrt{\langle \eta^2 \rangle} = 10^{-2} \varphi_0$ . As regards the values of porosity, we assumed  $\varphi_0 = 0.02$  and  $\varphi_1 = 0.2$ . The value of the transport parameter is  $H = 10$  here, which makes the thin-front approximation justified when describing the system evolution. The cubic permeability model was assumed,  $K \propto \varphi^3$ , and the resulting permeability ratio between the primary and secondary phases is  $\kappa = (\varphi_1/\varphi_0)^3 = 10^3$ .

The initial state of the system has a translational invariance in the  $y$  direction, and it remains almost one-dimensional for some time. In fact, the dissolution front seems to evolve towards its stationary shape, propagating with a constant velocity in the  $x$  direction (Fig 5.1b). However, as the reasoning presented in Chapter 3 suggests, such a state is not stable. Indeed, small disturbances in the initial porosity distribution cause the reaction front to break up and array of bumps (fingers) develops (Fig 5.1c). The larger the fingers, the weaker is the impact of noise on the evolution of the system. Until the fingers are small, the nonlinear couplings between them are negligible. They grow independently, according to the linear theory (Sec. 3.6). However, as soon as the lengths of fingers become comparable with the diffusive length, the couplings cannot be neglected. During this period of the evolution, the weakly nonlinear theory from Chapter 4 should be an appropriate approximation of the dynamics. Indeed, in Fig 5.1d we can see that the  $x$  coordinates of the finger tips are much more dispersed than the  $x$  coordinates of their roots, which is an effect predicted by the theory. In the subsequent stages of the evolution the nonlinear effects are even stronger. The competition between the dissolution fingers typically leads to a cascade of merging and screening events: smaller fingers are either absorbed by larger

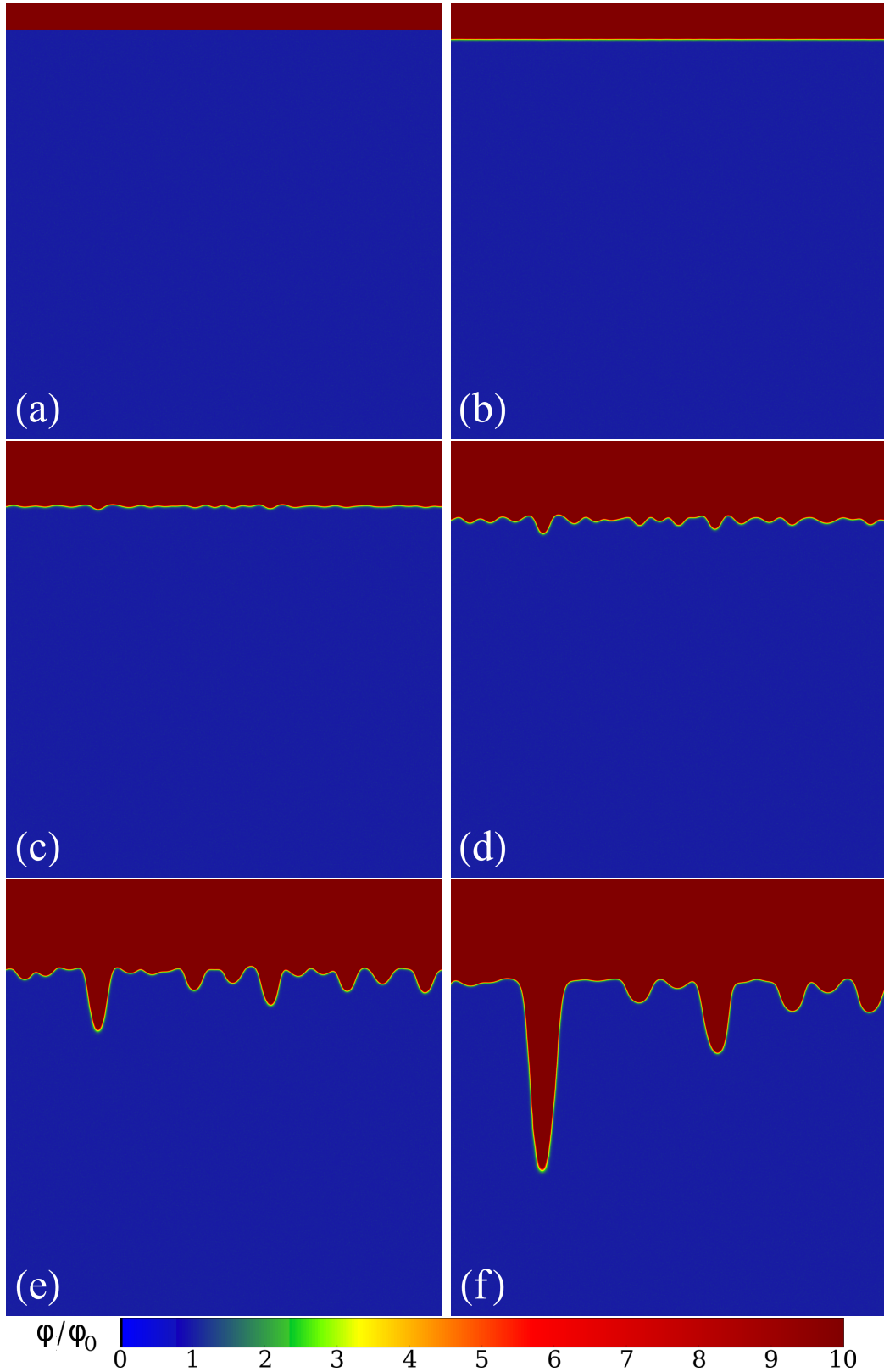


Figure 5.1: Numerical simulation of the dissolution system, Eqs. (3.1–3.12). The partial differential equations are discretized on a rectangular grid,  $2048 \times 2048$  points, which translates to  $204.8L_{diff} \times 204.8L_{diff}$ . The (rescaled) porosity distribution,  $\varphi/\varphi_0$ , is plotted at different moments: (a)  $\hat{t} = 0$ , (b)  $\hat{t} = 0.8$ , (c)  $\hat{t} = 3.2$ , (d)  $\hat{t} = 4.4$ , (e)  $\hat{t} = 6$ , and (f)  $\hat{t} = 8$  (the time scale is equal to  $T = L_{diff}/(u_0\gamma)$ ).

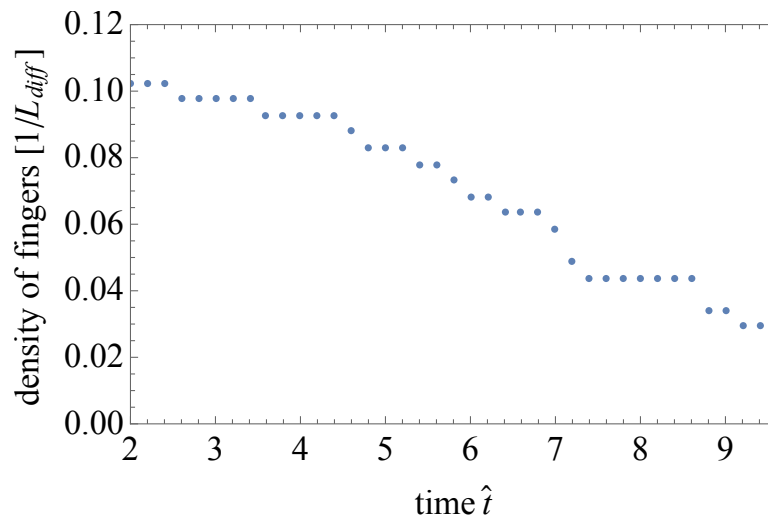


Figure 5.2: Number of dissolution fingers per a unit width of the system, as a function of time. The data was acquired from the numerical simulation presented in Fig. 5.1.

ones, or their growth ceases, because the larger ones absorb all the reactant flux. The number of active fingers decreases in time (Fig. 5.2), but they are getting wider and longer (Fig 5.1e–f).



# Chapter 6

## Stationary dissolution forms

In this chapter we study single, invariantly translating dissolution forms. First, in Sec. 6.1 we aim to find the geometry of a single dissolution finger. Such a form can be regarded as a model of the tip of a long finger (see Fig. 6.1). So far, this problem has not been given much attention by other authors. Propagation of individual dissolution fingers was studied by petroleum engineers [50, 51, 52]. In these works, simple geometric models of wormhole shapes were adopted, which are not preserved during the growth. The closest in spirit to the present study is the work by Nilson and Griffiths from 1990 [53]. They also tackle the problem of steadily propagating dissolution forms and find them to be parabolic (in 2D) or paraboloidal (in 3D). Their reactive-infiltration model seems to be based, however, on rather strong assumptions which are hardly satisfied in natural systems, and the resemblance of their results to ours is only superficial. We discuss it in more detail near the end of Sec. 6.1.1. Here we just mention that in [53] the reactant concentration field is not resolved, but is assumed to be uniform within the finger. Consequently, the dissolution front velocity is taken to be proportional to the local fluid velocity. Additionally, the fluid pressure inside the finger is also assumed to be uniform, which is only justified if the permeability of the dissolved phase is significantly higher than the permeability of the primary rock. As a result of these simplifications, the problem is effectively reduced to a single-phase one, requiring the solution of the Laplace equation for pressure outside the finger only. As discussed in Refs. [54, 55] such “one-phase” growth problems are in general much easier to solve than the “two-phase” problems in which the pressure (and flow field) both inside and outside the finger need to be found, which is the case in the present study. Additionally, we have to solve not only for the pressure, but also for the concentration field, as in our model the reaction front propagation velocity is proportional to the diffusive flux of the reactant.

In Sec. 6.2 we are looking for the counterparts of the dissolution fingers, i.e. for the invariantly translating roots (see Fig. 6.1). Similar problems were studied before, both experimentally [56] and theoretically [57], but contrary to our study, the primary rock was assumed to be impermeable. Our results are thus more general than the previous ones.

In principle, the dynamics of the system was given in Sec. 3.3 (Eqs. 3.36–3.45). However, now we do not want to choose a priori any particular length scale  $L$ , assuming that a more relevant one might appear during our analysis. Such a length scale would be connected with the geometry of the stationary forms which we are going to look for. With the yet unspecified length scale  $L$ , the dynamics of our reactive infiltration system is the following. We have

$$\hat{\nabla}^2 \hat{p} = 0 \quad \mathbf{r} \in \Omega(\hat{t}) \quad (6.1)$$

$$\kappa \hat{\nabla} \hat{p} \cdot \hat{\nabla} \hat{c} + \text{Pe}^{-1} \hat{\nabla}^2 \hat{c} = 0 \quad \mathbf{r} \in \Omega(\hat{t}) \quad (6.2)$$

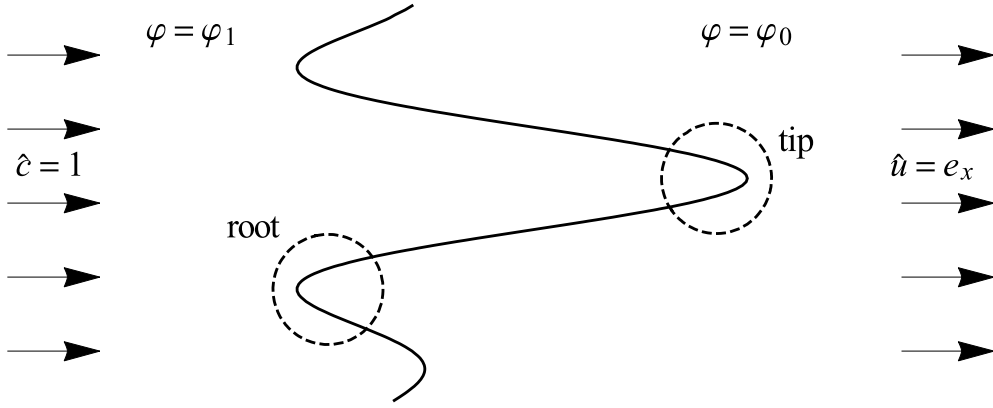


Figure 6.1: The dissolution front (solid line) is a boundary between the dissolved domain upstream and the undissolved domain upstream. A “tip” and a “root” are marked by dashed circles.

in the upstream region and

$$\hat{\nabla}^2 \hat{p} = 0 \quad \mathbf{r} \in \bar{\Omega}(\hat{t}) \quad (6.3)$$

$$\hat{c} = 0 \quad \mathbf{r} \in \bar{\Omega}(\hat{t}) \quad (6.4)$$

in the downstream one. In the above,

$$\text{Pe} \equiv \frac{u_0 L}{D(\varphi_1)} \quad (6.5)$$

is the Péclet number which measures the relative magnitude of convective and diffusive effects in the upstream domain on the length scale  $L$ . The boundary conditions are

$$\hat{\mathbf{u}}(x \rightarrow \infty) = \mathbf{e}_x, \quad \hat{c}(x \rightarrow \infty) = 0, \quad (6.6)$$

and

$$(\partial_x \hat{u}_x)(x \rightarrow -\infty) = 0, \quad \hat{c}(x \rightarrow -\infty) = 1, \quad (6.7)$$

which, as before, need to be supplemented by the continuity conditions for the pressure  $\hat{p}$  and the normal component of the velocity  $\hat{u}_n$  across the interface at the boundary (which is the reaction front)  $\partial\Omega$ . At this boundary, the concentration field also satisfies

$$\frac{\partial \hat{c}}{\partial \hat{t}} - \text{Pe}^{-1} |\hat{\nabla} \hat{c}|^2 = 0 \quad \mathbf{r} \in \partial\Omega(\hat{t}). \quad (6.8)$$

## 6.1 Stationary dissolution fingers

In this section, we derive the shape of a single, invariantly propagating dissolution finger. The exposition follows Ref. [58]. We begin with the two-dimensional case.

### 6.1.1 Two-dimensional stationary dissolution fingers

#### Ivantsov’s ansatz and finger geometry

At the boundary between the phases, Eq. (6.8) is satisfied. Without any loss in generality, one might extend this equation to the whole domain  $\Omega$  as

$$F(\hat{\mathbf{r}}, \hat{t}) \frac{\partial \hat{c}}{\partial \hat{t}} - |\hat{\nabla} \hat{c}|^2 = 0, \quad (6.9)$$

with  $F$  formally given as  $F = |\hat{\nabla}\hat{c}|^2/\partial_{\hat{t}}\hat{c}$  and satisfying  $F|_{\hat{\mathbf{r}}\in\partial\Omega(t)} = \text{Pe}$ . To proceed, we use the ansatz due to Ivantsov [59, 60] by assuming that the functional dependence of  $F$  on spatial and time coordinates is of the form

$$F(\hat{\mathbf{r}}, \hat{t}) = F(c(\hat{\mathbf{r}}, \hat{t})), \quad (6.10)$$

so that

$$F(\hat{c})\frac{\partial\hat{c}}{\partial\hat{t}} - |\hat{\nabla}\hat{c}|^2 = 0 \quad (6.11)$$

is satisfied in the whole domain  $\Omega$ . Obviously,  $F$  must satisfy

$$F(\hat{c} = 0) = \text{Pe} \quad (6.12)$$

for the consistency with the boundary condition (3.45). Using this idea, Ivantsov has found his famous set of steady-state solutions to the dendrite growth problem in a supercooled melt. Note that assuming the ansatz (6.10) might lead to losing some of more general solutions of the problem.

Let us now suppose that our problem has a stationary solution: a dissolution finger moving invariantly in the  $x$  direction with velocity  $U$ . Rewriting Eq. (6.11) in the moving coordinate system gives

$$-\hat{U}F(\hat{c})\frac{\partial\hat{c}}{\partial\hat{x}} - |\hat{\nabla}\hat{c}|^2 = 0 \quad (6.13)$$

or

$$\hat{\nabla}\hat{c} \cdot (\hat{\nabla}\hat{c} + \hat{U}F(\hat{c})\hat{\nabla}\hat{x}) = 0. \quad (6.14)$$

Let us note that both the Laplace equation (6.1) and the advection-diffusion equation with potential flow (6.2) are conformally invariant. A large class of conformally invariant, non-Laplacian physical problems has been identified by Bazant [61, 62] and involves such phenomena as nonlinear diffusion, advection, or electromigration coupled to diffusion. The conformal invariance of these processes provides an effective way of solving these problems [63]. In the context of growth processes, these techniques have been used to track the evolution of the interface in solidification and melting under the action of a potential flow [64, 65, 66, 57, 67, 61, 68]. However, in these works the growth has been taking place in external flows (with the fluid outside of the growing object), in contrast to the present case where the medium is porous, and the driving flow goes through the growing finger and then into the undissolved medium.

In our case, Eq. (6.14) is also conformally invariant. This allows us to make a conformal coordinate transformation  $(\hat{x}, \hat{y}) \rightarrow (\chi, \psi)$  such that  $\hat{c} = \hat{c}(\chi)$  (i.e. the isolines of  $\hat{c}$  coincide with the curves  $\chi(\hat{x}, \hat{y}) = \text{const}$ ). Since Eq. (6.14) is conformally invariant, we get

$$\frac{d\hat{c}}{d\chi} + \hat{U}F(\hat{c}(\chi))\frac{\partial\hat{x}}{\partial\chi} = 0. \quad (6.15)$$

The immediate conclusion is that  $\partial\hat{x}/\partial\chi$  must be a function of  $\chi$  only<sup>1</sup>, hence

$$\hat{x}(\chi, \psi) = \Phi_1(\chi) + \Phi_2(\psi). \quad (6.17)$$

The Cauchy-Riemann conditions,

$$\frac{\partial\hat{y}}{\partial\psi} = \frac{\partial\hat{x}}{\partial\chi}, \quad \frac{\partial\hat{y}}{\partial\chi} = -\frac{\partial\hat{x}}{\partial\psi}, \quad (6.18)$$

---

<sup>1</sup>Note that if one sought a stationary solution without having assumed the Ivantsov ansatz, one would obtain at this point

$$\frac{d\hat{c}}{d\chi} + \hat{U}F(\chi, \psi)\frac{\partial\hat{x}}{\partial\chi} = 0 \quad (6.16)$$

which does not provide any information about the mapping.

lead to the Laplace equation for  $\hat{x}$ ,  $\nabla_{\chi\psi}^2 \hat{x} = 0$ , the general solution of which, compatible with (6.17), is

$$\hat{x}(\chi, \psi) = \frac{1}{2} \hat{\rho} ((\chi - \chi_*)^2 - (\psi - \psi_*)^2). \quad (6.19a)$$

Using again (6.18) allows us to find  $\hat{y}(\chi, \psi)$  in the form

$$\hat{y}(\chi, \psi) = \hat{\rho}(\chi - \chi_*)(\psi - \psi_*) + \hat{y}_*. \quad (6.19b)$$

Without any loss of generality we can set  $\chi_* = \psi_* = y_* = 0$ . Furthermore, we can assume that the parabola characterized by  $\chi = 1$  corresponds to the dissolution front (any other parabola can be scaled onto it by an appropriate choice of parameter  $\hat{\rho}$ ). Note that the parameter  $\hat{\rho}$  corresponds to the (dimensionless) radius of curvature of the parabolic finger. This suggests that the (dimensional) radius of curvature,  $\rho$ , could be used as a length parameter in our problem. Taking  $L = \rho$  leads to  $\hat{\rho} = 1$  which simplifies the further analysis.

Our final conclusion is the following: the only conformal mapping  $(\hat{x}, \hat{y}) \rightarrow (\chi, \psi)$  which makes the concentration field in the dissolution finger a function of one variable only,  $\hat{c}(\hat{x}, \hat{y}) = \hat{c}(\chi(\hat{x}, \hat{y}))$ , is (up to translation)

$$\hat{x}(\chi, \psi) = \frac{1}{2} (\chi^2 - \psi^2) \quad (6.20)$$

$$\hat{y}(\chi, \psi) = \chi\psi, \quad (6.21)$$

which is the usual transformation to the parabolic coordinates. The inverse transformation is

$$\chi^2 = \sqrt{\hat{x}^2 + \hat{y}^2} + \hat{x} = \hat{r} + \hat{x}, \quad (6.22)$$

$$\psi^2 = \sqrt{\hat{x}^2 + \hat{y}^2} - \hat{x} = \hat{r} - \hat{x}, \quad (6.23)$$

where  $\hat{r}$  has been introduced as a shorthand notation. The transformation can be written in a more compact form using complex numbers:

$$\chi + i\psi = \Phi(\hat{x} + i\hat{y}) = \sqrt{2(\hat{x} + i\hat{y})} \quad (6.24)$$

$$\hat{x} + i\hat{y} = \Phi^{-1}(\chi + i\psi) = \frac{1}{2}(\chi + i\psi)^2. \quad (6.25)$$

It is worth noting that parabolic geometries have also been obtained by other authors studying steadily translating growth forms. The classical example are Ivantsov's dendrites [59]. In fact, Adda Bedia and Ben Amar [60] have shown that, at least in the context of steady state dendritic growth at zero surface tension, the parabolic solutions are the only admissible solutions once the Ivantsov ansatz is adopted and that even when one modifies this approach by making a more general ansatz, no new forms are found.

Once the shape of the finger is known, we can find the pressure and the concentration both inside and outside of it.

## Pressure field

Inside the finger ( $\chi < 1$ ), the pressure field satisfies the Laplace equation (6.1), which in the parabolic coordinates has the same simple form as in the Cartesian ones,

$$\frac{\partial^2 \hat{p}}{\partial \chi^2} + \frac{\partial^2 \hat{p}}{\partial \psi^2} = 0. \quad (6.26)$$

To proceed, one should note that the solvent transport equation inside the finger, Eq. (6.2), posed in the  $(\chi, \psi)$  coordinates is

$$\text{Pe}\kappa \frac{\partial \hat{p}}{\partial \chi} \frac{d\hat{c}}{d\chi} + \frac{d^2 \hat{c}}{d\chi^2} = 0. \quad (6.27)$$

Now it is straightforward to conclude that  $\partial_\chi \hat{p}$  must be a function of  $\chi$  only. Along with the fact that  $\hat{p}$  satisfies the Laplace equation (6.26), this gives, similarly as in the case of conformal mapping derivation,

$$\hat{p}(\chi, \psi) = -\frac{1}{2}A_0(\chi^2 - \psi^2) + A_1\chi + A_2\psi, \quad (6.28)$$

where the constant term has been dropped. However, the constants  $A_1$  and  $A_2$  have to be zero, otherwise the flow  $\hat{\mathbf{u}} = -\kappa \hat{\nabla} \hat{p}$  would diverge at  $\hat{\mathbf{r}} = 0$ .

Outside the dissolution finger, in the undissolved matrix, the pressure still obeys the Laplace equation,

$$\frac{\partial^2 \hat{p}}{\partial \chi^2} + \frac{\partial^2 \hat{p}}{\partial \psi^2} = 0. \quad (6.29)$$

The continuity conditions for  $\hat{p}$  and  $\hat{u}_n \equiv \hat{u}_\chi$  yield here

$$-\frac{1}{2}A_0(1 - \psi^2) = \hat{p}|_{\chi \rightarrow 1^+} \quad (6.30)$$

$$-\kappa A_0 = \left. \frac{\partial \hat{p}}{\partial \chi} \right|_{\chi \rightarrow 1^+}. \quad (6.31)$$

This is supplemented by the boundary condition (6.6)

$$-\hat{\nabla} \hat{p} \Big|_{\chi \rightarrow \infty} = \mathbf{e}_x = \hat{\nabla} \hat{x}, \quad (6.32)$$

which can be written in the  $(\chi, \psi)$  coordinates as

$$\lim_{\chi \rightarrow \infty} \frac{1}{\chi} \frac{\partial \hat{p}}{\partial \chi} = -1 \quad \lim_{\chi \rightarrow \infty} \frac{1}{\psi} \frac{\partial \hat{p}}{\partial \psi} = 1. \quad (6.33)$$

The solution of Eq. (6.29) fulfilling (6.30–6.33) is

$$\hat{p}(\chi, \psi) = -\frac{1}{2}(\chi^2 - \psi^2) - (\kappa - 1)(\chi - 1). \quad (6.34)$$

Additionally, the condition (6.31) gives  $A_0 = 1$  for the constant appearing in the solution of the internal problem, Eqs. (6.28).

To sum up, the pressure field in the system is

$$\hat{p}(\chi, \psi) = \begin{cases} -\frac{1}{2}(\chi^2 - \psi^2), & 0 \leq \chi \leq 1, \\ -\frac{1}{2}(\chi^2 - \psi^2) - (\kappa - 1)(\chi - 1), & \chi \geq 1. \end{cases} \quad (6.35)$$

Fig. 6.2 shows the pressure fields, plotted for various permeability contrasts  $\kappa$ , in the physical  $(x, y)$ -plane. Note that inside the finger the isobars are parallel to each other and oriented along the  $y$  direction, which is a manifestation of the fact that the flow is uniform there:

$$\hat{p}(\hat{x}, \hat{y}) = -\hat{x}, \quad \mathbf{r} \in \Omega, \quad (6.36)$$

$$\hat{\mathbf{u}}(\hat{x}, \hat{y}) = \kappa \mathbf{e}_x, \quad \mathbf{r} \in \Omega. \quad (6.37)$$

In the dimensional variables, the (constant) Darcy velocity inside the finger is

$$\mathbf{u}_{in} = \kappa u_0 \mathbf{e}_x \quad (6.38)$$

Outside the finger, in the undissolved domain  $\bar{\Omega}$ , the pressure field is

$$\hat{p}(\hat{x}, \hat{y}) = -\hat{x} - (\kappa - 1) \left( \sqrt{\hat{r} + \hat{x}} - 1 \right). \quad (6.39)$$

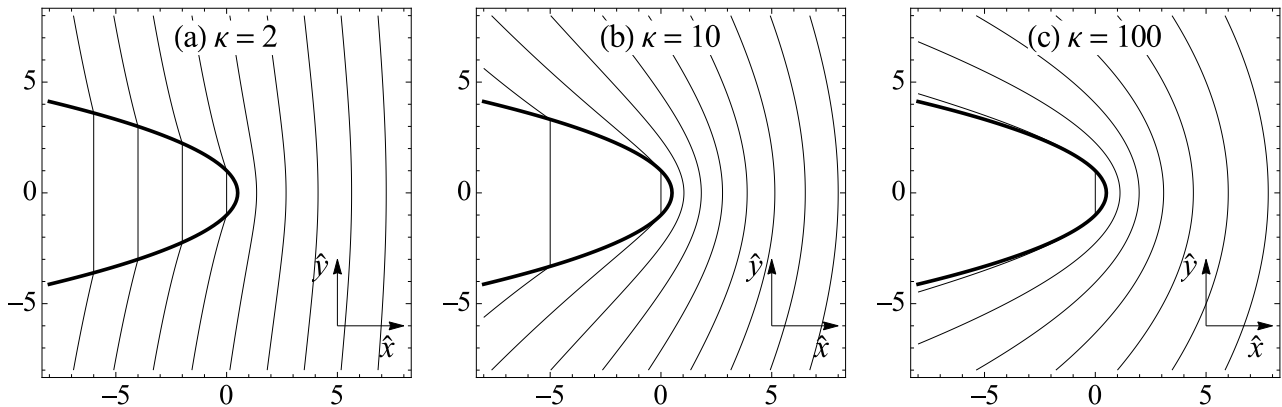


Figure 6.2: Pressure field inside and outside of the two-dimensional stationary dissolution finger (marked by the thick parabola), for different values of permeability contrasts: (a)  $\kappa = 2$ , (b)  $\kappa = 10$ , and (c)  $\kappa = 100$ . The (dimensionless) pressure drop between the neighbouring isobars is (a) 2, (b) 5, and (c) 50.

The term linear in  $\hat{x}$  dominates far from the boundary  $\partial\Omega$ , which agrees with the far-downstream condition for the flow field (6.6). Note that both the pressure field inside the finger (6.36) as well as that outside (6.39) obey the upstream boundary condition (3.10).

The above-obtained pressure field is analogous to that derived by Kacimov and Obnosov [69], who analyzed the groundwater flow in a porous medium with a parabolic inclusion. In fact the pressure problem solved in [69] is more general than that considered here, since it involved the far-field flow velocity oriented at an arbitrary angle with respect to the parabola axis, not necessarily parallel as in (6.6). Interestingly, in each case the flow within the parabola is found to be uniform. This is the parallel of the classical result by Poisson and Maxwell who noted that the electric field inside elliptic or ellipsoidal inclusions is uniform [70, 71], see also Carslaw and Jaeger [72] for the interpretation of this fact in the context of heat transfer.

Finally, let us note that the higher the permeability contrast  $\kappa$ , the more disturbed is the pressure field by the presence of the finger and the more aligned are the isobars along the reaction front. In the limit of  $\kappa \rightarrow \infty$ , the dissolution front  $\partial\Omega$  would correspond to one of the isobars.

### Solvent concentration field

As mentioned before, the solvent concentration field inside the finger is governed by the transport equation (6.27). Additionally, at the front itself, the reactant concentration vanishes, i.e.  $\hat{c}(\chi = 1) = 0$ . It is harder to formulate the second boundary condition for the concentration, necessary to close the equation. As mentioned in Chapter 2, the upstream condition in the form of Eq. (6.7) is inconsistent with the presence of the finger extending towards  $x \rightarrow -\infty$ . Instead, we need to prescribe the concentration within the finger. In accordance with the assumption that  $\hat{c}$  is a function of  $\chi$  only, we impose  $\hat{c} = 1$  on one of the parabolas, defined by  $\chi = \chi_0$  (see Fig. 6.3).

Inserting the resolved pressure field, Eq. (6.35), into the transport equation (6.27) yields the concentration field

$$\hat{c}(\chi) = \frac{\operatorname{erfi}\left(\sqrt{\frac{1}{2}\kappa\operatorname{Pe}}\chi\right) - \operatorname{erfi}\left(\sqrt{\frac{1}{2}\kappa\operatorname{Pe}}\right)}{\operatorname{erfi}\left(\sqrt{\frac{1}{2}\kappa\operatorname{Pe}}\chi_0\right) - \operatorname{erfi}\left(\sqrt{\frac{1}{2}\kappa\operatorname{Pe}}\right)}, \quad \chi_0 \leq \chi \leq 1, \quad (6.40)$$

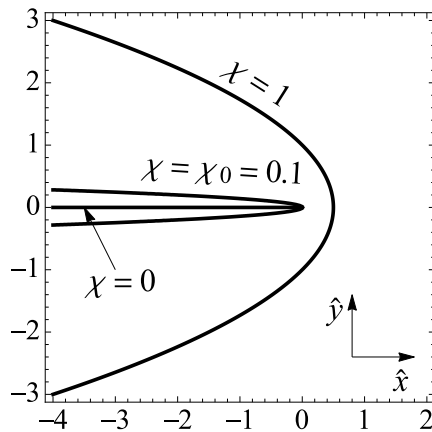


Figure 6.3: Schematic representation of the boundary conditions for the concentration field  $\hat{c}$  inside the parabolic dissolution finger. The finger is represented in the Cartesian coordinate system, with the  $x$  axis pointing rightwards and the lengths scaled by the radius of curvature  $\rho$ . The outer parabola, denoted by  $\chi = 1$ , constitutes the boundary of the finger and is characterized by vanishing of the reactants concentration,  $\hat{c}(\chi = 1) = 0$ . At the inner parabola of  $\chi = \chi_0$  (here  $\chi_0 = 0.1$ ) the boundary condition (3.11) is imposed,  $\hat{c}(\chi = \chi_0) = 1$ . Additionally, the line  $\chi = 0$  is shown.

where  $\operatorname{erfi}(x)$  is the imaginary error function defined as  $\operatorname{erfi}(x) \equiv \frac{2}{\sqrt{\pi}} \int_0^x e^{t^2} dt$ , and as mentioned above, the inlet concentration,  $\hat{c} = 1$ , has been imposed on the parabola  $\chi = \chi_0$  ( $0 \leq \chi_0 < 1$ ). As a special case, one can choose  $\chi_0 = 0$ , which yields

$$\hat{c}(\chi) = 1 - \frac{\operatorname{erfi}\left(\sqrt{\frac{1}{2}\kappa\text{Pe}}\chi\right)}{\operatorname{erfi}\left(\sqrt{\frac{1}{2}\kappa\text{Pe}}\right)}, \quad 0 \leq \chi \leq 1. \quad (6.41)$$

A closer inspection of Eq. (6.40) reveals that the relevant parameter controlling the concentration field is the product

$$\text{Pe}' = \kappa \text{Pe} = \frac{\rho u_{in}}{D(\varphi_1)}, \quad (6.42)$$

with  $u_{in}$  given by Eq. (6.38). This parameter is interpreted as the Péclet number related to the flow within the finger.

The impact of this parameter on the concentration profiles is analyzed in Fig. 6.4. For small values of  $\text{Pe}'$ , Eq. (6.40) is approximated by

$$\hat{c} \approx \frac{\chi - 1}{\chi_0 - 1}, \quad \chi_0 \leq \chi \leq 1, \quad (6.43)$$

i.e. the concentration depends linearly on the parabolic coordinate  $\chi$ . The gradient of the concentration field is then relatively uniform (cf. Fig. 6.4a). This situation can be referred to as the “diffusive” regime. In the opposite case of large  $\text{Pe}'$  (the “convective” regime), the concentration boundary layer is formed, with uniform concentration  $\hat{c} = 1$  in the body of the finger and high gradients near the boundary (Fig. 6.4c). In this limit the solutions found by us acquire direct physical relevance since a somewhat artificial choice of  $\chi_0$  becomes irrelevant here, as long as the parabola  $\chi = \chi_0$  lies in the bulk. By comparing the argument of  $\operatorname{erfi}$  in the numerator of Eq. (6.40) with unity,  $\chi\sqrt{\text{Pe}'/2} \sim 1$ , one can find the characteristic width of the boundary layer,  $\Delta\chi$ ,

$$\Delta\chi \sim \left(\frac{1}{2}\text{Pe}'\right)^{-\frac{1}{2}}. \quad (6.44)$$

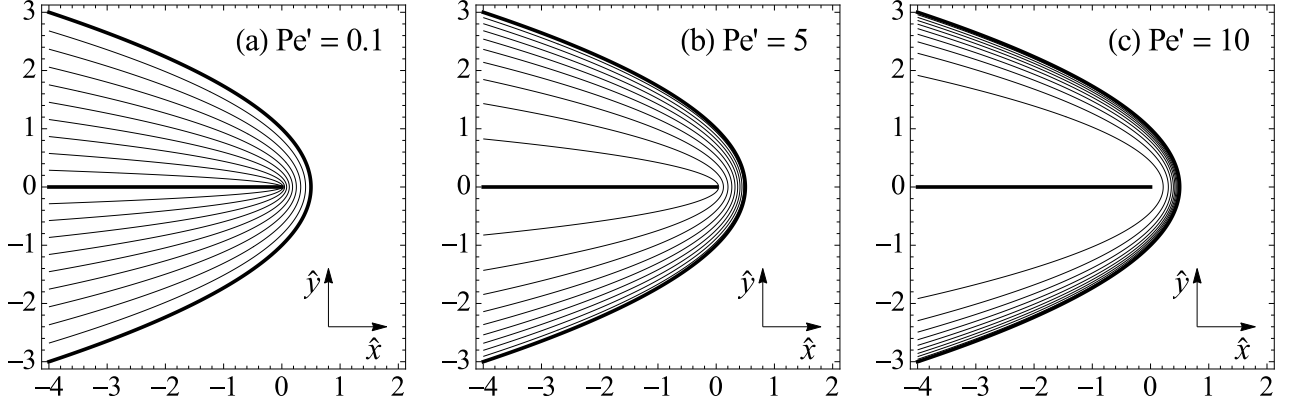


Figure 6.4: Reactant concentration field  $\hat{c}$  inside the two-dimensional stationary dissolution finger (marked by the thick parabola), for (a)  $Pe' = 0.1$ , (b)  $Pe' = 5$ , and (c)  $Pe' = 10$ . The boundary condition for the concentration (3.11), has been imposed on the line  $\chi = \chi_0 = 0$ . The (dimensionless) concentration drop between the neighbouring isolines of  $\hat{c}$  (thin parabolas) is set to 0.1. The boundary of the finger is also an isoline of the concentration (for  $\hat{c} = 0$ ).

The condition

$$\chi_0 \ll 1 - \left(\frac{1}{2}Pe'\right)^{-\frac{1}{2}} \quad (6.45)$$

guarantees that  $\chi_0$  lies in the bulk and thus its precise value does not affect the concentration profiles. This is confirmed by the comparison of  $\hat{c}$  profiles for  $Pe' = 10$  and  $\chi_0 = 0.05$  with those for  $\chi = 0.2$ , which are found to be almost indistinguishable, as shown in Fig. 6.5.

### Finger propagation velocity

Finally, Eq. (6.15) allows us to find the advancement velocity of the dissolution finger,

$$\hat{U} = -\frac{\hat{c}'(\chi)}{F(\hat{c}(\chi))\partial_{\chi}\hat{x}}\Big|_{\chi=1} = \frac{\sqrt{2}\kappa \exp\left(\frac{1}{2}Pe'\right)}{\sqrt{\pi} Pe' \left(\operatorname{erfi}\left(\sqrt{\frac{1}{2}Pe'}\right) - \operatorname{erfi}\left(\sqrt{\frac{1}{2}Pe'}\chi_0\right)\right)}, \quad (6.46)$$

where we have used the fact that  $F(\hat{c}(\chi = 1)) = Pe = Pe'/\kappa$ . Two limiting cases, corresponding to small/high values of  $Pe'$ , are given by

$$\lim_{Pe' \rightarrow 0} Pe \hat{U} = (1 - \chi_0)^{-1}, \quad (6.47)$$

$$\lim_{Pe' \rightarrow \infty} \hat{U} = \kappa. \quad (6.48)$$

The velocity scale is  $L/T = \gamma u_0$ . Thus in the limit of small  $Pe'$ , the dimensional finger advancement speed approaches

$$U \approx \frac{\gamma u_0}{Pe(1 - \chi_0)} = \frac{\gamma D(\varphi_1)}{\rho(1 - \chi_0)}, \quad (6.49)$$

i.e. it is inversely proportional to the radius of curvature of the tip. Such a behavior is in full analogy to the Ivantsov result for the dendrite propagation speed [59]. On the contrary, for large Péclet numbers the propagation velocity becomes constant with respect to the curvature of the finger tip and simply proportional to the Darcy velocity inside the finger,

$$U \approx \gamma u_0 \kappa = \gamma u_{in}. \quad (6.50)$$

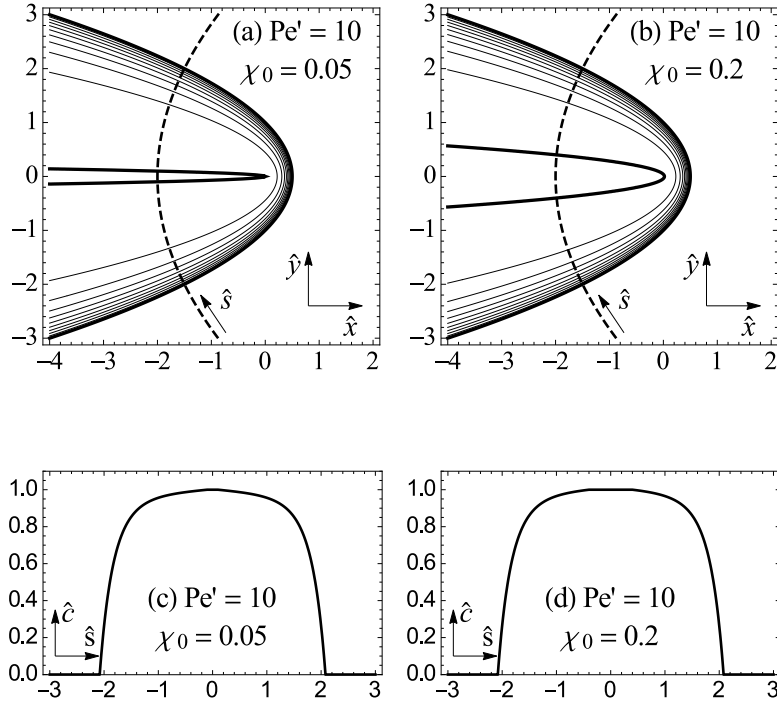


Figure 6.5: (a,b) Reactant concentration field  $\hat{c}$  inside the two-dimensional stationary dissolution finger in the “convective” regime, with  $Pe' = 10$ . The thick solid lines mark the finger boundary and the  $\chi = \chi_0$  parabola with (a)  $\chi_0 = 0.05$  and (b)  $\chi_0 = 0.2$ , on which the inlet concentration has been imposed,  $\hat{c}(\chi = \chi_0) = 1$ . The (dimensionless) concentration drop between the neighbouring isolines of  $\hat{c}$  (thin parabolas) is set to 0.1. The dashed line marks the parabola  $\psi = 2$  (locally orthogonal to the isolines of concentration) parametrized by the arc length  $\hat{s}$ . The reactant concentration profile along this parabola,  $\hat{c}(\hat{s})$ , is plotted in panels (c) and (d).

Notice the inherent indeterminacy of the general result (6.46): we have obtained the relation between the tip radius (via  $Pe'$ ) and the propagation speed with no means of evaluating each of these quantities independently. This is connected with the scale-invariance of the original equations (3.22–3.29) and can be lifted only after the introduction of an additional lengthscale. Again, this feature is shared by both the Ivantsov parabolas and the Saffman-Taylor fingers, which also represent families of growth forms and need the short-scale regularization mechanism such as surface tension or kinetic undercooling for the selection of a particular tip radius and advancement velocity. In the case of dissolution patterns, the additional lengthscale might originate from the reaction front width (assumed to be zero in our analysis) or from the interactions with other dissolution fingers: in real system, the finger is never infinite, but always constrained by the presence of its neighbours.

### Comparison with the Nilson & Griffiths model

At this point it is worth noting the main differences between our finger growth model and the one of Nilson and Griffiths [53]. Firstly, the boundary conditions at infinity are different. While we assume that the whole system is infiltrated by the reactive fluid (with a constant pressure gradient at  $x \rightarrow \infty$ ), Nilson & Griffiths assume constant pressure at  $x \rightarrow \infty$ , which means that the fluid far downstream ahead of the finger is kept immobile. In their model, however, the reactive fluid is constantly injected into the system, displacing the original pore fluid, so the latter becomes compressed. Such an assumption does not seem to be a realistic one for water under typical groundwater pressures. In another case considered in [53] the rock is initially unsaturated, with no fluid present in the pores. Then the reactive fluid enters the system, creating the finger and flooding the medium, which is associated with the formation of a 'product layer' of chemically equilibrated fluid ahead of the finger tip. Since no pressure gradient is imposed far downstream, the fluid in the product layer gradually slows down, as the thickness of the layer increases until it reaches a stationary situation in which both the finger and the product layer advance with equal velocities. Again, this is a fundamentally different situation from the one considered in the present work. In particular, the solution pipes shown in Fig. 1.4 were formed under the melting glacier, with gravity imposing the pressure gradient across the entire system.

There is yet another difference between our approaches, now related to the constraints on the values of physical parameters, under which the finger model is supposed to work. Similarly to us, Nilson & Griffiths adopt the thin-front approximation, stating that the reactant is entirely consumed immediately after reaching the finger boundary. As mentioned in Sec. 3.1, such a simplification is justified if  $H \gg 1$ . At the same time, however, it is assumed in [53] that the concentration of the reactant inside the finger is constant, so that the dissolution front velocity is proportional to the local fluid velocity. This is only possible if the advection within the finger dominates over the diffusive transport, i.e. the Péclet number  $Pe' = u_{in}L/D \gg 1$ , which puts rather stringent constraints on the admissible values of  $D$ ,  $u_{in}$  and the reaction rate. The flow rates should be on one hand sufficiently large (to keep the transport advective within the finger), but on the other hand, since  $H \propto |u|^{-2}$ , small enough to keep the reaction front thin. In our study the constraints on the admissible parameters are much broader, since while keeping the front thin, we fully resolve the concentration field inside the finger, and thus obtain the finger propagation velocities over the entire range of Péclet numbers, cf. Eq. (6.46). At smaller  $Pe'$ , the effects connected with the buildup of a diffusive layer of the depleted reactant appear [42], which have a significant impact on the wormhole propagation speed.

Similarly as in our case, Nilson & Griffiths recover a whole family of parabolic wormholes, which propagate with different velocities. However, the differences in the boundary conditions between our model and theirs result in different relations between the finger propagation velocity

and the curvature of its tip. Let us recall that the model of Nilson & Griffiths is supposed to be valid for high Péclet numbers. Their wormholes propagate with the velocity proportional to their tip curvature. We also recover a similar scaling,  $U \propto \rho^{-1}$ , but only in the opposite regime of small Péclet numbers. On the contrary, for large  $Pe'$  the finger propagation velocity is independent from its curvature.

In some respect Nilson & Griffiths go one step further than we do and aim to find the regularization mechanism, which would select a certain parabolic solution from the whole family. They manage to do this, however paying a price of introducing another assumption to their model, namely that the chemical reaction is a zeroth order one, i.e. the reaction rate does not depend on the concentration of the reactants. They also make use of the specific nature of their wormholes, which are surrounded by the “product layer” of the fluid which came through them. The purely chemical regularization mechanism which they propose indeed seems to select a particular solution, however it is arguable whether its presence does not violate the initial assumption that the reaction front is thin.

### 6.1.2 Three-dimensional stationary dissolution fingers

In this section we study the geometry of three-dimensional dissolution fingers. The physical, Cartesian coordinates will be denoted by the letters  $x, y, z$  (while the spatial coordinates scaled by the yet undefined length scale  $L$  are  $\hat{x}, \hat{y}, \hat{z}$ ). In the following, we will assume that the fluid flow is directed along the  $z$  axis.

#### Ivantsov’s ansatz and finger geometry

Similarly as in the two-dimensional case, we assume the Ivantsov ansatz as well as the stationarity of the fingers, so the starting point of our investigations is the following set of equations for the pressure and concentration inside the finger

$$\kappa \hat{\nabla} \hat{p} \cdot \hat{\nabla} \hat{c} + Pe^{-1} \hat{\nabla}^2 \hat{c} = 0 \quad (6.51a)$$

$$\hat{\nabla}^2 \hat{p} = 0 \quad (6.51b)$$

$$\hat{\nabla} \hat{c} \cdot (F(\hat{c}) \hat{U} \hat{\nabla} \hat{z} + \hat{\nabla} \hat{c}) = 0. \quad (6.51c)$$

As before, on the boundary of the finger we put  $\hat{c} = 0$  and  $F = Pe$ . In the region outside the finger the pressure obeys the Laplace equation whereas the concentration vanishes.

Let us switch to the cylindrical coordinate system,  $(\hat{x}, \hat{y}, \hat{z}) \rightarrow (\hat{r}, \phi, \hat{z})$  and look for the solutions with rotational invariance, i.e. independent of  $\phi$ . Eqs. (6.51) in the new variables take the form

$$\kappa Pe \hat{\nabla}_{rz} \hat{p} \cdot \hat{\nabla}_{rz} \hat{c} + \hat{\nabla}_{rz}^2 \hat{c} + \frac{1}{\hat{r}} \frac{\partial \hat{c}}{\partial \hat{r}} = 0 \quad \mathbf{r} \in \Omega(\hat{t}) \quad (6.52a)$$

$$\hat{\nabla}_{rz}^2 \hat{p} + \frac{1}{\hat{r}} \frac{\partial \hat{p}}{\partial \hat{r}} = 0 \quad \mathbf{r} \in \Omega(\hat{t}) \quad (6.52b)$$

$$\hat{\nabla}_{rz} \hat{c} \cdot (F(\hat{c}) \hat{U} \hat{\nabla}_{rz} \hat{z} + \hat{\nabla}_{rz} \hat{c}) = 0 \quad \mathbf{r} \in \Omega(\hat{t}) \quad (6.52c)$$

where  $\hat{\nabla}_{rz} = (\partial_{\hat{r}}, \partial_{\hat{z}})$  acts as if the  $(\hat{r}, \hat{z})$  were Cartesian coordinates. Similarly,  $\hat{\nabla}_{rz}^2 = \partial_{\hat{r}}^2 + \partial_{\hat{z}}^2$ .

Analogously to the previous case we are looking for a conformal map  $(\hat{z}, \hat{r}) \rightarrow (\chi, \psi)$  such that  $\hat{c}$  becomes a function of one variable only,  $\hat{c} = \hat{c}(\chi)$ . Again, from Eq. (6.52c) we draw the conclusion that such a map needs to be a parabolic one,

$$\hat{z} = \frac{1}{2}(\chi^2 - \psi^2) \quad (6.53a)$$

$$\hat{r} = \chi\psi, \quad (6.53b)$$

with the radius of curvature of the finger chosen as the length unit. As before, we assume that the finger boundary coincides with the  $\chi = 1$  paraboloid.

### Pressure field

Let us now use this mapping to solve the Laplace equation for the pressure inside and outside the dissolution finger. Since the Lamé coefficients  $h_\chi, h_\psi$  for the transformation (6.53) are equal to

$$h_\chi = \left| \frac{d\hat{\mathbf{r}}}{d\chi} \right| = \sqrt{\left( \frac{\partial \hat{r}}{\partial \chi} \right)^2 + \left( \frac{\partial \hat{z}}{\partial \chi} \right)^2} = \sqrt{\chi^2 + \psi^2}, \quad (6.54)$$

$$h_\psi = \left| \frac{d\hat{\mathbf{r}}}{d\psi} \right| = \sqrt{\left( \frac{\partial \hat{r}}{\partial \psi} \right)^2 + \left( \frac{\partial \hat{z}}{\partial \psi} \right)^2} = \sqrt{\chi^2 + \psi^2} = h_\chi, \quad (6.55)$$

equation (6.52a) written in terms of  $\chi$  and  $\psi$  becomes

$$\text{Pe}' \frac{\partial \hat{p}}{\partial \chi} \hat{c}'(\chi) + \hat{c}''(\chi) + \frac{1}{\chi} \hat{c}'(\chi) = 0. \quad (6.56)$$

Its form suggests that  $\partial_\chi \hat{p}$  is a function of  $\chi$  only and thus the pressure field  $\hat{p}$  inside the dissolution finger is separable into

$$\hat{p}(\chi, \psi) = X(\chi) + Y(\psi). \quad (6.57)$$

The Laplace equation for the pressure inside the dissolution finger, Eq. (6.52b), in the  $\chi, \psi$  coordinates transforms into

$$\frac{\partial^2 \hat{p}}{\partial \chi^2} + \frac{\partial^2 \hat{p}}{\partial \psi^2} + \frac{1}{\chi} \frac{\partial \hat{p}}{\partial \chi} + \frac{1}{\psi} \frac{\partial \hat{p}}{\partial \psi} = 0, \quad 0 \leq \chi < 1. \quad (6.58)$$

Inserting (6.57) into Eq. (6.58) gives the result that the pressure field inside the dissolution finger should be of the form

$$\hat{p}(\chi, \psi) = -\frac{1}{2} C_0 (\chi^2 - \psi^2) + C_1 \ln \chi + C_2 \ln \psi + C_3, \quad 0 \leq \chi < 1. \quad (6.59)$$

We immediately set  $C_1 = C_2 = 0$ , to avoid singularities at  $\chi = 0$  or  $\psi = 0$ , while the constants  $C_0$  and  $C_3$  are to be determined from the boundary and the continuity conditions. Next, we look for the solution of the Laplace equation for the pressure field outside of the finger of the same functional form as that inside,

$$\hat{p}(\chi, \psi) = -\frac{1}{2} D_0 (\chi^2 - \psi^2) + D_1 \ln \chi + D_2 \ln \psi, \quad \chi > 1. \quad (6.60)$$

where the constant term has been skipped.

The continuity conditions and the far-downstream boundary condition for the flow are analogous to the two-dimensional case (Eqs. (3.9–3.31)). The downstream boundary condition yields  $D_0 = 1$ . The continuity of the pressure and the normal component of the flux at the finger boundary  $\chi = 1$  yields  $D_2 = C_3 = 0$ ,  $C_0 = 1$  and  $D_1 = 1 - \kappa$ .

Eventually, the pressure field in the whole space is

$$\hat{p}(\chi, \psi) = \begin{cases} -\frac{1}{2}(\chi^2 - \psi^2) & 0 \leq \chi \leq 1 \\ -\frac{1}{2}(\chi^2 - \psi^2) - (\kappa - 1) \ln \chi & \chi \geq 1, \end{cases} \quad (6.61)$$

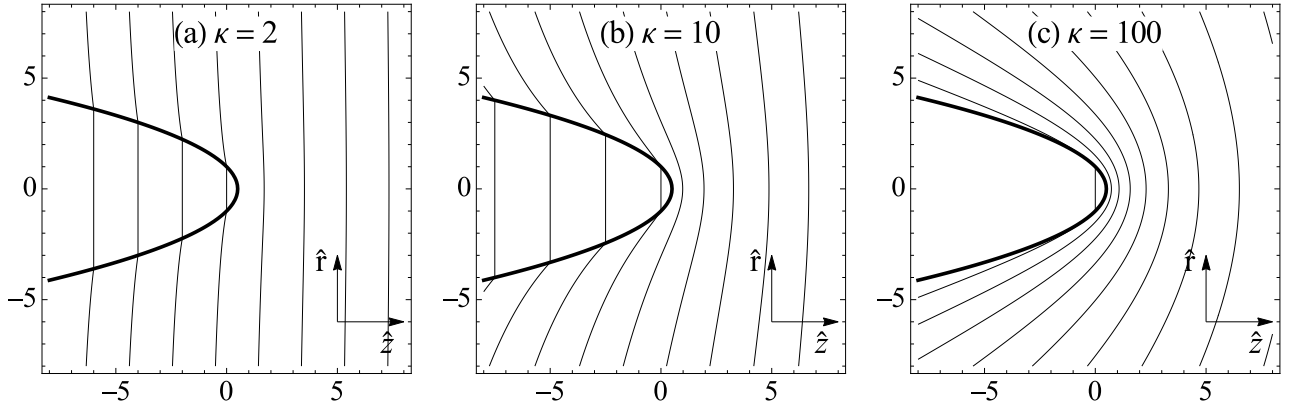


Figure 6.6: Pressure field inside and outside of the three-dimensional stationary dissolution finger. The cross-section of the finger is shown, with the finger boundary marked by a thick parabola. The pressure field is plotted for different values of permeability contrast: (a)  $\kappa = 2$ , (b)  $\kappa = 10$ , and (c)  $\kappa = 100$ . The (dimensionless) pressure drop between the neighbouring isobars is (a) 2, (b) 2.5, and (c) 10.

or, in the Cartesian coordinates,

$$\hat{p}(\hat{z}, \hat{r}) = \begin{cases} -\hat{z} & 0 \leq \sqrt{\hat{z}^2 + \hat{r}^2} + \hat{z} \leq 1 \\ -\hat{z} - \frac{\kappa - 1}{2} \ln(\sqrt{\hat{z}^2 + \hat{r}^2} + \hat{z}) & \sqrt{\hat{z}^2 + \hat{r}^2} + \hat{z} \geq 1, \end{cases} \quad (6.62)$$

This solution has been plotted in Fig. 6.6 for different values of the permeability contrast,  $\kappa$ . The overall picture is similar to that in the two-dimensional case, with a uniform flow inside the finger and the flow disturbance around it relaxing to a uniform flow field far downstream. For small values of the permeability contrast  $\kappa$ , the presence of the finger does not significantly disturb the isobars, whereas in the opposite case the isobars become almost parallel to the finger boundary.

### Solvent concentration field

Using (6.61) one can solve Eq. (6.56) and find the concentration field inside the finger. The solution can be written in terms of the exponential integral function  $\text{Ei}(x) = -\int_{-x}^{\infty} t^{-1} e^{-t} dt$ ,

$$\hat{c}(\chi) = \frac{\text{Ei}(\frac{1}{2}\text{Pe}'\chi^2) - \text{Ei}(\frac{1}{2}\text{Pe}')}{\text{Ei}(\frac{1}{2}\text{Pe}'\chi_0^2) - \text{Ei}(\frac{1}{2}\text{Pe}')}, \quad \chi_0 < \chi < 1, \quad (6.63)$$

where, as before, we set the condition  $\hat{c} = 1$  on the parabola  $\chi = \chi_0$  (with  $0 < \chi_0 < 1$ ). The concentration fields for various parameters have been plotted in Fig. 6.7. Qualitatively, the behavior is similar to the one observed for the 2D case. The “diffusive” regime is observed for small values of  $\text{Pe}'$  (see Fig. 6.7a) and is characterized by relatively uniform distribution of the concentration gradient. In this case, the concentration field can be approximated by<sup>2</sup>

$$\hat{c}(\chi) \approx \frac{\ln \chi}{\ln \chi_0}, \quad \chi_0 < \chi < 1. \quad (6.64)$$

<sup>2</sup>Expanding the exponential integral function for small arguments yields  $\text{Ei}(x) = \gamma_E + \ln x + x + O(x^2)$ , where  $\gamma_E \approx 0.5772$  is the Euler-Mascheroni constant.

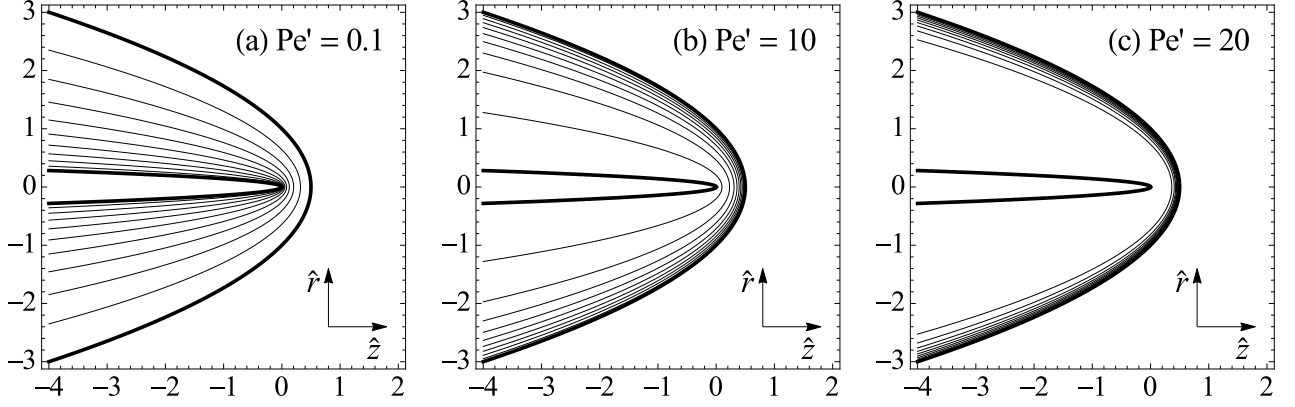


Figure 6.7: Reactant concentration field  $\hat{c}$  in the cross-section of the three-dimensional stationary dissolution finger, for (a)  $Pe' = 0.1$ , (b)  $Pe' = 5$ , and (c)  $Pe' = 20$ . The parameter  $\chi_0$  was chosen to be 0.1. The (dimensionless) concentration drop between the neighbouring isolines is set to 0.1.

In the opposite case of high  $Pe'$  (see Fig. 6.7c), the boundary layer characterized by high gradients of the concentration  $\hat{c}$  is formed near the finger boundary, while in the interior of the finger the  $\hat{c}$  field is almost uniform. The characteristic width of the boundary layer in the  $(\chi, \psi)$ -plane is, similarly as in the 2D case, equal to  $(\frac{1}{2}Pe')^{-1/2}$ , which sets the constraint on the choice of  $\chi_0$ , analogous to the two-dimensional one (Eq. (6.45)).

The only significant difference between the 3D and the 2D cases is that in 3D we cannot demand  $\chi_0 = 0$ , since the Ei function diverges at zero and the solution becomes singular. However, this constraint becomes irrelevant in the “convective” regime ( $Pe' \gg 1$ ), since then  $\hat{c} \approx 1$  throughout the bulk of the finger.

### Finger propagation velocity

Finally, the finger propagation velocity, derived analogously to the 2D case, is given by

$$\hat{U} = -\left. \frac{\hat{c}'(\chi)}{F(\hat{c}(\chi))\partial_\chi \hat{z}} \right|_{\chi=1} = \frac{2\kappa(Pe')^{-1} \exp(\frac{1}{2}Pe')}{\text{Ei}(\frac{1}{2}Pe') - \text{Ei}(\frac{1}{2}Pe'\chi_0^2)}, \quad (6.65)$$

with the limiting cases characterized by

$$\lim_{Pe' \rightarrow 0} Pe' \hat{U} = -(\ln \chi_0)^{-1}, \quad (6.66)$$

$$\lim_{Pe' \rightarrow \infty} \hat{U} = \kappa. \quad (6.67)$$

Again, there is a significant similarity with the 2D case. The (dimensional) propagation velocity of dissolution fingers at small Péclet numbers is inversely proportional to  $\rho$ ,

$$U \approx -\frac{\gamma u_0}{Pe \ln \chi_0} = -\frac{\gamma D(\varphi_1)}{\rho \ln \chi_0}, \quad (6.68)$$

whereas at high Péclet numbers the propagation velocity becomes independent of the radius of curvature and yields

$$U \approx \gamma u_{in}. \quad (6.69)$$

### 6.1.3 Natural solution pipes

Geological studies of the solution pipe system in Smerdyna [5] (Fig. 1.4) suggest that they were formed at the end of the Elsterian glaciation, when huge amounts of meltwater were infiltrating the bedrock. Such mildly acidic water was able to dissolve the underlying calcite. It was a typical reactive-infiltration system: nonlinear couplings between the fluid flow, chemical activity, and permeability evolution led to the formation of the pipe network. At the area of approximately  $S = 2 \text{ km}^2$ , the pipe density is  $0.16/\text{m}^2$ . They cover about 6.1% of the surface area. The average volume of a pipe is approx.  $1 \text{ m}^3$ , which gives the host rock removal volume of  $\Delta V/S \approx 1600 \text{ m}^3/\text{ha} = 16 \text{ cm}$ .

Relatively simple mass balance considerations allow us to assess the total meltwater fluxes which the area had to receive during the deglaciation so that such an extensive pipe network could be formed. Cold meltwater was most probably mildly acidic, of  $pH \approx 5$ , which translates to the hydrogen cation concentration of  $c_{in} = [\text{H}^+] \approx 10^{-5} \text{ mol/L}$ . The equilibrium concentration of  $\text{H}^+$  is of the order of  $c_{eq} \approx 10^{-8} \text{ mol/L} \ll c_{in}$ . Taking into account the molar volume of calcite,  $\nu = 31.2 \text{ cm}^3/\text{mol}$ , and the porosity of the bedrock,  $\varphi_0 \approx 30\%$ , the acid capacity number can be estimated as

$$\gamma \approx \frac{\nu c_{in}}{1 - \varphi_0} \approx 5 \cdot 10^{-7}. \quad (6.70)$$

Consequently, the whole area had to receive the total volume of meltwater equal to

$$V_w = \gamma^{-1} S \cdot \Delta V/S = 10^4 \text{ km}^3, \quad (6.71)$$

which translates to the water column of height

$$V_w/S = 10^4 \text{ km}^3/2 \text{ km}^2 = 5 \cdot 10^3 \text{ km}. \quad (6.72)$$

This is four orders of magnitude more than the estimated height of the glacial cover (500 m). The above estimation was apparently overlooked by geologists studying the piping system [73, 5]. It suggests that the area was infiltrated by meltwater originating from quite distant sources, and was presumably transported by a river network developed on the surface or under the glacier. The host rock near Smerdyna is highly porous (ca. 30%), which might explain why this particular area was a convenient place for meltwater to infiltrate into deeper groundwater reservoirs.

The time scale of the overall process is more difficult to estimate. An upper bound can be given as the length of the Elsterian glacial period (400-320 ky ago):  $\Delta t < 8 \cdot 10^4$  years. Another estimate can be provided by studying footprints of the last (Weichsel a.k.a. Vistulian) glaciation, which are easier to study than its older counterparts. In principle, surface exposure dating based on measurements of the cosmogenic  $^{36}\text{Cl}$  content can be used to track the glacier withdrawal. Such studies reveal that typical time scales of this process were  $\Delta t = 10^3 - 10^4$  years [74]. Taking  $\Delta t = 10^4$  years as the reference value, we can estimate the mean Darcy velocity of the infiltrating water,

$$u_0 = \gamma^{-1} \Delta V / (S \Delta t) = 44 \text{ cm/day}. \quad (6.73)$$

Since the geometry of the pipes can be measured, it is in principle possible to estimate the Péclet number characterizing the environmental conditions under which the pipes were formed. The radii of curvature of the tips of the solution pipes presented in Fig. 1.4 (bottom) are  $\rho \approx 20 \text{ cm}$ . Next, we estimate the molecular diffusivity to be  $D_{mol} \approx 10^{-5} \text{ cm}^2/\text{s}$ , which is a typical order of magnitude for the diffusion coefficient of small molecules under normal conditions. The porosity difference between the limestone and the pipe fill is approximately 10%. Consequently, the Péclet number can be approximated as

$$\text{Pe} = \frac{u_0 \rho}{\varphi_1 D_{mol}} \approx 2.5 \cdot 10^3 \gg 1. \quad (6.74)$$

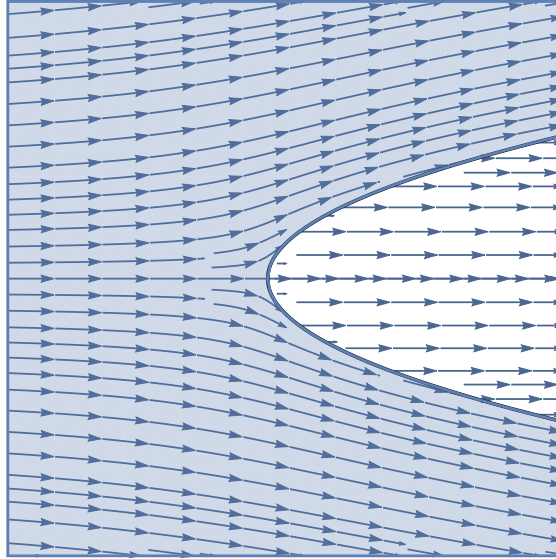


Figure 6.8: A schematic picture showing a root (the white region) surrounded by the totally dissolved matrix (the shaded region). The thin arrowed lines represent streamlines of the Darcy flow.

The solution pipes were formed in the high Péclet number regime.

The 10% porosity difference between the rocks typically corresponds to the permeability contrast of  $\kappa \approx 10$  [75]. Thus, according to (6.69), the longest wormhole length can be estimated as  $U\Delta t = \gamma u_0 \kappa \Delta t \approx 8$  m. Up to the order of magnitude, this estimate is consistent with the field observations.

## 6.2 Stationary roots

Reasoning analogous to the one presented in Section 6.1 can be applied to find another family of invariantly propagating dissolution forms. Contrary to the dissolution fingers which are convex, these forms are concave. These concave forms will be dubbed “roots”. The tips of the roots are the local minima of the curve representing the reaction front,  $\xi = \zeta(\eta; \tau)$  (contrary to the fingers, whose tips are the local maxima). A single root is sketched in Fig. 6.8. As one can easily deduce, the fluid flow should go mainly around the root. However, if the permeability contrast  $\kappa$  is finite, one might expect that some part of the fluid penetrates it as well. In this chapter we will pose the problem of finding the geometry of an invariantly translating root. Our intuitions regarding the flow in the vicinity of such a root will also be verified.

### 6.2.1 Two-dimensional stationary roots

In Sec. 6.1.1, while looking for the geometry of stationary two-dimensional fingers, we adopted the Ivantsov’s ansatz. As a result, we were able to find the conformal transformation from the Cartesian coordinates to the coordinates coinciding with the isolines of the reactant concentration. It turned out that the transformation has to be a parabolic one, Eqs. (6.19). Next, we identified the radius of curvature of the finger’s tip  $\rho$  as the length scale  $L$ , making a silent assumption that the finger is convex, i.e. its tip’s curvature is positive. However, one can also consider concave dissolution forms. Then the length scale should be rather set as  $L = -\rho$ .

Consequently, the desired conformal transformation is

$$\hat{x}(\chi, \psi) = -\frac{1}{2}(\chi^2 - \psi^2), \quad (6.75)$$

$$\hat{y}(\chi, \psi) = -\chi\psi, \quad (6.76)$$

and the inverse one is

$$\chi^2 = \sqrt{\hat{x}^2 + \hat{y}^2} - \hat{x} = \hat{r} - \hat{x} \quad (6.77)$$

$$\psi^2 = \sqrt{\hat{x}^2 + \hat{y}^2} + \hat{x} = \hat{r} + \hat{x}. \quad (6.78)$$

Again, both the  $\chi$  and  $\psi$  coordinates vary between zero and infinity,  $0 \leq \chi, \psi < \infty$ . The transformation  $(\hat{x}, \hat{y}) \rightarrow (\chi, \psi)$  and its inverse can be written in a compact, complex form,

$$\hat{x} + i\hat{y} = -\frac{1}{2}(\chi + i\psi)^2, \quad (6.79)$$

$$\chi + i\psi = \sqrt{-2(\hat{x} + i\hat{y})}. \quad (6.80)$$

Without much loss of generality we can identify the parabola  $\chi = 1$  with the boundary between the dissolved and the undissolved domains. Now the dissolved domain (the root) is located in the interior of the parabola,  $0 \leq \chi < 1$ .

## Pressure field

Similarly as in the finger problem (Sec. 6.1), we apply the Ivantsov's ansatz and conclude that in the dissolved domain ( $\chi > 1$ ) the pressure field is separable into a sum of two functions dependent on, respectively,  $\chi$  and  $\psi$ . The general solution of the Laplace equation for the pressure is then

$$\hat{p}(\chi, \psi) = \frac{1}{2}A_0(\chi^2 - \psi^2) + A_1\chi + A_2\psi. \quad (6.81)$$

Far from the reaction front ( $\chi \rightarrow \infty$ ) the flow velocity should be uniform,

$$-\kappa \hat{\nabla} \hat{p} \sim \hat{\nabla} \hat{x}, \quad (6.82)$$

so

$$A_0 = \frac{1}{\kappa} \quad \text{and} \quad A_2 = 0. \quad (6.83)$$

Note that now, contrary to the finger case, the condition (6.82) has to be imposed upstream from the dissolution front, in the dissolved phase (cf. Eq. (6.32)).

Within the undissolved root ( $0 \leq \chi < 1$ ) pressure also obeys the Laplace equation. The only admissible solution is similar to the one outside the root,

$$\hat{p}(\chi, \psi) = \frac{1}{2}A'_0(\chi^2 - \psi^2) + A_3\chi + A_4\psi + A_5. \quad (6.84)$$

However, in order to avoid singularities in the pressure or velocity field at  $\chi = 0$ , we have to demand that  $A_3 = 0$ . The continuity of the pressure field and of the normal velocity at the boundary  $\chi = 1$  yield

$$A'_0 = \frac{1}{\kappa}, \quad A_4 = 0, \quad A_1 = -\frac{\kappa - 1}{\kappa^2}, \quad \text{and} \quad A_5 = -\frac{\kappa - 1}{\kappa^2}. \quad (6.85)$$

. Eventually, the pressure field inside and outside the root is equal to

$$\hat{p}(\chi, \psi) = \begin{cases} \frac{1}{2\kappa}(\chi^2 - \psi^2) - \frac{\kappa - 1}{\kappa^2}, & 0 \leq \chi < 1, \\ \frac{1}{2\kappa}(\chi^2 - \psi^2) - \frac{\kappa - 1}{\kappa^2}\chi, & \chi > 1, \end{cases} \quad (6.86)$$

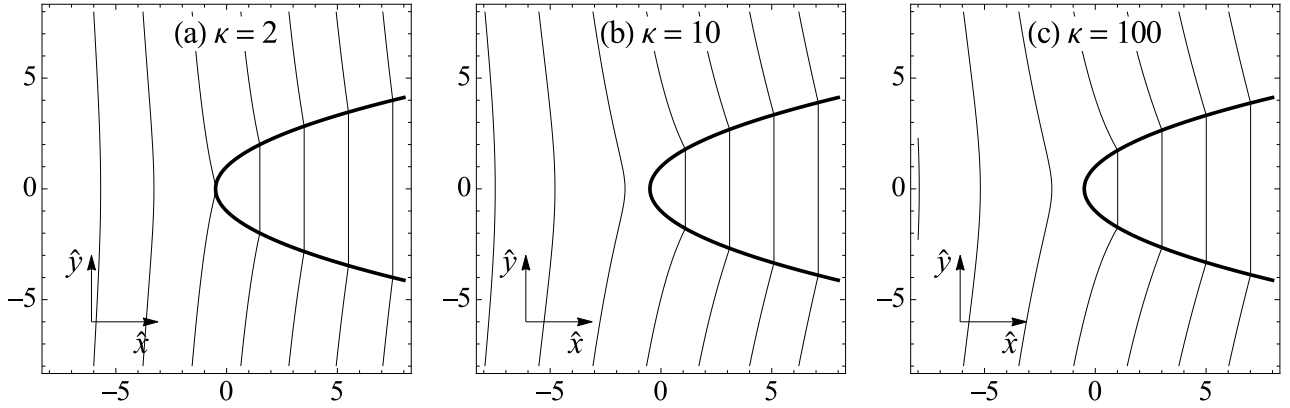


Figure 6.9: Pressure field inside and outside of the two-dimensional stationary root (marked by the thick parabola), for different values of permeability contrasts  $\kappa$ , (a)  $\kappa = 2$ , (b)  $\kappa = 10$ , and (c)  $\kappa = 100$ . The (dimensionless) pressure drop between the neighbouring isobars is (a) 1, (b) 0.2, and (c) 0.02.

or, in the Cartesian coordinates,

$$\hat{p}(\hat{x}, \hat{y}) = \begin{cases} -\frac{1}{\kappa}\hat{x} - \frac{\kappa - 1}{\kappa^2}, & 0 \leq \hat{r} - \hat{x} < 1, \\ -\frac{1}{\kappa}\hat{x} - \frac{\kappa - 1}{\kappa^2}\sqrt{\hat{r} - \hat{x}}, & \hat{r} - \hat{x} > 1. \end{cases} \quad (6.87)$$

The pressure field is illustrated in Fig. 6.9. The flow velocity within the root is uniform, similarly as it was within the dissolution finger. As the permeability contrast  $\kappa$  grows, the isobars around the root ( $\chi \gtrsim 1$ ) become more and more perpendicular to the dissolution front. Consequently, much less flow penetrates the root. In the limit of  $\kappa \rightarrow \infty$  the dissolution front becomes a flow line and it is no longer penetrated by the fluid.

### Solvent concentration field

In the dissolved phase around the root ( $\chi > 1$ ) the solvent concentration satisfies the advection-diffusion equation, which posed in the  $(\chi, \psi)$  coordinates<sup>3</sup> reads

$$\text{Pe}\kappa \frac{\partial \hat{p}}{\partial \chi} \hat{c}'(\chi) + \hat{c}''(\chi) = 0. \quad (6.88)$$

Along with the boundary conditions  $\hat{c}(\chi = 1) = 0$ , and  $\hat{c}(\chi \rightarrow \infty) = 1$ , this equation yields the solution

$$\hat{c}(\chi, \psi) = \begin{cases} 0, & 0 \leq \chi < 1, \\ \frac{\text{erf}\left(\sqrt{\frac{1}{2}\text{Pe}}(\chi - 1 + \frac{1}{\kappa})\right) - \text{erf}\left(\frac{1}{\kappa}\sqrt{\frac{1}{2}\text{Pe}}\right)}{1 - \text{erf}\left(\frac{1}{\kappa}\sqrt{\frac{1}{2}\text{Pe}}\right)}, & \chi > 1, \end{cases} \quad (6.89)$$

where the error function  $\text{erf}$  is defined as  $\text{erf}(z) = \frac{2}{\sqrt{\pi}} \int_0^z e^{-t^2} dt$ . Returning to the Cartesian coordinates, the solvent concentration field is

$$\hat{c}(\hat{x}, \hat{y}) = \begin{cases} 0 & 0 \leq \hat{r} - \hat{x} < 1, \\ \frac{\text{erf}\left(\sqrt{\frac{1}{2}\text{Pe}}(\sqrt{\hat{r} - \hat{x}} - 1 + \frac{1}{\kappa})\right) - \text{erf}\left(\frac{1}{\kappa}\sqrt{\frac{1}{2}\text{Pe}}\right)}{1 - \text{erf}\left(\frac{1}{\kappa}\sqrt{\frac{1}{2}\text{Pe}}\right)} & \hat{r} - \hat{x} > 1. \end{cases} \quad (6.90)$$

<sup>3</sup>And similarly as in Sec. 6.1 we assume that the isolines of concentration coincide with the curves  $\chi = \text{const}$ .

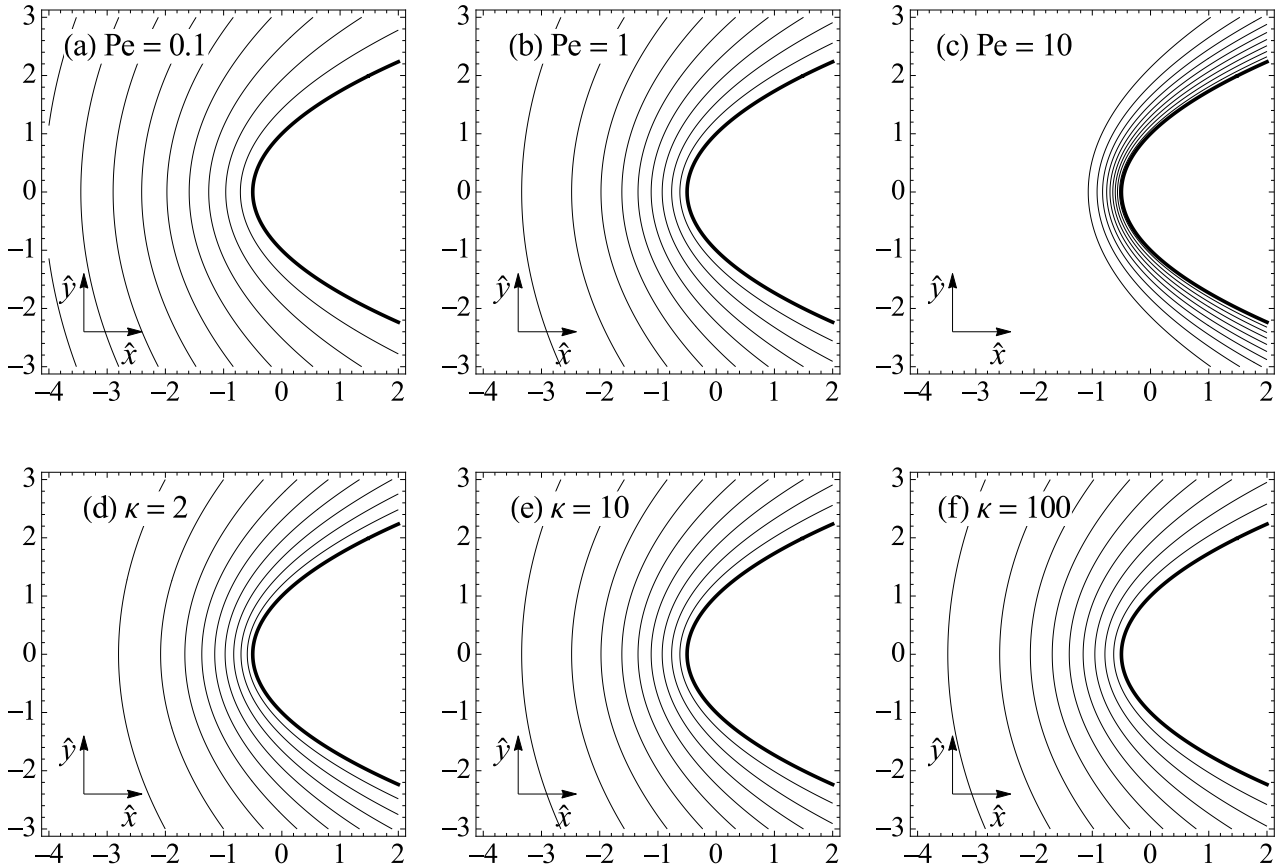


Figure 6.10: Reactant concentration field  $\hat{c}$  outside the two-dimensional stationary root (marked by the thick parabola). Top row:  $\kappa = 10$  and (a)  $Pe = 0.1$ , (b)  $Pe = 1$ , (c)  $Pe = 10$ . Bottom row:  $Pe = 1$  and (d)  $\kappa = 2$ , (e)  $\kappa = 10$ , (f)  $\kappa = 100$ . The (dimensionless) concentration drop between the neighbouring isolines of  $\hat{c}$  (thin parabolas) is set to 0.1. The boundary of the finger is also an isoline of the concentration (for  $\hat{c} = 0$ ).

The solution is illustrated in Fig. 6.10. Obviously, the concentration is zero within the root and the parabolic dissolution front (the boundary of the root) is an isoline of the concentration,  $\hat{c}(\chi = 1) = 0$ . For small Péclet numbers the concentration gradients are relatively small — the diffusion is the dominant transport mechanism in the vicinity of the root. For large  $Pe$ , however, the concentration is equal to almost unity everywhere except for a thin boundary layer near the dissolution front, where high concentration gradients are observed. The characteristic width of such a layer,  $\Delta\chi$ , can be estimated by comparing the argument of the first error function in the numerator of Eq. (6.89) with unity,

$$\sqrt{\frac{Pe}{2}}(\Delta\chi + \kappa^{-1}) \sim 1. \quad (6.91)$$

Consequently,

$$\Delta\chi \sim \sqrt{\frac{2}{Pe}} - \kappa^{-1} \xrightarrow{\kappa \rightarrow \infty} \sqrt{\frac{2}{Pe}}, \quad (6.92)$$

which is in fact valid for both low and high Péclet numbers. Returning to the Cartesian coordinates, the width of the boundary layer along the root axis of symmetry ( $\hat{y} = 0$ ),  $\Delta\hat{x}$ , is

of the order of<sup>4</sup>

$$\Delta\hat{x} = \frac{1}{2}(\Delta\chi)^2 + \Delta\chi \sim \frac{1}{2} \left( \sqrt{\frac{2}{\text{Pe}}} - \frac{1}{\kappa} \right)^2 + \sqrt{\frac{2}{\text{Pe}}} - \frac{1}{\kappa} \xrightarrow{\kappa \rightarrow \infty} \frac{1}{\text{Pe}} + \sqrt{\frac{2}{\text{Pe}}}. \quad (6.94)$$

Consequently, it scales like  $\text{Pe}^{-1}$  for  $\text{Pe} \ll 1$  and like  $\text{Pe}^{-1/2}$  for  $\text{Pe} \gg 1$ .

As one can notice in Fig. 6.10, panels (d–f), the dependence of the concentration profiles on the permeability contrast is weak. In the limit of large permeability contrast

$$\lim_{\kappa \rightarrow \infty} \hat{c} = \text{erf} \left( \sqrt{\frac{1}{2}\text{Pe}(\chi - 1)} \right) = \text{erf} \left( \sqrt{\frac{1}{2}\text{Pe}(\sqrt{\hat{r}} - \hat{x} - 1)} \right) \quad (6.95)$$

outside the root.

### Propagation velocity

Lastly, one can derive the propagation velocity of the root,

$$\hat{U} = - \frac{\hat{c}'(\chi)}{F(\hat{c}(\chi))\partial_{\chi}\hat{x}} \Big|_{\chi=1} = \sqrt{\frac{2}{\pi\text{Pe}}} \frac{\exp\left(-\frac{1}{2\kappa^2}\text{Pe}\right)}{1 - \text{erf}\left(\frac{1}{\kappa}\sqrt{\frac{1}{2}\text{Pe}}\right)}. \quad (6.96)$$

The limiting case of small Péclet numbers is

$$\hat{U} \approx \sqrt{\frac{2}{\pi\text{Pe}}}. \quad (6.97)$$

Interestingly, the same result can be obtained in the limit of large permeability contrast,

$$\lim_{\kappa \rightarrow \infty} \hat{U} = \sqrt{\frac{2}{\pi\text{Pe}}}. \quad (6.98)$$

The velocity scale in our model is  $\gamma u_0$ . Recalling the definition of the Peclét number, we find that the dimensional propagation velocity is equal to

$$\lim_{\kappa \rightarrow \infty} U = \gamma \sqrt{\frac{2D(\varphi_1)u_0}{\pi\rho}}, \quad (6.99)$$

i.e. it is inversely proportional to the square root of the root tip radius of curvature. As one can notice,  $U$  is also an increasing function of both Darcy velocity magnitude  $u_0$  and the dispersion coefficient  $D$ . Increasing the former causes a larger total solvent flux into the system, while the latter is responsible for the transfer of the reactant to the boundary of the root.

The high-Pe limit is a bit more subtle. If  $\text{Pe}$  is significantly larger than  $\kappa^2$ , then the limit of high  $\text{Pe}/\kappa^2$  can be taken for (6.96), yielding

$$\lim_{\text{Pe}/\kappa^2 \rightarrow \infty} \hat{U} = \frac{1}{\kappa}, \quad (6.100)$$

or, in the dimensional variables,

$$\lim_{\text{Pe}/\kappa^2 \rightarrow \infty} U = \frac{\gamma u_0}{\kappa}, \quad (6.101)$$

which is in full analogy with the high-Pe limit for the fingers. The Darcy velocity inside the root is equal to  $u_0/\kappa$ , and multiplying this value by the acid capacity number  $\gamma$ , one obtains the root propagation velocity in the advection-dominant regime.

<sup>4</sup>The tip of the root in our coordinate system is located at  $(\hat{x}, \hat{y}) = (-1/2, 0)$ . Therefore, by denoting the outer boundary of the boundary layer by  $\hat{x}_c$  ( $\chi_c$ ), one can switch from  $\Delta\chi = \chi_c - 1$  to  $\Delta\hat{x}$  in the following way:

$$\Delta\hat{x} = -\frac{1}{2} - \hat{x}_c = -\frac{1}{2} + \frac{1}{2}\chi_c^2 = \frac{1}{2}(\chi_c^2 - 1) = \frac{1}{2}((1 + \Delta\chi)^2 - 1) = \frac{1}{2}(\Delta\chi)^2 + \Delta\chi. \quad (6.93)$$

## 6.2.2 Three-dimensional stationary roots

Similarly as the dissolution fingers, two-dimensional stationary roots have their three-dimensional axisymmetric counterparts. In this section we will derive their characteristics. After assuming the Ivantsov's ansatz, the dynamics of the system outside the root is given by Eqs. (6.51). Then switching to the cylindrical coordinate system,  $(\hat{x}, \hat{y}, \hat{z}) \rightarrow (\hat{r}, \phi, \hat{z})$ , results in Eqs. (6.52). Demanding that  $\hat{c} = \hat{c}(\chi)$  after the conformal transformation  $(\hat{z}, \hat{r}) \rightarrow (\chi, \psi)$  yields the result that the transformation should be a parabolic one. Selecting the negative curvature of the boundary of the root and omitting unimportant parameters of the mapping function results in the following map,

$$\hat{z} = -\frac{1}{2}(\chi^2 - \psi^2) \quad (6.102a)$$

$$\hat{r} = -\chi\psi. \quad (6.102b)$$

As before, it is assumed that the boundary of the root coincides with the  $\chi = 1$  paraboloid.

### Pressure field

After the mapping, the advection-diffusion equation reads

$$\kappa\text{Pe} \frac{\partial \hat{p}}{\partial \chi} \hat{c}'(\chi) + \hat{c}''(\chi) + \frac{1}{\chi} \hat{c}'(\chi) = 0. \quad (6.103)$$

Its form suggests that  $\partial_\chi \hat{p}$  is a function of  $\chi$  only and thus the pressure field  $\hat{p}$  outside the root is separable into

$$\hat{p}(\chi, \psi) = X(\chi) + Y(\psi). \quad (6.104)$$

The Laplace equation for the pressure in the dissolved domain transforms into

$$\frac{\partial^2 \hat{p}}{\partial \chi^2} + \frac{\partial^2 \hat{p}}{\partial \psi^2} + \frac{1}{\chi} \frac{\partial \hat{p}}{\partial \chi} + \frac{1}{\psi} \frac{\partial \hat{p}}{\partial \psi} = 0, \quad \chi > 1. \quad (6.105)$$

Inserting the form (6.104) into Eq. (6.105) yields the general solution of the Laplace equation for the pressure outside the root,

$$\hat{p}(\chi, \psi) = \frac{1}{2}C_0(\chi^2 - \psi^2) + C_1 \ln \chi + C_2 \ln \psi + C_3, \quad \chi > 1. \quad (6.106)$$

The constants  $C_0, C_1, C_2, C_3$  are to be determined from the boundary and the continuity conditions. The far-upstream boundary condition,

$$\lim_{\chi \rightarrow \infty} \kappa \hat{\nabla} \hat{p} = -\hat{\nabla} \hat{z}, \quad (6.107)$$

yields  $C_0 = 1/\kappa$ . Next, we note that the solution of the Laplace equation for the pressure field outside the root should be of the same functional form as the one inside,

$$\hat{p}(\chi, \psi) = \frac{1}{2}C'_0(\chi^2 - \psi^2) + C_4 \ln \chi + C_5 \ln \psi, \quad 0 \leq \chi < 1 \quad (6.108)$$

(the constant term has been skipped). Setting  $C_4 = C_5 = 0$  is necessary to avoid singularities at  $\chi = 0$  or  $\psi = 0$ . The continuity of the pressure and the normal component of the Darcy velocity at the boundary of the root yields  $C'_0 = 1/\kappa$ ,  $C_1 = (1 - \kappa)/\kappa^2$ , and  $C_2 = C_3 = 0$ .

Eventually, the pressure field in the whole space (inside and outside the root) is

$$\hat{p}(\chi, \psi) = \begin{cases} \frac{1}{2\kappa}(\chi^2 - \psi^2), & 0 \leq \chi \leq 1, \\ \frac{1}{2\kappa}(\chi^2 - \psi^2) - \frac{\kappa - 1}{\kappa^2} \ln \chi, & \chi \geq 1, \end{cases} \quad (6.109)$$

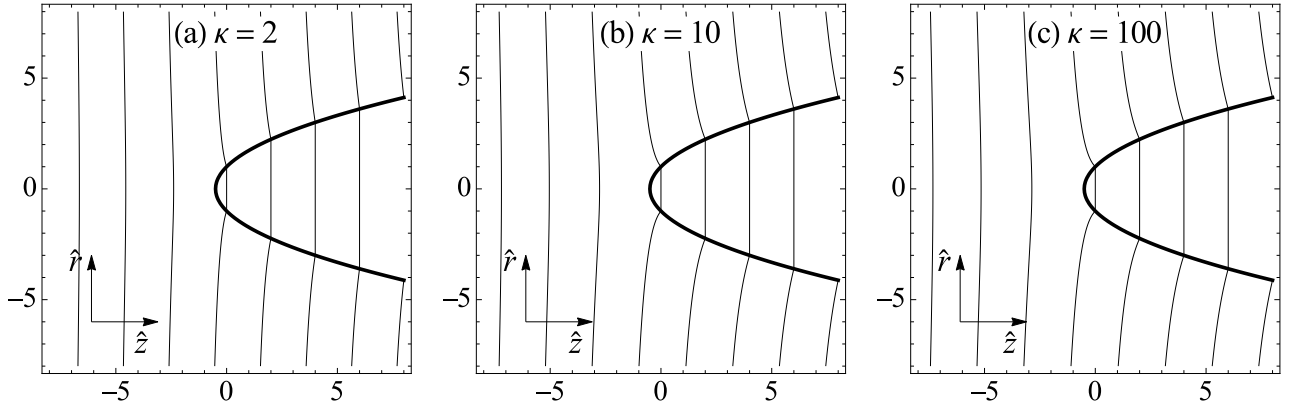


Figure 6.11: Pressure field inside and outside of the three-dimensional stationary root (marked by the thick parabola), for different values of permeability contrasts  $\kappa$ , (a)  $\kappa = 2$ , (b)  $\kappa = 10$ , and (c)  $\kappa = 100$ . The (dimensionless) pressure drop between the neighbouring isobars is (a) 1, (b) 0.2, and (c) 0.02.

or, using Cartesian coordinates,

$$\hat{p}(\hat{z}, \hat{x}) = \begin{cases} -\kappa^{-1}\hat{z}, & 0 \leq \sqrt{\hat{z}^2 + \hat{r}^2} - \hat{z} \leq 1, \\ -\kappa^{-1}\hat{z} - \frac{\kappa - 1}{2\kappa^2} \ln(\sqrt{\hat{z}^2 + \hat{r}^2} - \hat{z}), & \sqrt{\hat{z}^2 + \hat{r}^2} - \hat{z} \geq 1. \end{cases} \quad (6.110)$$

The solution is illustrated in Fig. 6.11. Again we note that the flow field inside the root is uniform (the isobars are parallel to each other). The higher the permeability contrast, the less fluid penetrates the root (the more orthogonal are the isobars to the outer boundary of the root).

### Solvent concentration field

Based on the pressure field (6.109) one can solve Eq. (6.103) and find the concentration field outside the root. The solution, satisfying the far-field and the matching conditions,

$$\hat{c}(\chi \rightarrow \infty) = 1, \quad \hat{c}(\chi = 1) = 0, \quad (6.111)$$

can be written either in terms of the incomplete Gamma function  $\Gamma(a, z) = \int_z^\infty dt e^{-t} t^{a-1}$ , or the exponential integral function  $E_n(z) = \int_1^\infty dt e^{-tz} t^{-n}$ ,

$$\hat{c}(\chi) = 1 - \frac{\Gamma\left(\frac{\text{Pe}(\kappa-1)}{2\kappa}, \frac{\text{Pe}\chi^2}{2}\right)}{\Gamma\left(\frac{\text{Pe}(\kappa-1)}{2\kappa}, \frac{\text{Pe}}{2}\right)} = 1 - \frac{\chi^{\frac{(\kappa-1)\text{Pe}}{\kappa}} E_{1-\frac{\text{Pe}(\kappa-1)}{2\kappa}}\left(\frac{\text{Pe}\chi^2}{2}\right)}{E_{1-\frac{\text{Pe}(\kappa-1)}{2\kappa}}\left(\frac{\text{Pe}}{2}\right)}, \quad \chi > 1. \quad (6.112)$$

The concentration field is shown in Fig. 6.12. For small Pe it is diffusion which dominates in the vicinity of the root tip, and the concentration gradients are relatively small. In the opposite case of large Pe, the solvent concentration is almost uniform ( $\hat{c} \approx 1$ ), except for a thin boundary layer near the boundary of the root, which is characterized by a steep decrease of the concentration.

Similarly as in the two-dimensional case, the dependence of the concentration profiles on the permeability contrast is rather weak (see Fig. 6.12, panels (d-f)), and the limit of large

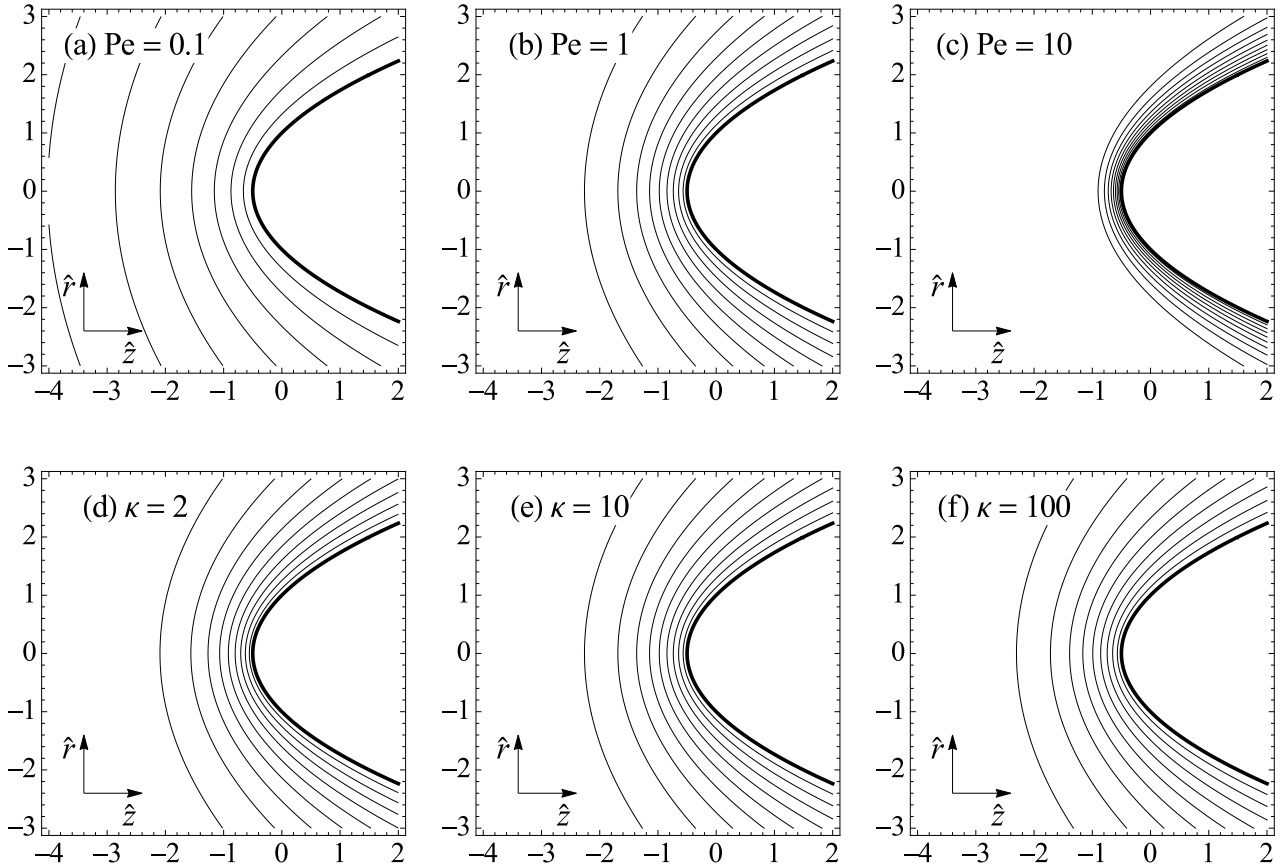


Figure 6.12: Reactant concentration field  $\hat{c}$  outside the two-dimensional stationary root (marked by the thick parabola). Top row:  $\kappa = 10$  and (a)  $Pe = 0.1$ , (b)  $Pe = 1$ , (c)  $Pe = 10$ . Bottom row:  $Pe = 1$  and (d)  $\kappa = 2$ , (e)  $\kappa = 10$ , (f)  $\kappa = 100$ . The (dimensionless) concentration drop between the neighbouring isolines of  $\hat{c}$  (thin parabolas) is set to 0.1. The boundary of the finger is also an isoline of the concentration (for  $\hat{c} = 0$ ).

permeability contrast is finite,

$$\begin{aligned}\lim_{\kappa \rightarrow \infty} \hat{c} &= 1 - \frac{\Gamma\left(\frac{\text{Pe}}{2}, \frac{\text{Pe}\chi^2}{2}\right)}{\Gamma\left(\frac{\text{Pe}}{2}, \frac{\text{Pe}}{2}\right)} = 1 - \frac{\chi^{\text{Pe}} E_{1-\text{Pe}/2}\left(\frac{\text{Pe}\chi^2}{2}\right)}{E_{1-\text{Pe}/2}\left(\frac{\text{Pe}}{2}\right)} \\ &= 1 - \frac{\Gamma\left(\frac{\text{Pe}}{2}, \frac{\text{Pe}}{2}(\sqrt{\hat{z}^2 + \hat{r}^2} - \hat{z})\right)}{\Gamma\left(\frac{\text{Pe}}{2}, \frac{\text{Pe}}{2}\right)} = 1 - \frac{\chi^{\text{Pe}} E_{1-\text{Pe}/2}\left(\frac{\text{Pe}}{2}(\sqrt{\hat{z}^2 + \hat{r}^2} - \hat{z})\right)}{E_{1-\text{Pe}/2}\left(\frac{\text{Pe}}{2}\right)}\end{aligned}\quad (6.113)$$

outside the root.

### Propagation velocity

Finally, the finger propagation velocity, derived analogously to the previous cases, is given by

$$\hat{U} = -\frac{\hat{c}'(\chi)}{F(\hat{c}(\chi))\partial_\chi \hat{z}} \Big|_{\chi=1} = \frac{e^{-\text{Pe}/2} \left(\frac{\text{Pe}}{2}\right)^{\frac{(\kappa-1)\text{Pe}}{2\kappa}-1}}{\Gamma\left(\frac{\text{Pe}(\kappa-1)}{2\kappa}, \frac{\text{Pe}}{2}\right)} = \frac{2e^{-\text{Pe}/2}}{\text{Pe} E_{1-\frac{\text{Pe}(\kappa-1)}{2\kappa}}\left(\frac{\text{Pe}}{2}\right)}.\quad (6.114)$$

In the diffusion-dominant regime ( $\text{Pe} \ll 1$ ), Eq. (6.114) simplifies to<sup>5</sup>

$$\hat{U} \approx -\frac{2}{\text{Pe}(\ln \text{Pe} + \gamma_E - \ln 2)},\quad (6.116)$$

while the advection-dominant case ( $\text{Pe} \gg 1$ ) is

$$\lim_{\text{Pe} \rightarrow \infty} \hat{U} = \kappa^{-1}.\quad (6.117)$$

The limiting case of finite Pe and large permeability contrast is

$$\lim_{\kappa \rightarrow \infty} \hat{U} = \frac{e^{-\text{Pe}/2} \left(\frac{\text{Pe}}{2}\right)^{\frac{\text{Pe}}{2}-1}}{\Gamma\left(\frac{\text{Pe}}{2}, \frac{\text{Pe}}{2}\right)} = \frac{2e^{-\text{Pe}/2}}{\text{Pe} E_{1-\text{Pe}/2}\left(\frac{\text{Pe}}{2}\right)}.\quad (6.118)$$

The asymptotic ( $x \rightarrow \infty$ ) behaviour of the incomplete Gamma function is  $\Gamma(x, x) \approx \Gamma(x)/2 \approx \sqrt{\pi x/2} x^{x-1} e^{-x}$ . As a result, for  $\kappa \rightarrow \infty$  and large Pe the propagation velocity follows

$$\lim_{\kappa \rightarrow \infty} \hat{U} \approx \sqrt{\frac{4}{\pi \text{Pe}}}\quad (6.119)$$

Equations (6.117) and (6.119) are analogous to their two-dimensional counterparts, but the asymptotic behaviour in the small-Pe case, Eq. (6.116), is markedly different. A probable explanation of this discrepancy is the sensitivity of the diffusion (which is a dominant transport mechanism for  $\text{Pe} \ll 1$ ) to the dimensionality change.

<sup>5</sup> Expansion of the denominator of (6.114) gives

$$\Gamma\left(\frac{\text{Pe}(\kappa-1)}{2\kappa}, \frac{\text{Pe}}{2}\right) = -\gamma_E + \ln 2 - \ln \text{Pe} + O(\text{Pe} \ln^2 \text{Pe}).\quad (6.115)$$

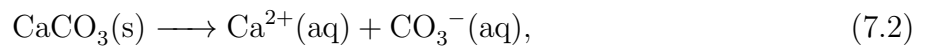
# Chapter 7

## Dynamics of dissolution-precipitation fronts

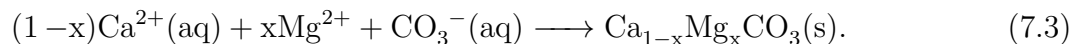
In the theoretical studies on stability and evolution of reaction fronts, most effort has been put so far on analyzing the simplest systems, with a single mineral being dissolved. Natural systems are usually, however, more complicated, and multiple chemical reactions typically occur simultaneously. In principle, dissolution of one mineral is often accompanied by precipitation of another. For instance, dolomitization is such a replacement process. Calcite (calcium carbonate), exposed to Mg-rich fluids, transforms into dolomite (calcium magnesium carbonate) [76]. The overall reaction is



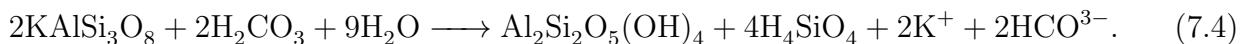
with  $0 < x < 1$ , but the process itself is more complicated than Eq. (7.1) might suggest. It consists of (at least) two subprocesses: dissolution of calcite,



and precipitation of dolomite,



A similar alteration process is kaolinization, when alkali feldspar in the presence of a slightly acidic solution is replaced by kaolinite (a clay mineral),



Replacement is observed on the geological scales, but it can be also reproduced in laboratory [9]. However, due to the length scale difference between these two cases, the ion transport mechanisms are different. At large scales ( $> 1$  m) advection dominates, whereas at small scales ( $< 1$  cm) the transport is mostly diffusive.

In this chapter we will formulate a simple model of an infiltration-driven replacement system and study its stability.

### 7.1 Model

In our model system, two reactions occur simultaneously. In course of dissolution of the primary mineral ( $M_P$ ) by the incoming reactant ( $X$ ), an aqueous product  $A_S$  is produced,



(where  $n_{X,P}$  denote stoichiometric coefficients). The product ion ( $A_S$ ) reacts with some species  $Y$ , present in the aqueous or mineral phase, and precipitates, forming the secondary mineral  $M_S$ ,



where  $n_S$  stands for the stoichiometric coefficient. We assume that the amount of  $Y$  is sufficiently high, so that its concentration does not change much in the process. Consequently, the reaction rates do not depend on the concentration of  $Y$ , which is thus not tracked.

The reactive transport model has been introduced earlier in this thesis, in Chapter 2. Here, we will quickly recall it in the context of the dissolution-precipitation system. The rock is infiltrated by incompressible Darcy flow,

$$\mathbf{u} = -\frac{K(\varphi)}{\mu} \nabla p, \quad \nabla \cdot \mathbf{u} = 0, \quad (7.7a)$$

which is uniform far downstream,

$$\lim_{x \rightarrow \infty} \mathbf{u} = u_0 \mathbf{e}_x. \quad (7.7b)$$

Since the Darcy velocity should be finite, pressure should be a continuous field, despite possible discontinuities in the porosity and permeability fields.

The aqueous species  $X$  and  $A_S$  are transported in the flow by advection and dispersion. Their concentrations change due to chemical activity as well. Consequently, the spatial variability of both concentrations is governed by the advection-dispersion-reaction equations,

$$\nabla \cdot (c_X \mathbf{u}) - \nabla \cdot (D_H(\varphi) \nabla c_X) = -r_{\text{diss}}, \quad (7.7c)$$

$$\nabla \cdot (c_S \mathbf{u}) - \nabla \cdot (D_S(\varphi) \nabla c_S) = n_P r_{\text{diss}} - r_{\text{prec}}. \quad (7.7d)$$

In the above,  $r_{\text{diss}}$  and  $r_{\text{prec}}$  denote rates of reactions (7.5) and (7.6), respectively. Far upstream the concentration of the solvent  $X$  is fixed, while the concentration of the coupling ion  $A_S$  is zero. Far downstream, these concentrations do not change — the fluid is in chemical equilibrium with the infiltrated rock [13],

$$c_X|_{x \rightarrow -\infty} = c_X^{\text{in}}, \quad \partial_x c_X|_{x \rightarrow \infty} = 0, \quad (7.7e)$$

$$c_S|_{x \rightarrow -\infty} = 0, \quad \partial_x c_S|_{x \rightarrow \infty} = 0. \quad (7.7f)$$

For simplicity, we shall assume the equality of the dispersion coefficients and disregard their variability with porosity, setting

$$D_S(\varphi) = D_H(\varphi) = D = \text{const}. \quad (7.7g)$$

This simplification is only a quantitative one and should not change the system dynamics significantly.

The specific volumes of the primary and secondary minerals evolve due to chemical activity. The volume fraction of the primary mineral decreases, while the volume fraction of the secondary mineral increases,

$$\partial_t v_P = -n_X \nu_P r_{\text{diss}}, \quad (7.7h)$$

$$\partial_t v_S = n_S \nu_S r_{\text{prec}}. \quad (7.7i)$$

In the above,  $\nu_{P,S}$  denote the molar volumes of the primary and the secondary mineral. Initially, the primary mineral occupies the downstream part of the system, while the secondary mineral is absent,

$$v_P|_{t \rightarrow -\infty} = v_P^{\text{max}} \Theta(x), \quad (7.7j)$$

$$v_S|_{t \rightarrow -\infty} = 0, \quad (7.7k)$$

where  $\Theta(x)$  denotes the Heaviside step function. Since we do not assume presence of any other mineral phases in the system, the specific molar volumes and porosity should sum up to unity,

$$v_P + v_S + \varphi = 1. \quad (7.7l)$$

Lastly, the reaction kinetics is modeled as first-order,

$$r_{diss} = \alpha_{diss} c_X \Theta(v_P), \quad (7.7m)$$

$$r_{prec} = \alpha_{prec} c_S, \quad (7.7n)$$

where  $\alpha_{diss,prec}$  are kinetic constants. In fact, both dissolution and precipitation are surface reactions and the fact that the reaction rates are proportional to the specific surface area should be taken into account in (7.7m–7.7n). For simplicity, we assume that the effective reactive surface is constant, and its value is incorporated into the reaction constants  $\alpha_{diss,prec}$ . As an obvious exception, the reactive surface for dissolution is set to zero in the case of absence of the primary mineral, which is modeled as the multiplication of the dissolution rate by the Heaviside step function  $\Theta$ . Regardless of this discontinuity in the reaction kinetics, both concentrations and their derivatives have to be continuous.

## 7.2 Scaling

Since it is more convenient to deal with dimensionless quantities, we will scale our variables. The scaled, dimensionless variables will be denoted by hats (e.g.  $\hat{c}_S$ ). As regards the Darcy velocity and the concentrations, natural scaling comes from the boundary conditions,

$$\hat{\mathbf{u}} = \mathbf{u}/u_0, \quad (7.8)$$

$$\hat{c}_X = c_X/c_X^{in}, \quad (7.9)$$

$$\hat{c}_S = c_S/c_X^{in}. \quad (7.10)$$

As the length and time scales we choose

$$L = \frac{u_0}{\alpha_{prec}}, \quad T = \frac{v_P^{max}}{n_X \nu_P c_X^{in} \alpha_{prec}}. \quad (7.11)$$

The velocity scale is taken to be

$$\frac{L}{T} = \frac{n_X \nu_P c_X^{in} u_0}{v_P^{max}}. \quad (7.12)$$

The specific volumes and the porosity are already dimensionless, but for convenience we scale them as

$$\hat{v}_S = v_S/v_P^{max}, \quad (7.13)$$

$$\hat{v}_P = v_P/v_P^{max}, \quad (7.14)$$

$$\hat{\varphi} = 1 + (\varphi - 1)/v_P^{max}. \quad (7.15)$$

Now the scaled specific volumes vary between zero and one, and the scaled porosity between  $1 - 1/v_P^{max}$  and one. Lastly, we scale the rock permeability and the pressure,

$$\hat{K} = \frac{K(\varphi)}{K(1 - v_P^{max})}, \quad (7.16)$$

$$\hat{p} = \frac{K(1 - v_P^{max})}{u_0 \mu L} p. \quad (7.17)$$

In the scaled variables, the dynamics of the system (7.7) reads

$$\hat{\nabla} \cdot \hat{\mathbf{u}} = 0 \quad (7.18a)$$

$$\hat{\mathbf{u}} = \hat{K}(\hat{\varphi}) \hat{\nabla} \hat{p} \quad (7.18b)$$

$$\hat{\nabla} \cdot (\hat{c}_X \hat{\mathbf{u}}) - H \hat{\nabla}^2 \hat{c}_X = -\Lambda \Theta(\hat{v}_P) \hat{c}_X \quad (7.18c)$$

$$\hat{\nabla} \cdot (\hat{c}_S \hat{\mathbf{u}}) - H \hat{\nabla}^2 \hat{c}_S = n_P \Lambda \Theta(\hat{v}_P) \hat{c}_X - \hat{c}_S \quad (7.18d)$$

$$\partial_{\hat{t}} \hat{v}_P = -\Lambda \Theta(\hat{v}_P) \hat{c}_X \quad (7.18e)$$

$$\partial_{\hat{t}} \hat{v}_S = \frac{n_S \nu_S}{n_X \nu_P} \hat{c}_S \quad (7.18f)$$

$$\hat{\varphi} + \hat{v}_S + \hat{v}_P = 1, \quad (7.18g)$$

where the transport parameter

$$H = \frac{\alpha_{prec} D}{u_0^2} \quad (7.19)$$

is the ratio of the Damköhler and the Péclet numbers associated with the precipitation, and

$$\Lambda = \frac{\alpha_{diss}}{\alpha_{prec}} \quad (7.20)$$

is the ratio of the reaction kinetic constants.

The boundary and initial conditions for the rescaled quantities are

$$\hat{c}_S|_{\hat{x} \rightarrow -\infty} = 0, \quad \hat{c}_S|_{\hat{x} \rightarrow \infty} = 0, \quad (7.21)$$

$$\hat{c}_X|_{\hat{x} \rightarrow -\infty} = 1, \quad \hat{c}_X|_{\hat{x} \rightarrow \infty} = 0, \quad (7.22)$$

$$\hat{\mathbf{u}}|_{\hat{x} \rightarrow \infty} = \hat{e}_x, \quad (7.23)$$

and

$$\hat{v}_P|_{\hat{t} \rightarrow -\infty} = \Theta(\hat{x}), \quad \hat{v}_S|_{\hat{t} \rightarrow -\infty} = 0. \quad (7.24)$$

## 7.3 One-dimensional solutions

Numerical simulations of the one-dimensional version of dynamics (7.18) reveals that after some transient period a dissolution-precipitation front is formed (Fig. 7.1). The front evolves to an invariant form, propagating with a constant velocity. The velocity of such a stationary front  $U$ , as well as the eventual secondary mineral content,  $v_S^{max}$ , can be deduced from mass balance between the incoming and outgoing ions. The reasoning will be presented in Sec. 7.3.1. Next, in Sec. 7.3.2, we will obtain the same results, studying invariants which appear in the system dynamics. Lastly, in Sec. 7.3.3, we derive complete analytical solutions which describe the volume fraction and concentration profiles of the stationary replacement fronts. Here, the values of  $U$  and  $v_S^{max}$  arise as a consequence of continuity conditions.

### 7.3.1 Mass balance

The incoming reactant flux density (in moles of X per unit area and unit time) is  $u_0 c_X^{in}$ , while the outgoing reactant flux density vanishes. The rate of the primary mineral consumption (in moles of  $M_P$  per unit area and unit time) is  $v_P^{max} U / \nu_P$ , where  $U$  is the velocity of the reaction front. Since the dissolution reaction stoichiometry is  $n_X M_P + X \longrightarrow n_P A_S$ , from mass balance we get

$$u_0 c_X^{in} = \frac{v_P^{max} U}{n_X \nu_P}, \quad (7.25)$$

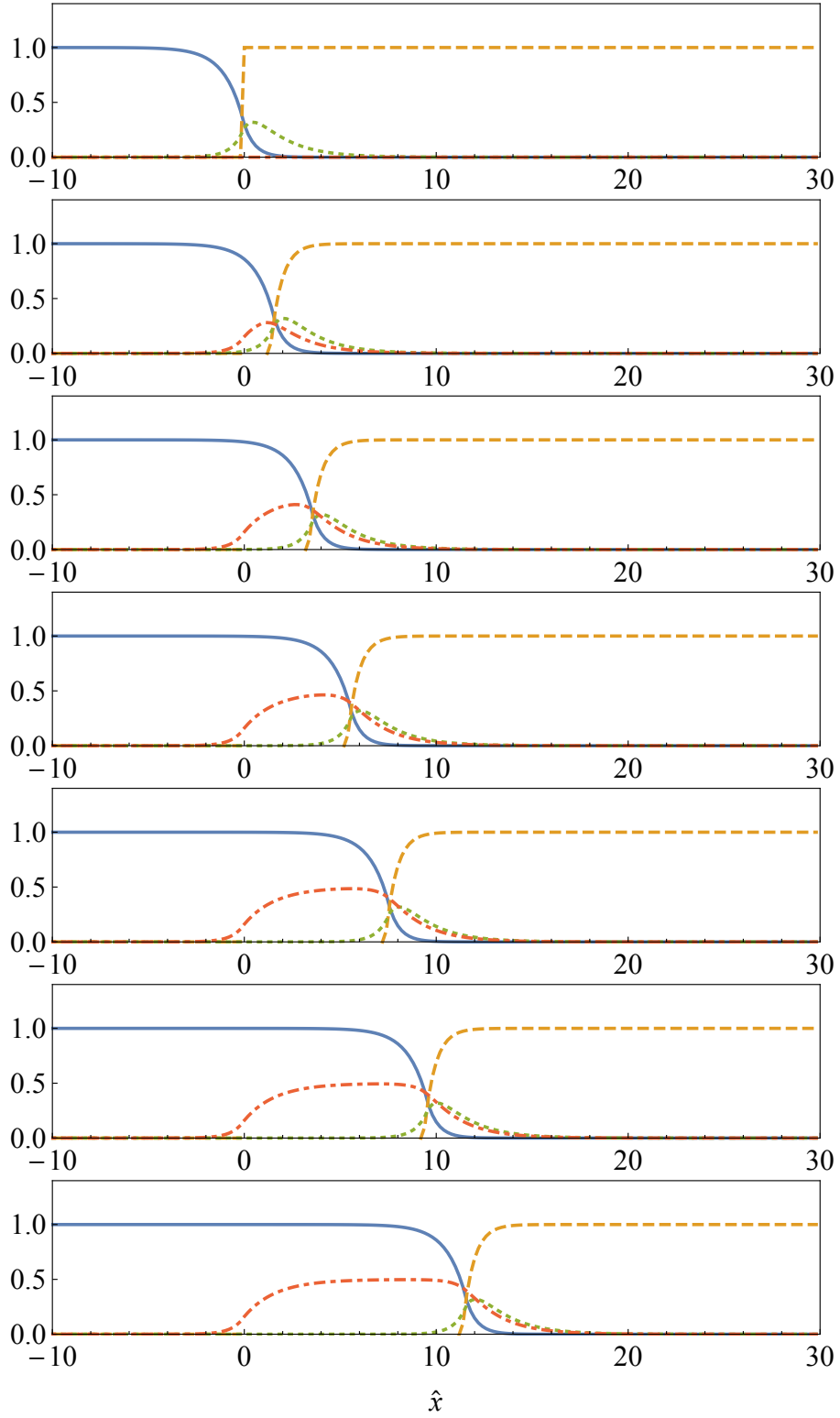
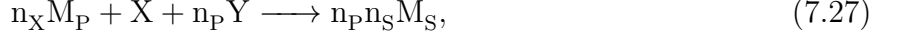


Figure 7.1: Numerical solutions of the one-dimensional version of Eqs. (7.18), for  $\Lambda = 5$ ,  $n_S \nu_S / n_X \nu_P = 0.5$ ,  $H = 1$ , and  $n_P = 1$ . The fields ( $\hat{c}_X$ , blue solid;  $\hat{v}_P$ , yellow dashed;  $\hat{c}_S$ , green dotted; and  $\hat{v}_S$ , red dot-dashed) are plotted in moments  $\hat{t} = 0, 2, 4, 6, 8, 10$ , and  $12$  (panels top to bottom). The dissolution-precipitation front develops and evolves towards a stationary form while translating. Note that the final porosity of the precipitated phase is  $0.5$ .

which yields the front velocity equal to

$$U = \frac{u_0 c_X^{in} n_X \nu_P}{v_P^{max}}. \quad (7.26)$$

As illustrated in Fig. 7.1, the replacement front propagates leaving behind a certain amount of the secondary mineral. Similar mass balance allows us to find the asymptotic ( $t \rightarrow \infty$ ) specific volume of the secondary mineral. After combining chemical reactions (7.5–7.6) into a single one,



it can be noticed that  $n_X$  moles of the primary mineral are replaced with  $n_P n_S$  moles of the secondary mineral. Let us then consider an arbitrary point where initially  $v_P = v_P^{max}$  (e.g. any  $\hat{x} \gg 1$  in Fig. 7.1). Taking the molar volumes into account, the asymptotic (and maximal) specific volume of the secondary mineral at this point is

$$v_S^{max} = v_S(t \rightarrow \infty) = \frac{n_P n_S \nu_S}{n_X \nu_P} v_P^{max}. \quad (7.28)$$

Note that in the above reasoning we neglect any smoothening effects connected with dispersion.

### 7.3.2 Spatial invariants

The same results as those presented in Sec. 7.3.1 can be obtained in a more strict way by studying the one-dimensional version of the system dynamics, either in the dimensional or dimensionless form. The idea of such an analysis was first introduced by Ortoleva et al. [11]. Considering the dimensionless equations 7.18, one gets in 1D

$$\partial_{\hat{x}} \hat{u}_x = 0 \quad (7.29a)$$

$$\hat{u}_x = \hat{K}(\hat{\varphi}) \partial_{\hat{x}} \hat{p} \quad (7.29b)$$

$$\partial_{\hat{x}} (\hat{c}_X \hat{u}_x) - H \partial_{\hat{x}}^2 \hat{c}_X = -\Lambda \Theta(\hat{v}_P) \hat{c}_X \quad (7.29c)$$

$$\partial_{\hat{x}} (\hat{c}_S \hat{u}_x) - H \partial_{\hat{x}}^2 \hat{c}_S = n_P \Lambda \Theta(\hat{v}_P) \hat{c}_X - \hat{c}_S \quad (7.29d)$$

$$\partial_{\hat{t}} \hat{v}_P = -\Lambda \Theta(\hat{v}_P) \hat{c}_X \quad (7.29e)$$

$$\partial_{\hat{t}} \hat{v}_S = \frac{n_S \nu_S}{n_X \nu_P} \hat{c}_S \quad (7.29f)$$

$$-\hat{\varphi} = \hat{v}_S + \hat{v}_P, \quad (7.29g)$$

with the boundary and initial conditions

$$\hat{c}_S|_{\hat{x} \rightarrow -\infty} = 0, \quad \partial_{\hat{x}} \hat{c}_S|_{\hat{x} \rightarrow \infty} = 0, \quad (7.30a)$$

$$\hat{c}_X|_{\hat{x} \rightarrow -\infty} = 1, \quad \partial_{\hat{x}} \hat{c}_X|_{\hat{x} \rightarrow \infty} = 0, \quad (7.30b)$$

$$\hat{u}_x|_{\hat{x} \rightarrow \infty} = 1, \quad (7.30c)$$

$$\hat{v}_P|_{\hat{t} \rightarrow -\infty} = \Theta(\hat{x}), \quad \hat{v}_S|_{\hat{t} \rightarrow -\infty} = 0. \quad (7.30d)$$

The incompressibility of the Darcy velocity, along with the accompanying far-downstream boundary condition immediately yields

$$\hat{u}_x = 1. \quad (7.31)$$

The pressure field adapts to the varying permeability to assert (7.31). Now let us switch to the coordinate system translating with the reaction front, i.e. apply the coordinate transformation  $(\hat{x}, \hat{t}) \rightarrow (\xi, \tau)$ ,

$$\xi = \hat{x} - \hat{U} \hat{t}, \quad \tau = \hat{t}, \quad (7.32)$$

to Eqs. (7.29). Without any loss of generality we can set  $\xi = 0$  at the rightmost place where the primary mineral is absent. In the above,  $\hat{U}$  denotes the dimensionless reaction front velocity, which is yet to be determined. In the moving coordinates, the one-dimensional ion transport and rock composition evolution equations are

$$\partial_\xi \hat{c}_X - H \partial_\xi^2 \hat{c}_X = -\Lambda \Theta(\hat{v}_P) \hat{c}_X \quad (7.33a)$$

$$\partial_\xi \hat{c}_S - H \partial_\xi^2 \hat{c}_S = n_P \Lambda \Theta(\hat{v}_P) \hat{c}_X - \hat{c}_S \quad (7.33b)$$

$$(\partial_\tau - \hat{U} \partial_\xi) \hat{v}_P = -\Lambda \Theta(\hat{v}_P) \hat{c}_X \quad (7.33c)$$

$$(\partial_\tau - \hat{U} \partial_\xi) \hat{v}_S = \frac{n_S \nu_S}{n_X \nu_P} \hat{c}_S. \quad (7.33d)$$

Now we assume that the stationary state has been achieved, which formally means taking the long-time limit,  $\tau \rightarrow \infty$ . In the reference frame moving with the front, its morphology is time independent. Two equations can be composed from Eqs. (7.33),

$$\partial_\xi \hat{c}_X - H \partial_\xi^2 \hat{c}_X = -\hat{U} \partial_\xi \hat{v}_P, \quad (7.34a)$$

$$\partial_\xi \hat{c}_S - H \partial_\xi^2 \hat{c}_S = -n_P \hat{U} \partial_\xi \hat{v}_P + \frac{n_X \nu_P}{n_S \nu_S} \hat{U} \partial_\xi \hat{v}_S. \quad (7.34b)$$

Now one can notice that the above identities yield two functions, which are independent of the  $\xi$  variable,

$$\partial_\xi \left( \hat{c}_X - H \partial_\xi \hat{c}_X + \hat{U} \hat{v}_P \right) = 0, \quad (7.35a)$$

$$\partial_\xi \left( \hat{c}_S - H \partial_\xi \hat{c}_S + n_P \hat{U} \hat{v}_P - \frac{n_X \nu_P}{n_S \nu_S} \hat{U} \hat{v}_S \right) = 0, \quad (7.35b)$$

which can be evaluated at  $\xi \rightarrow \pm\infty$  and compared,

$$\lim_{\xi \rightarrow -\infty} \left( \hat{c}_X - H \partial_\xi \hat{c}_X + \hat{U} \hat{v}_P \right) = \lim_{\xi \rightarrow \infty} \left( \hat{c}_X - H \partial_\xi \hat{c}_X + \hat{U} \hat{v}_P \right), \quad (7.36a)$$

$$\lim_{\xi \rightarrow -\infty} \left( \hat{c}_S - H \partial_\xi \hat{c}_S + n_P \hat{U} \hat{v}_P - \frac{n_X \nu_P}{n_S \nu_S} \hat{U} \hat{v}_S \right) = \lim_{\xi \rightarrow \infty} \left( \hat{c}_S - H \partial_\xi \hat{c}_S + n_P \hat{U} \hat{v}_P - \frac{n_X \nu_P}{n_S \nu_S} \hat{U} \hat{v}_S \right). \quad (7.36b)$$

In an infinite system diffusive fluxes should vanish both far upstream and far downstream. The boundary conditions for the concentrations, Eqs. (7.30a–b), transform in the moving reference frame into

$$\hat{c}_X|_{\xi \rightarrow -\infty} = 0, \quad \partial_\xi \hat{c}_X|_{\xi \rightarrow \infty} = 0, \quad (7.37a)$$

$$\hat{c}_S|_{\xi \rightarrow -\infty} = 1, \quad \partial_\xi \hat{c}_S|_{\xi \rightarrow \infty} = 0. \quad (7.37b)$$

Additionally, the fluid far downstream should be in chemical equilibrium with the infiltrated rock, which in the case of our chemical kinetics is asserted for

$$\hat{c}_X|_{\xi \rightarrow \infty} = 0, \quad \hat{c}_S|_{\xi \rightarrow \infty} = 0. \quad (7.37c)$$

Evaluation of the specific volumes at  $\xi \rightarrow \pm\infty$  is a bit more tricky. The initial far-downstream ( $\hat{x} \rightarrow \infty$ ) value of the primary mineral volume fraction should be equal to the asymptotic ( $\tau \rightarrow \infty$ ) far-downstream ( $\xi \rightarrow \infty$ ) value, so the initial conditions for the specific volumes, Eqs. (7.30d), can be transformed into far-downstream boundary conditions in the  $(\xi, \tau)$  coordinates as follows,

$$\hat{v}_P|_{\xi \rightarrow \infty} = 1, \quad \hat{v}_S|_{\xi \rightarrow \infty} = 0. \quad (7.37d)$$

Upstream of the stationary replacement front all the primary mineral has been replaced by a certain amount of the secondary mineral, so

$$\hat{v}_P|_{\xi \rightarrow -\infty} = 0, \quad \hat{v}_S|_{\xi \rightarrow -\infty} = \varrho^{-1}, \quad (7.37e)$$

where the amount of the precipitate  $\varrho^{-1}$ , as not given a priori in our model, is to be determined. Eventually, evaluation of (7.36) yields the reaction front velocity  $\hat{U}$ , as well as the value of  $\varrho$ ,

$$\hat{U} = 1, \quad \varrho = \frac{n_X \nu_P}{n_S n_P \nu_S}. \quad (7.38)$$

Taking into account the scalings, the result is fully analogous to Eqs. (7.26) and (7.28). Note that neither here, nor in Sec. 7.3.1, we have not assumed any specific form of the reaction kinetics. Only the concentrations far upstream and far downstream are relevant, the latter corresponding to chemical equilibrium. Also, a more general dispersion model could have been assumed here as well. It does not influence the results provided that the diffusive fluxes vanish far upstream and far downstream, which is in fact inevitable for infinite systems.

### 7.3.3 One-dimensional profiles

The entire morphology of the asymptotic, stationary front can be found analytically for simple our model. Let us return to Eqs. (7.33) and assume stationarity ( $\partial_\tau = 0$ ). The advection-dispersion-reaction equation for the solvent X has an exponential solution. The integration constants can be found from the transformed boundary conditions (7.37a) and the requirement of continuity of both the concentration and its derivative. After short algebra one recovers

$$\hat{c}_X(\xi) = \begin{cases} \left( \frac{\Gamma_2}{\Lambda} - 1 \right) e^{\xi/H} + 1, & \xi < 0, \\ \frac{\Gamma_2}{\Lambda} e^{-\Gamma_2 \xi}, & \xi > 0, \end{cases} \quad (7.39a)$$

where  $\Gamma_2 = \frac{\sqrt{1 + 4\Lambda H} - 1}{2H}$ . Knowing the functional form of the stationary solvent concentration profile, it is straightforward to integrate Eq. (7.33c) and recover the stationary profile of the primary mineral specific volume. In that way one finds

$$\hat{v}_P(\xi) = \begin{cases} 0, & \xi < 0, \\ 1 - e^{-\Gamma_2 \xi}, & \xi > 0, \end{cases} \quad (7.39b)$$

where we have used the fact that  $\hat{U} = 1$  (Eq. (7.38)) and the integration constant was derived from the boundary condition (7.37d). In a similar manner it is possible to obtain the stationary profiles of the coupling ion concentration, and the secondary mineral specific volume,

$$\hat{c}_S(\xi) = \begin{cases} \frac{n_P \Gamma_2}{\Lambda - 1} \frac{\Gamma_2 - \Gamma_1}{\Gamma_1^* + \Gamma_1} e^{\Gamma_1^* \xi}, & \xi < 0, \\ \frac{n_P \Gamma_2}{\Lambda - 1} \left( \frac{\Gamma_1^* + \Gamma_2}{\Gamma_1 + \Gamma_1^*} e^{-\Gamma_1 \xi} - e^{-\Gamma_2 \xi} \right), & \xi > 0, \end{cases} \quad (7.39c)$$

$$\hat{v}_S(\xi) = \begin{cases} \varrho^{-1} \left( 1 - \frac{1}{\Lambda - 1} \frac{\Gamma_2 \Gamma_2 - \Gamma_1}{\Gamma_1^* \Gamma_1^* + \Gamma_1} e^{\Gamma_1^* \xi} \right), & \xi < 0, \\ \varrho^{-1} \frac{1}{\Lambda - 1} \left( \frac{\Gamma_2 \Gamma_1^* + \Gamma_2}{\Gamma_1 \Gamma_1 + \Gamma_1^*} e^{-\Gamma_1 \xi} - e^{-\Gamma_2 \xi} \right), & \xi > 0, \end{cases} \quad (7.39d)$$

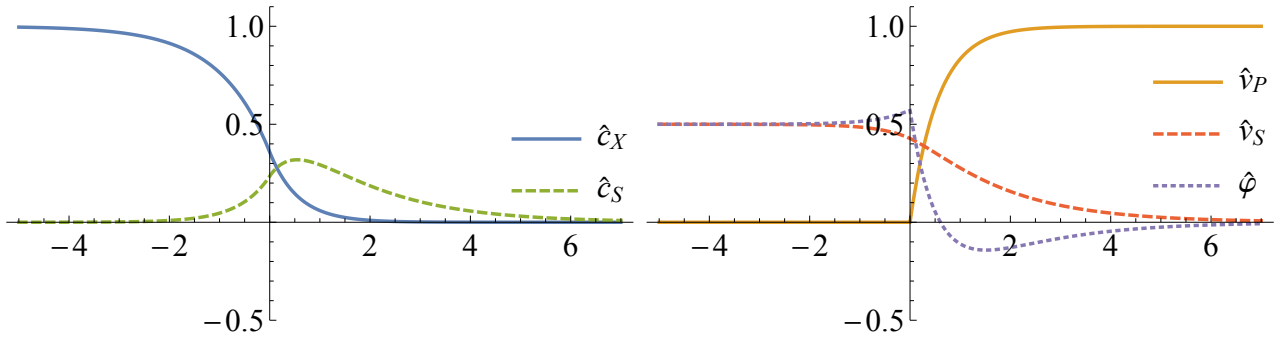


Figure 7.2: One-dimensional stationary solutions, Eqs. (7.39), of the infiltration-driven replacement model, Eqs. (7.18), for  $n_P = 1$ ,  $H = 1$ ,  $\Lambda = 5$ , and  $\varrho = 2$ . Left panel: concentrations. Right panel: specific volumes and porosity.

where  $\Gamma_1 = \frac{\sqrt{1+4H}-1}{2H}$ ,  $\Gamma_1^* = \frac{\sqrt{1+4H}+1}{2H}$ , and the parameter  $\varrho$  is defined in Eq. (7.38). Consequently, the (rescaled) porosity is equal to

$$\hat{\varphi}(\xi) = 1 - \hat{v}_P - \hat{v}_S = \begin{cases} 1 - \varrho^{-1} \left( 1 - \frac{1}{\Lambda - 1} \frac{\Gamma_2 \Gamma_2 - \Gamma_1}{\Gamma_1^* \Gamma_1^* + \Gamma_1} e^{\Gamma_1^* \xi} \right), & \xi < 0, \\ e^{-\Gamma_2 \xi} - \varrho^{-1} \frac{1}{\Lambda - 1} \left( \frac{\Gamma_2 \Gamma_1^* + \Gamma_2}{\Gamma_1 \Gamma_1 + \Gamma_1^*} e^{-\Gamma_1 \xi} - e^{-\Gamma_2 \xi} \right), & \xi > 0. \end{cases} \quad (7.39e)$$

The above stationary solutions are illustrated in Fig. 7.2. The position  $\xi = 0$  was set at the rightmost place free of the primary mineral. The solvent (X) concentration decreases diffusively upstream of the reaction front ( $\xi < 0$ ), and the characteristic (dimensional) width of this diffusive decay is

$$l_X^u = \frac{D}{u_0}. \quad (7.40)$$

Then, at  $\xi > 0$ , the solvent penetrates the primary mineral. The characteristic depth of the penetration,

$$l_X^d = \frac{2D}{\sqrt{u_0^2 + 4D\alpha_{diss}} - u_0}, \quad (7.41)$$

arises from the interplay between the solvent transport and dissolution. The concentration of the secondary ion,  $A_S$ , is increased only in the vicinity of the replacement front, as it is produced during dissolution and almost immediately consumed in course of precipitation. The  $A_S$  ion diffuses upstream, with the characteristic length

$$l_S^u = \frac{2D}{\sqrt{u_0^2 + 4D\alpha_{prec}} + u_0}. \quad (7.42)$$

Downstream it reaches further,

$$l_S^d = \frac{2D}{\sqrt{u_0^2 + 4D\alpha_{prec}} - u_0}, \quad (7.43)$$

as the transport downstream is amplified by advection. The relative magnitudes of these four length scales are functions of two parameters only,  $H$  and  $\Lambda$ . As shown in Fig. 7.3, for both large  $H$  and  $\Lambda$ ,  $l_X^u$  dominates. For  $H < 2$  and  $\Lambda > 1$ ,  $l_S^d$  is the largest length. For small  $\Lambda$ ,  $l_X^d$  dominates. However, the latter case is rather unphysical. Dissolution is usually faster than precipitation,  $\Lambda > 1$ . The expression for the last characteristic length,  $l_S^u$ , is similar to the

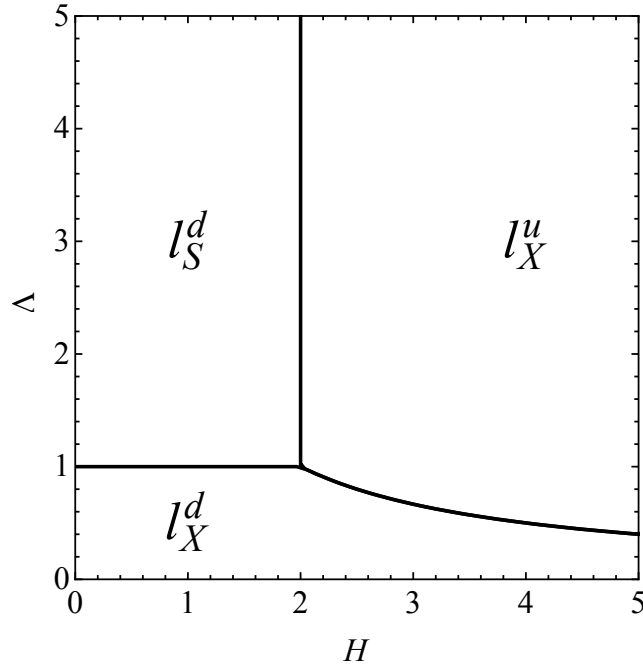


Figure 7.3: A “phase diagram” showing the largest characteristic length as a function of the transport parameter  $H$  and the reaction rate constant ratio  $\Lambda$ . The boundaries between the “phases” are given by relations  $H = 2$ ,  $\Lambda = 1$ , and  $H\Lambda = 2$ .

expression for  $l_S^d$ , except for a sign difference in the denominator. As a consequence,  $l_S^u$  is never the largest length:  $l_S^u < l_S^d$  for any positive Darcy velocity  $u_0$ .

The primary mineral is present only downstream ( $\xi > 0$ ). Its volume fraction increases exponentially with the characteristic length scale  $l_X^d$ . Far downstream it reaches the value  $\hat{v}_P = 1$  (or, returning to the original variables,  $v_P = v_P^{max}$ ). The secondary mineral content decreases from  $\hat{v}_S = \varrho^{-1}$  (or  $v_S = v_P^{max}/\varrho$ ) far upstream to zero far downstream. A notable feature of the stationary replacement front is the nonmonotonicity of the porosity field. Far upstream its value is equal to  $\hat{\varphi} = 1 - \varrho^{-1}$  (or  $\varphi = 1 - v_P^{max}/\varrho$ ). Then, closer to the front, it gradually increases due to a (diffusive) decrease in the secondary mineral content. Just at the dissolution front a sharp decrease of porosity is observed, which is due to relative abundance of both minerals. After reaching a well-defined minimum, porosity increases again as the secondary mineral content goes to zero far downstream.

It can be deduced from Eq. (7.39e) that the minimal value of porosity in a stationary front is

$$\min_{\xi} \hat{\varphi}(\xi) = - \frac{\frac{\Gamma_1^* + \Gamma_2}{\Gamma_1 + \Gamma_1^*} \left( \frac{\Gamma_2}{\Gamma_1} - 1 \right) \left( \left( \frac{\Gamma_1^* + \Gamma_2}{\Gamma_1 + \Gamma_1^*} \right)^{-1} ((\Lambda - 1)\rho + 1) \right)^{(1-\Gamma_2/\Gamma_1)^{-1}}}{(\Lambda - 1)\rho}, \quad (7.44a)$$

and

$$\min_{\xi} \varphi(\xi) = v_P^{max} (\min_{\xi} \hat{\varphi}(\xi) - 1) + 1. \quad (7.44b)$$

Formally Eqs. (7.44) allow for negative minimal porosity, but obviously in nature porosity cannot reach negative values. This imposes a constraint on our results, which are valid only for a part of the parameter space, namely for parameter sets which yield positive values of the porosity minimum,  $\min_{\xi} \varphi$ . A negative value of the expression (7.44b) indicates that a stationary replacement front does not develop for the selected parameters, and our solutions, (7.39), are no longer valid. Fig. 7.4 illustrates the allowed region of the parameter space in two limiting

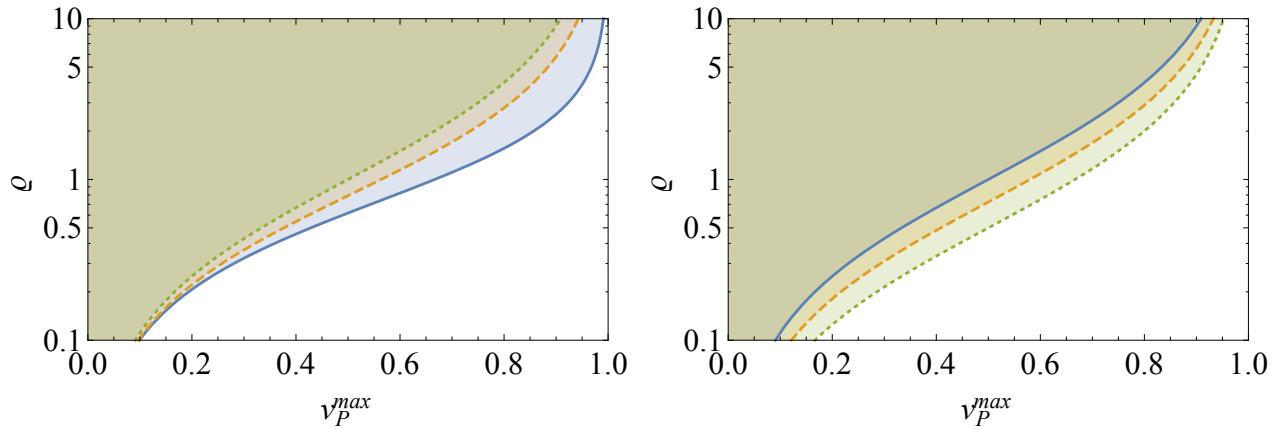


Figure 7.4: Part of the parameter space which yields stationary solutions, i.e. invariantly translating planar replacement fronts. Left: limit of  $H \rightarrow 0$ , and  $\kappa = 2, 10, \infty$  (shaded region above the solid, dashed, and dotted line, respectively). Right: limit of  $\Lambda \rightarrow \infty$ , and  $H = 0, 1, \infty$  (shaded region above solid, dashed, and dotted line, respectively). In general, stationary solutions are possible if  $\varrho$  is sufficiently large and  $v_P^{max}$  — small. Decreasing  $\Lambda$  and increasing  $H$  expands the allowed parameter space.

cases,  $H \rightarrow 0$  (negligible dispersion), and  $\Lambda \rightarrow \infty$  (dissolution much faster than precipitation). Should one wish to study the regime outside this region, a small modification of our model is necessary: the precipitation rate should be modified by an appropriate function of porosity, which would account for the reaction slowdown in case of lack of free pore space. In order to assure that the fluid can percolate through the rock, porosity cannot drop exactly to zero, but only to some minimal porosity,  $\varphi_{min}$ , which can be treated as an additional parameter in the model. The simplest extension of our model, which would prevent the system from complete clogging, involves the additional step function in the precipitation rate (7.7n),

$$r_{prec} = \alpha_{prec} c_S \Theta(\varphi - \varphi_{min}). \quad (7.45)$$

In fact, the introduction of such residual porosity, which prevents the flow paths from being completely clogged, can be justified by the observation that precipitation in small pores is significantly slower than in large pores. Therefore only a fraction of porosity is eliminated in course of precipitation [77]. Moreover, reaction-generated stresses can keep a part of the pore network open and even induce microcracking in the rock matrix.

## 7.4 Stability of stationary replacement fronts

Here, we pose the problem of stability of the one-dimensional solutions with respect to perpendicular perturbations of the front. The method will be similar as presented in Chapter 3, i.e. linear stability analysis (LSA) of the stationary solutions. Now, however, due to a larger number of components, the problem is more complicated. Also, now there are more parameters which might possibly control the behaviour of the system. In order to deal with this issue, in our study we limit ourselves to two special cases, either of negligible dispersion (Sec. 7.4.2), or quick dissolution (with respect to precipitation; Sec. 7.4.3). We begin, however, with general considerations.

### 7.4.1 Dynamics of the perturbations

The linear stability analysis starts with assuming that the reaction front is perturbed by a small transverse perturbation. Our analysis will be limited to two dimensions. As already noted in

Sec. 3.6, a linear stability analysis in 3D can be reduced to a two-dimensional one. Since the domain which we consider is infinite, an arbitrary perturbation can be decomposed into a sum of harmonic modes, which in the linear approximation evolve independently. It is thus sufficient to consider a single harmonic mode, i.e. the dissolution front is taken to be

$$\zeta(\eta, \tau) = \zeta_0 e^{\hat{\sigma}\tau} \cos(\hat{k}\eta), \quad (7.46)$$

where  $\zeta_0 \ll 1$  is the initial amplitude of the perturbation,  $\hat{\sigma}$  is its growth rate,  $\hat{k}$  is the wavenumber characterizing the perturbation, and  $\eta = y/L$  is the rescaled length in the direction transverse to the dominant flow direction.

Up to the linear order, the perturbation of the front results in analogous (spatially harmonic and temporally exponential) perturbations of all the fields. In the following, perturbations will be denoted by tildes. For instance, the perturbed solvent concentration field is upstream equal to

$$\hat{c}_X(\xi) + \tilde{c}_X(\xi, \eta, \tau) = \left( \frac{\Gamma_2}{\Lambda} - 1 \right) e^{\xi/H} + 1 + f_{c_X}(\xi) e^{\hat{\sigma}\tau} \cos(\hat{k}\eta), \quad (7.47)$$

where the (small) amplitude of the perturbation,  $f_{c_X}(\xi)$ , is yet to be determined. Obviously, the perturbed fields also have to satisfy the general equations of the dynamics, (7.18), which in the translating reference frame read

$$\hat{\nabla} \cdot \hat{\mathbf{u}} = 0 \quad (7.48a)$$

$$\hat{\mathbf{u}} = \hat{K}(\hat{\varphi}) \hat{\nabla} \hat{p} \quad (7.48b)$$

$$\hat{\nabla} \cdot (\hat{c}_X \hat{\mathbf{u}}) - H \hat{\nabla}^2 \hat{c}_X = -\Lambda \Theta(\hat{v}_P) \hat{c}_X \quad (7.48c)$$

$$\hat{\nabla} \cdot (\hat{c}_S \hat{\mathbf{u}}) - H \hat{\nabla}^2 \hat{c}_S = n_P \Lambda \Theta(\hat{v}_P) \hat{c}_X - \hat{c}_S \quad (7.48d)$$

$$(\partial_\tau - \partial_\xi) \hat{v}_P = -\Lambda \Theta(\hat{v}_P) \hat{c}_X \quad (7.48e)$$

$$(\partial_\tau - \partial_\xi) \hat{v}_S = \frac{1}{n_P \varrho} \hat{c}_S \quad (7.48f)$$

$$\hat{\varphi} + \hat{v}_S + \hat{v}_P = 1. \quad (7.48g)$$

Inserting the perturbed fields to Eqs. (7.48) gives

$$\hat{\nabla} \cdot (\hat{\mathbf{u}} + \tilde{\mathbf{u}}) = 0 \quad (7.49a)$$

$$(\hat{\mathbf{u}} + \tilde{\mathbf{u}}) = \hat{K}(\hat{\varphi} + \tilde{\varphi}) \hat{\nabla}(\hat{p} + \tilde{p}) \quad (7.49b)$$

$$\hat{\nabla} \cdot ((\hat{c}_X + \tilde{c}_X)(\hat{\mathbf{u}} + \tilde{\mathbf{u}})) - H \hat{\nabla}^2(\hat{c}_X + \tilde{c}_X) = -\Lambda \Theta(\xi - \zeta)(\hat{c}_X + \tilde{c}_X) \quad (7.49c)$$

$$\hat{\nabla} \cdot ((\hat{c}_S + \tilde{c}_S)(\hat{\mathbf{u}} + \tilde{\mathbf{u}})) - H \hat{\nabla}^2(\hat{c}_S + \tilde{c}_S) = n_P \Lambda \Theta(\xi - \zeta)(\hat{c}_X + \tilde{c}_X) - (\hat{c}_S + \tilde{c}_S) \quad (7.49d)$$

$$(\partial_\tau - \partial_\xi)(\hat{v}_P + \tilde{v}_P) = -\Lambda \Theta(\xi - \zeta)(\hat{c}_X + \tilde{c}_X) \quad (7.49e)$$

$$(\partial_\tau - \partial_\xi)(\hat{v}_S + \tilde{v}_S) = \frac{1}{n_P \varrho} (\hat{c}_S + \tilde{c}_S) \quad (7.49f)$$

$$\hat{v}_P + \tilde{v}_P + \hat{v}_S + \tilde{v}_S + \hat{\varphi} + \tilde{\varphi} = 1. \quad (7.49g)$$

The boundary conditions, Eqs. (7.37) (plus the far-field condition for the flow field), are also perturbed,

$$\hat{\mathbf{u}} + \tilde{\mathbf{u}}|_{\xi \rightarrow \infty} = \hat{\mathbf{e}}_\xi, \quad (7.50a)$$

$$\hat{c}_X + \tilde{c}_X|_{\xi \rightarrow -\infty} = 0, \quad \partial_\xi(\hat{c}_X + \tilde{c}_X)|_{\xi \rightarrow \infty} = 0, \quad (7.50b)$$

$$\hat{c}_S + \tilde{c}_S|_{\xi \rightarrow -\infty} = 1, \quad \partial_\xi(\hat{c}_S + \tilde{c}_S)|_{\xi \rightarrow \infty} = 0, \quad (7.50c)$$

$$\hat{v}_P + \tilde{v}_P|_{\xi \rightarrow -\infty} = 0, \quad \hat{v}_P + \tilde{v}_P|_{\xi \rightarrow \infty} = 1, \quad (7.50d)$$

$$\hat{v}_S + \tilde{v}_S|_{\xi \rightarrow -\infty} = \varrho^{-1}, \quad \hat{v}_S + \tilde{v}_S|_{\xi \rightarrow \infty} = 0. \quad (7.50e)$$

Now, noting that the unperturbed fields are specific solutions of Eqs. (7.48) which satisfy boundary conditions (7.37), and neglecting in Eqs. (7.49) terms which are of the second or higher order in the perturbations, one recovers the system of PDEs for the perturbations,

$$\partial_\xi \tilde{u}_\xi + \partial_\eta \tilde{u}_\eta = 0 \quad (7.51a)$$

$$\tilde{u}_\xi = \hat{K}(\hat{\varphi}) \partial_\xi \tilde{p} + \hat{K}'(\hat{\varphi}) \tilde{\varphi} \partial_\xi \hat{p} \quad (7.51b)$$

$$\tilde{u}_\eta = \hat{K}(\hat{\varphi}) \partial_\eta \tilde{p} \quad (7.51c)$$

$$\partial_\xi \tilde{c}_X + \tilde{u}_\xi \partial_\xi \hat{c}_X - H \partial_\xi^2 \tilde{c}_X - H \partial_\eta^2 \tilde{c}_X = -\Lambda \tilde{c}_X \Theta(\xi - \zeta) \quad (7.51d)$$

$$\partial_\xi \tilde{c}_S + \tilde{u}_\xi \partial_\xi \hat{c}_S - H \partial_\xi^2 \tilde{c}_S - H \partial_\eta^2 \tilde{c}_S = n_P \Lambda \Theta(\xi - \zeta) \tilde{c}_X - \tilde{c}_S \quad (7.51e)$$

$$\partial_\tau \tilde{v}_P - \partial_\xi \tilde{v}_P = -\Lambda \Theta(\xi - \zeta) \tilde{c}_X \quad (7.51f)$$

$$\partial_\tau \tilde{v}_S - \partial_\xi \tilde{v}_S = \frac{1}{n_P \rho} \tilde{c}_S \quad (7.51g)$$

$$\tilde{v}_P + \tilde{v}_S + \tilde{\varphi} = 0 \quad (7.51h)$$

accompanied by far-field boundary conditions

$$\tilde{\mathbf{u}}|_{\xi \rightarrow \infty} = 0, \quad (7.52a)$$

$$\tilde{c}_X|_{\xi \rightarrow -\infty} = 0, \quad \partial_\xi \tilde{c}_X|_{\xi \rightarrow \infty} = 0, \quad (7.52b)$$

$$\tilde{c}_S|_{\xi \rightarrow -\infty} = 0, \quad \partial_\xi \tilde{c}_S|_{\xi \rightarrow \infty} = 0, \quad (7.52c)$$

$$\tilde{v}_P|_{\xi \rightarrow -\infty} = 0, \quad \tilde{v}_P|_{\xi \rightarrow \infty} = 0, \quad (7.52d)$$

$$\tilde{v}_S|_{\xi \rightarrow -\infty} = 0, \quad \tilde{v}_S|_{\xi \rightarrow \infty} = 0. \quad (7.52e)$$

After defining

$$W(\hat{\varphi}(\xi)) \equiv \frac{\hat{K}'(\hat{\varphi})}{\hat{K}(\hat{\varphi})}, \quad (7.53)$$

the flow equations (7.51a–7.51c) can be combined to eliminate  $\tilde{p}$  and  $\tilde{u}_\eta$ ,

$$\hat{\nabla}^2 \tilde{u}_\xi = W(\partial_\eta^2 \tilde{\varphi} + \hat{\varphi}' \partial_\xi \tilde{u}_\xi). \quad (7.54)$$

The  $W = W(\hat{\varphi}(\xi))$  function will be referred to as a permeability gain factor. It measures a relative increase of permeability due to a small porosity increase. As can be deduced just by looking at Eq. (7.54), it plays a fundamental role in the stability analysis.

From now on, we will focus on two limiting cases: either  $H \rightarrow 0$ , or  $\Lambda \rightarrow \infty$ .

## 7.4.2 LSA in the limit of negligible dispersion

### Base solutions

If the characteristic diffusion length  $l_X^u$ , Eq. (7.40), is much smaller than other length scales characterizing the front profile (Eqs. (7.41–7.43)),

$$l_X^u \ll l_X^d, \quad l_X^u \ll l_S^u, \quad l_X^u \ll l_S^d, \quad (7.55)$$

then dispersion can be neglected. In our scaling, it is equivalent to taking the limit  $H \rightarrow 0$ . Since

$$\lim_{H \rightarrow 0} \Gamma_1 = 1, \quad \lim_{H \rightarrow 0} \Gamma_2 = \Lambda, \quad \lim_{H \rightarrow 0} H \Gamma_1^* = 1, \quad (7.56)$$

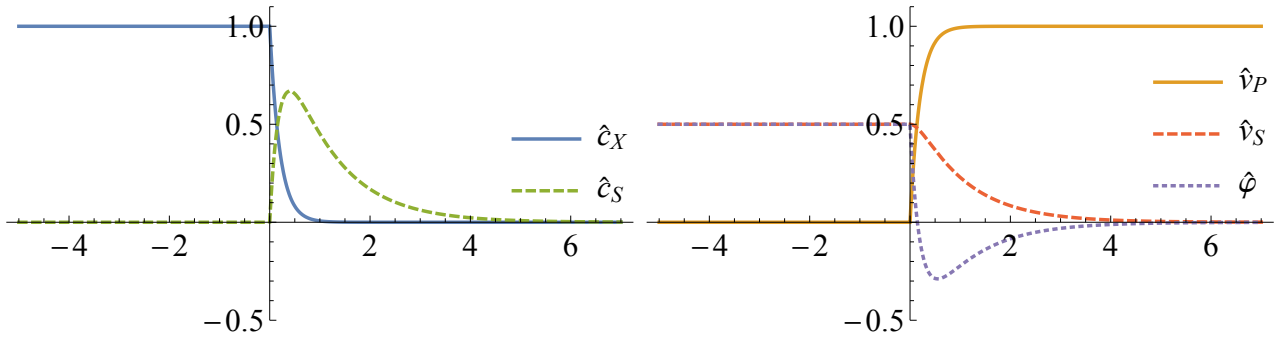


Figure 7.5: One-dimensional stationary solutions, Eqs. (7.57), of the infiltration-driven replacement model, Eqs. (7.18), for  $n_P = 1$ ,  $H \rightarrow 0$ ,  $\Lambda = 5$ , and  $\varrho = 2$ . Left panel: concentrations. Right panel: specific volumes and porosity.

the stationary replacement front profile in the zero-dispersion limit is given by

$$\hat{c}_X(\xi) = \begin{cases} 1, & \xi < 0, \\ e^{-\Lambda\xi}, & \xi > 0, \end{cases} \quad (7.57a)$$

$$\hat{c}_S(\xi) = \begin{cases} 0, & \xi < 0, \\ \frac{n_P\Lambda}{\Lambda-1} (e^{-\xi} - e^{-\Lambda\xi}), & \xi > 0, \end{cases} \quad (7.57b)$$

$$\hat{v}_P(\xi) = \begin{cases} 0, & \xi < 0, \\ 1 - e^{-\Lambda\xi}, & \xi > 0, \end{cases} \quad (7.57c)$$

$$\hat{v}_S(\xi) = \begin{cases} \varrho^{-1}, & \xi < 0, \\ \varrho^{-1} \frac{1}{\Lambda-1} (\Lambda e^{-\xi} - e^{-\Lambda\xi}), & \xi > 0. \end{cases} \quad (7.57d)$$

The front profile is illustrated in Fig. 7.5. Since the dispersive fluxes vanish, the concentration, and consequently the volume fraction profiles, are constant upstream ( $\xi < 0$ ). The expression for the minimal porosity has a relatively simple form,

$$\min_{\xi} \hat{\varphi} = -\varrho^{-1}((\Lambda-1)\varrho+1)^{1/(1-\Lambda)}. \quad (7.58)$$

## Dynamics of the perturbations

Taking the limit  $H \rightarrow 0$  in the equations for the perturbations, (7.51), is trivial. However, due to the discontinuity in the dissolution term, it is more convenient to consider the upstream ( $\xi < \zeta$ ) and downstream ( $\xi > \zeta$ ) perturbations separately.

### Perturbations upstream

Upstream the primary mineral is by definition absent, so  $\tilde{v}_P = 0$ . The transport and the secondary mineral volume evolution equations for the perturbations are

$$\partial_{\xi} \tilde{c}_S = -\tilde{c}_S \quad (7.59a)$$

$$\partial_{\xi} \tilde{c}_X = 0 \quad (7.59b)$$

$$\partial_{\tau} \tilde{v}_S - \partial_{\xi} \tilde{v}_S = \frac{1}{n_P \rho} \tilde{c}_S \quad (7.59c)$$

$$-\tilde{\varphi} = \tilde{v}_S. \quad (7.59d)$$

The only solutions for the concentrations perturbations which satisfy the far-upstream boundary conditions  $\tilde{c}_X|_{\xi \rightarrow -\infty} = \tilde{c}_S|_{\xi \rightarrow -\infty} = 0$  are

$$\tilde{c}_X = \tilde{c}_S = 0. \quad (7.60)$$

Due to the exponential time-dependence of the perturbations (see Eq. (7.47)), Eq. (7.59c) can be rewritten as an ODE for the  $\xi$ -dependent perturbation amplitude,

$$\hat{\sigma} f_{v_S} - \partial_\xi f_{v_S} = 0. \quad (7.61)$$

Since the growth rate  $\hat{\sigma}$  can have any sign and the perturbation should vanish far upstream,  $\tilde{v}_S|_{\xi \rightarrow -\infty} = 0$ , the only admissible solution of Eq. (7.61) is

$$\tilde{v}_S = 0. \quad (7.62)$$

As a result, the porosity perturbation also vanishes,  $\tilde{\varphi} = 0$ . Since the (unperturbed) porosity upstream is constant in the regime of  $H \rightarrow 0$ , Eq. (7.54) coupling the perturbations of the Darcy velocity and the porosity, reduces to the Laplace equation for the Darcy velocity perturbation,

$$\tilde{\nabla}^2 \tilde{u}_\xi = 0. \quad (7.63)$$

As the  $\eta$ -dependent part of any perturbation is harmonic (see Eq. (7.47)), Eq. (7.63) can be written as an ODE for the perturbation amplitude,

$$(\partial_\xi^2 - \hat{k}^2) f_{u_\xi} = 0, \quad (7.64)$$

whose only solution which is finite at  $\xi \rightarrow -\infty$  is

$$f_{u_\xi}(\xi) = A e^{\hat{k}\xi}, \quad (7.65)$$

where the constant  $A$  will have to be determined from the continuity with the analogous solution downstream.

## Perturbations downstream

Downstream the equations for the perturbations are

$$\partial_\xi \tilde{c}_X + \tilde{u}_\xi \partial_\xi \hat{c}_X = -\Lambda \tilde{c}_X \quad (7.66a)$$

$$\partial_\xi \tilde{c}_S + \tilde{u}_\xi \partial_\xi \hat{c}_S = n_P \Lambda \tilde{c}_X - \tilde{c}_S \quad (7.66b)$$

$$\partial_\tau \tilde{v}_P - \partial_\xi \tilde{v}_P = -\Lambda \tilde{c}_X \quad (7.66c)$$

$$\partial_\tau \tilde{v}_S - \partial_\xi \tilde{v}_S = \frac{1}{n_P \varrho} \tilde{c}_S \quad (7.66d)$$

$$-\tilde{\varphi} = \tilde{v}_S + \tilde{v}_P, \quad (7.66e)$$

plus the equation (7.54) for the Darcy velocity perturbation. Using Eqs. (7.54) and (7.66a,c-e) one can express the perturbation amplitudes in the form of various differential operators acting on  $v_{v_P}$ ,

$$f_{c_X} = -\Lambda^{-1} (\hat{\sigma} - \partial_\xi) f_{v_P} \quad (7.67a)$$

$$f_{u_\xi} = -(\hat{c}'_X)^{-1} (\Lambda + \partial_\xi) f_{c_X} \quad (7.67b)$$

$$f_\varphi = -\frac{1}{\hat{k}^2} \left( \frac{1}{W} \hat{\nabla}^2 - \hat{\varphi}' \partial_\xi \right) f_{u_\xi} \quad (7.67c)$$

$$f_{v_S} = -f_{v_P} - f_\varphi \quad (7.67d)$$

$$f_{c_S} = n_P \varrho (\hat{\sigma} - \partial_\xi) f_{v_S}. \quad (7.67e)$$

The remaining equation (7.66b) allows us to reduce Eqs. (7.54) and (7.66) to a single 6th-order linear ODE for the  $f_{v_P}(\xi)$  amplitude,

$$\begin{aligned} (1 + \partial_\xi)(\hat{\sigma} - \partial_\xi) \left( \frac{1}{W}(\partial_\xi^2 - \hat{k}^2) - \hat{\varphi}'\partial_\xi \right) \frac{\Lambda}{\hat{c}'_X}(\Lambda + \partial_\xi)(\hat{\sigma} - \partial_\xi)f_{v_P} = \\ = \hat{k}^2 \left( \Lambda^2 (1 - \varrho^{-1} + \partial_\xi) - \frac{\Lambda}{n_P \varrho} \frac{\hat{c}'_S}{\hat{c}'_X}(\Lambda + \partial_\xi) \right) (\hat{\sigma} - \partial_\xi)f_{v_P}, \end{aligned} \quad (7.68)$$

which will be solved for  $\xi > 0$ . In the above,  $\hat{c}_{H,S}$  denote the stationary downstream solutions, (7.57a–b).

The far-downstream boundary conditions follow from the perturbed boundary conditions (7.50). In the limit of  $H \rightarrow 0$  there are three of them,

$$\lim_{\xi \rightarrow \infty} f_{u_\xi} = \lim_{\xi \rightarrow \infty} f_{v_P} = \lim_{\xi \rightarrow \infty} f_{v_S} = 0. \quad (7.69)$$

Using the relations (7.67), they can be written as boundary conditions for  $f_{v_P}$ .

### Continuity conditions

Continuity conditions for the perturbations follow from the continuity conditions in the general model. Continuity of the normal component of the Darcy velocity across the front,

$$(\hat{\mathbf{u}} + \tilde{\mathbf{u}}) \cdot (\mathbf{n} + \tilde{\mathbf{n}})|_{\xi \rightarrow \zeta^-} = (\hat{\mathbf{u}} + \tilde{\mathbf{u}}) \cdot (\mathbf{n} + \tilde{\mathbf{n}})|_{\xi \rightarrow \zeta^+} \quad (7.70)$$

(note that the vector normal to the front is also perturbed), after linearization yields

$$\tilde{u}_\xi|_{\xi \rightarrow 0^-} = \tilde{u}_\xi|_{\xi \rightarrow 0^+}. \quad (7.71)$$

Additionally, continuity of pressure,

$$\hat{p} + \tilde{p}|_{\xi \rightarrow \zeta^-} = \hat{p} + \tilde{p}|_{\xi \rightarrow \zeta^+}, \quad (7.72)$$

gives

$$\partial_\xi \tilde{u}_\xi|_{\xi \rightarrow 0^-} = \partial_\xi \tilde{u}_\xi|_{\xi \rightarrow 0^+}, \quad (7.73)$$

where we have used the fact that the stationary permeability profile is continuous. The upstream amplitude of the Darcy velocity perturbation is the exponential function (7.65), known up to the constant  $A$ . Now Eqs. (7.71) and (7.73) can be combined into a single one in order to eliminate  $A$ ,

$$(\partial_\xi - \hat{k})f_{u_\xi} \Big|_{\xi \rightarrow 0^+} = 0. \quad (7.74)$$

Both concentration fields have to be continuous across the front,

$$\hat{c}_X + \tilde{c}_X|_{\xi \rightarrow \zeta^-} = \hat{c}_X + \tilde{c}_X|_{\xi \rightarrow \zeta^+}, \quad (7.75)$$

$$\hat{c}_S + \tilde{c}_S|_{\xi \rightarrow \zeta^-} = \hat{c}_S + \tilde{c}_S|_{\xi \rightarrow \zeta^+}. \quad (7.76)$$

Since upstream both perturbations vanish, linearization of the above conditions gives

$$f_{c_X}|_{\xi \rightarrow 0^+} = -\zeta_0 \hat{c}'_X|_{\xi \rightarrow 0^+} = \Lambda \zeta_0, \quad (7.77)$$

$$f_{c_S}|_{\xi \rightarrow 0^+} = -\zeta_0 \hat{c}'_S|_{\xi \rightarrow 0^+} = -n_P \Lambda \zeta_0. \quad (7.78)$$

Lastly, the primary mineral volume fraction should vanish exactly at the front,

$$0 = \hat{v}_P + \tilde{v}_P|_{\xi \rightarrow \zeta^+}, \quad (7.79)$$

which gives

$$f_{v_P}|_{\xi \rightarrow 0^+} = -\zeta_0 \hat{v}'_P|_{\xi \rightarrow 0^+} = -\Lambda \zeta_0. \quad (7.80)$$

Three boundary conditions at  $\xi \rightarrow \infty$ , plus three at  $\xi = 0$ , allow one to solve Eq. (7.68) up to the (arbitrary) front perturbation amplitude  $\zeta_0$ . The fourth boundary condition at  $\xi = 0$  can then be used to find the dispersion relation between the perturbation growth rate  $\hat{\sigma}$  and the wavenumber  $\hat{k}$ . The dispersion relation  $\hat{\sigma} = \hat{\sigma}(\hat{k})$  depends on two parameters:  $\varrho$ , and  $\Lambda$ , as well as on the choice of the permeability model (through the permeability gain function  $W$ ). The value of the stoichiometric number  $n_P$  is irrelevant here, since it reduces after inserting the explicit formula for  $\hat{c}_S(\xi)$  into the ODE and the boundary conditions.

Equation (7.68) in general does not have an analytical solution and has to be solved numerically (see Appendix A for details). However, some approximate analytical treatment of the problem is possible. In principle, in the limit of small  $W$  it is possible to obtain strict analytical solutions up to an arbitrary order in  $W$ . We will apply this procedure in the following section.

### Expansion in small $W$

Defining the following set of differential operators,

$$\mathcal{K} = 1 + \partial_\xi = e^{-\xi} \partial_\xi e^\xi \quad (7.81)$$

$$\mathcal{S} = \hat{\sigma} - \partial_\xi = -e^{\hat{\sigma}\xi} \partial_\xi e^{-\hat{\sigma}\xi} \quad (7.82)$$

$$\mathcal{P} = \partial_\xi e^{\Lambda\xi} \quad (7.83)$$

$$\mathcal{M} = -\hat{k}^2 \left( \Lambda^2 (1 - \varrho^{-1} + \partial_\xi) + \frac{1}{n_P \varrho} \mathcal{C}'_S \partial_\xi e^{\Lambda\xi} \right) \quad (7.84)$$

$$\mathcal{F} = -\hat{\varphi}' \partial_\xi \quad (7.85)$$

$$\mathcal{L} = \partial_\xi^2 - \hat{k}^2 \quad (7.86)$$

$$\mathcal{J} = \partial_\xi - \hat{k} = e^{\hat{k}\xi} \partial_\xi e^{-\hat{k}\xi}, \quad (7.87)$$

we can state the problem of finding the dispersion relation as

$$\left( \mathcal{K} \mathcal{S} \left( \frac{1}{W} \mathcal{L} + \mathcal{F} \right) \mathcal{P} - \mathcal{M} \right) \mathcal{S} f_{v_P} = 0, \quad \xi > 0 \quad (7.88a)$$

$$f_{v_P}|_{\xi=0} = -\Lambda \xi_0 \quad (7.88b)$$

$$(\mathcal{S} - \Lambda) f_{v_P}|_{\xi=0} = 0 \quad (7.88c)$$

$$\left( \left( -\frac{1}{W} \mathcal{S} \mathcal{J} + \mathcal{F} \right) \mathcal{P} + \hat{k}^2 \Lambda \right) \mathcal{S} f_{v_P} \Big|_{\xi=0} = 0 \quad (7.88d)$$

$$\left( \mathcal{S} \left( \frac{1}{W} \mathcal{L} + \mathcal{F} \right) \mathcal{P} + \hat{k}^2 \Lambda (\Lambda + \varrho^{-1}) \right) \mathcal{S} f_{v_P} \Big|_{\xi=0} = 0 \quad (7.88e)$$

$$f_{v_P}|_{\xi \rightarrow \infty} = 0 \quad (7.88f)$$

$$\mathcal{S} f_{v_P}|_{\xi \rightarrow \infty} = 0 \quad (7.88g)$$

$$\mathcal{P} \mathcal{S} f_{v_P}|_{\xi \rightarrow \infty} = 0 \quad (7.88h)$$

$$\left( \frac{1}{W} \mathcal{L} + \mathcal{F} \right) \mathcal{P} \mathcal{S} f_{v_P} \Big|_{\xi \rightarrow \infty} = 0 \quad (7.88i)$$

$$\mathcal{S} \left( \frac{1}{W} \mathcal{L} + \mathcal{F} \right) \mathcal{P} \mathcal{S} f_{v_P} \Big|_{\xi \rightarrow \infty} = 0 \quad (7.88j)$$

In the case of small (and constant)  $W$ , one can expand both the solution of Eq. (7.68),  $f_{v_P}$ , and the growth rate  $\hat{\sigma}$  in the powers of  $W$ ,

$$f_{v_P} = f_0 + Wf_1 + W^2f_2 + \dots \quad (7.89)$$

$$\hat{\sigma} = \hat{\sigma}_0 + W\hat{\sigma}_1 + W^2\hat{\sigma}_2 + \dots \quad (7.90)$$

Now one needs to insert these forms into (7.88), and expand the ODE, as well as the boundary conditions, in subsequent powers of  $W$ . In zeroth order the procedure yields

$$\mathcal{K}\mathcal{S}_0\mathcal{L}\mathcal{P}\mathcal{S}_0f_0 = 0 \quad (7.91a)$$

$$f_0|_{\xi=0} = -\Lambda\zeta_0 \quad (7.91b)$$

$$(-\Lambda + \mathcal{S}_0)f_0|_{\xi=0} = 0 \quad (7.91c)$$

$$\mathcal{S}_0\mathcal{J}\mathcal{P}\mathcal{S}_0f_0|_{\xi=0} = 0 \quad (7.91d)$$

$$\mathcal{S}_0\mathcal{L}\mathcal{P}\mathcal{S}_0f_0|_{\xi=0} = 0 \quad (7.91e)$$

$$f_0|_{\xi\rightarrow\infty} = 0 \quad (7.91f)$$

$$\mathcal{S}_0f_0|_{\xi\rightarrow\infty} = 0 \quad (7.91g)$$

$$\mathcal{P}\mathcal{S}_0f_0|_{\xi\rightarrow\infty} = 0 \quad (7.91h)$$

$$\mathcal{L}\mathcal{P}\mathcal{S}_0f_0|_{\xi\rightarrow\infty} = 0 \quad (7.91i)$$

$$\mathcal{S}_0\mathcal{L}\mathcal{P}\mathcal{S}_0f_0|_{\xi\rightarrow\infty} = 0 \quad (7.91j)$$

where, by analogy to (7.82),  $\mathcal{S}_0 = \hat{\sigma}_0 - \partial_\xi$ . Solving Eqs. (7.91), one obtains the solution for  $\hat{\sigma}_0$ ,

$$\hat{\sigma}_0 = 0 \quad (7.92a)$$

$$f_0 = -\xi_0\Lambda e^{-\Lambda\xi} \quad (7.92b)$$

$$\mathcal{S}_0f_0 = -\xi_0\Lambda^2 e^{-\Lambda\xi} \quad (7.92c)$$

$$\mathcal{P}\mathcal{S}_0f_0 = 0 \quad (7.92d)$$

$$\mathcal{P}f_0 = 0 \quad (7.92e)$$

$$\mathcal{M}\mathcal{S}_0f_0 = \xi_0\hat{k}^2\Lambda^4(1 - \varrho^{-1} - \Lambda)e^{-\Lambda\xi}. \quad (7.92f)$$

Considering the first order contribution in Eqs. (7.88), one gets

$$\mathcal{K}\mathcal{S}_0\mathcal{L}\mathcal{P}\mathcal{S}_0f_1 = -\mathcal{K}\mathcal{S}_0\mathcal{F}\mathcal{P}\mathcal{S}_0f_0 - \hat{\sigma}_1\mathcal{K}\mathcal{L}\mathcal{P}\mathcal{S}_0f_0 + \mathcal{M}\mathcal{S}_0f_0 - \hat{\sigma}_1\mathcal{K}\mathcal{S}_0\mathcal{L}\mathcal{P}f_0 \quad (7.93a)$$

$$f_1|_{\xi=0} = 0 \quad (7.93b)$$

$$(-\Lambda + \mathcal{S}_0)f_1 + \hat{\sigma}_1f_0|_{\xi=0} = 0 \quad (7.93c)$$

$$-\mathcal{S}_0\mathcal{J}\mathcal{P}\mathcal{S}_0f_1 - \mathcal{S}_0\mathcal{J}\mathcal{P}\hat{\sigma}_1f_0 + (-\hat{\sigma}_1\mathcal{J}\mathcal{P} + \mathcal{F}\mathcal{P} + \hat{k}^2\Lambda)\mathcal{S}_0f_0\Big|_{\xi=0} = 0 \quad (7.93d)$$

$$\left(\mathcal{S}_0\mathcal{F}\mathcal{P} + \hat{\sigma}_1\mathcal{L}\mathcal{P} + \hat{k}^2\Lambda(\Lambda + \varrho^{-1})\right)\mathcal{S}_0f_0 + \mathcal{S}_0\mathcal{L}\mathcal{P}(\hat{\sigma}_1f_0 + \mathcal{S}_0f_1)\Big|_{\xi=0} = 0 \quad (7.93e)$$

$$f_1|_{\xi\rightarrow\infty} = 0 \quad (7.93f)$$

$$\mathcal{S}_0f_1|_{\xi\rightarrow\infty} = 0 \quad (7.93g)$$

$$\mathcal{P}\mathcal{S}_0f_1|_{\xi\rightarrow\infty} = 0 \quad (7.93h)$$

$$\mathcal{L}\mathcal{P}(\mathcal{S}_0f_1 + \hat{\sigma}_1f_0) + \mathcal{F}\mathcal{P}\mathcal{S}_0f_0|_{\xi\rightarrow\infty} = 0 \quad (7.93i)$$

$$\mathcal{S}_0\mathcal{F}\mathcal{P}\mathcal{S}_0f_0 + \mathcal{S}_0\mathcal{L}\mathcal{P}(\mathcal{S}_0f_1 + \hat{\sigma}_1f_0) + \hat{\sigma}_1\mathcal{L}\mathcal{P}\mathcal{S}_0f_0|_{\xi\rightarrow\infty} = 0 \quad (7.93j)$$

which can be simplified after inserting the zeroth order solutions (7.92). Solving for  $f_1$  and  $\hat{\sigma}_1$ , one gets:

$$\hat{\sigma}_1 = \frac{\Lambda\hat{k}\left(\hat{k}^2((\Lambda + 1)\varrho - 1) + \Lambda(\Lambda + 1)(\varrho - 1) + \hat{k}(\Lambda^2\varrho + 2\Lambda(\varrho - 1) + \varrho - 1)\right)}{2(\Lambda + 1)\varrho(\hat{k} + 1)(\Lambda + \hat{k})^2}. \quad (7.94)$$

Since the zeroth term of the expansion is  $\hat{\sigma}_0 = 0$ , the two-term expansion of  $\hat{\sigma}$  is

$$\hat{\sigma}(\hat{k}; H \rightarrow 0, \Lambda, W, \varrho) \approx W \frac{\Lambda \hat{k} \left( \hat{k}^2 ((\Lambda + 1)\varrho - 1) + \Lambda(\Lambda + 1)(\varrho - 1) + \hat{k} (\Lambda^2 \varrho + 2\Lambda(\varrho - 1) + \varrho - 1) \right)}{2(\Lambda + 1)\varrho(\hat{k} + 1)(\Lambda + \hat{k})^2}. \quad (7.95)$$

## Discussion of the results

As mentioned before, except for the small- $W$  case, Eqs. (7.68) do not have in general analytical solutions and have to be solved numerically. We have applied the boundary-bordering, pseudo-spectral method [78, 79] (see Appendix A for details) in order to solve them and to find the dispersion relations.

The length and time scales used for the scaling in Sec. (7.2), although convenient during the derivations, are not the most reasonable ones when it comes to interpreting the results. In the illustrating figures we will use different scalings, which should provide a deeper insight into the studied instability. Spatial coordinates will be scaled by  $l_S^d$  (Eq. (7.43)), which is the largest characteristic length for  $\Lambda > 1$  and  $H < 2$ . As the time scale we choose the one associated with the selected length scale:  $l_S^d/U$ , where  $U$  is the velocity of the planar front (Eq. (7.26)).

As both the numerical and analytical solutions show, perturbations of zero wavenumber are marginally stable,

$$\sigma(k = 0) = 0. \quad (7.96)$$

This is not surprising, since an infinite-wavelength perturbation of the front is a mere translation, a transformation neutral for an infinitely long ( $-\infty < \xi < \infty$ ) system.

Stability of the front with respect to long-wave ( $k \gtrsim 0$ ) perturbations should depend on the far-field permeability contrast. Indeed, Eq. (7.95) yields

$$U^{-1} \frac{d\sigma}{dk} \Big|_{k=0} = W \frac{\varrho - 1}{2\varrho}. \quad (7.97)$$

The sign of (7.97) is governed by the term  $(\varrho - 1)$ . If  $\varrho > 1$  (i.e. the secondary phase is more porous than the primary phase), long-wave perturbations are unstable, and vice versa. The result is analogous to Eq. (3.82) derived for the one-component reactive-infiltration instability. Indeed, the permeability ratio  $\kappa$  is now equal to

$$\kappa = \frac{e^{W\hat{\varphi}(\xi \rightarrow -\infty)}}{e^{W\hat{\varphi}(\xi \rightarrow \infty)}} = e^{W(1-\varrho^{-1})}. \quad (7.98)$$

Assuming that  $W \ll 1$ , Eq. (3.82) can be rewritten as

$$\hat{\sigma}'(\hat{k}) \Big|_{\hat{k}=0} = \frac{\kappa - 1}{\kappa + 1} = \frac{e^{W(1-\varrho^{-1})} - 1}{e^{W(1-\varrho^{-1})} + 1} \approx \frac{W(1-\varrho^{-1})}{2} = W \frac{\varrho - 1}{2\varrho}, \quad (7.99)$$

which is exactly the same result as the one derived for a more complicated dissolution-precipitation system, Eq. (7.97). It shows that the details of the model are not important from the point of view of the long-wavelength stability. What only matters is the permeability ratio between the primary and the secondary phases.

For equal far-upstream and far-downstream porosities ( $\rho = 1$ ), we have  $\sigma'(k = 0) = 0$ , and one needs to study higher derivatives to assess the front stability with respect to long-wave perturbations. As it can be easily checked,

$$\hat{\sigma}''(\hat{k}; \varrho = 1) \Big|_{\hat{k}=0} = W \frac{\Lambda}{\Lambda + 1} > 0, \quad (7.100)$$

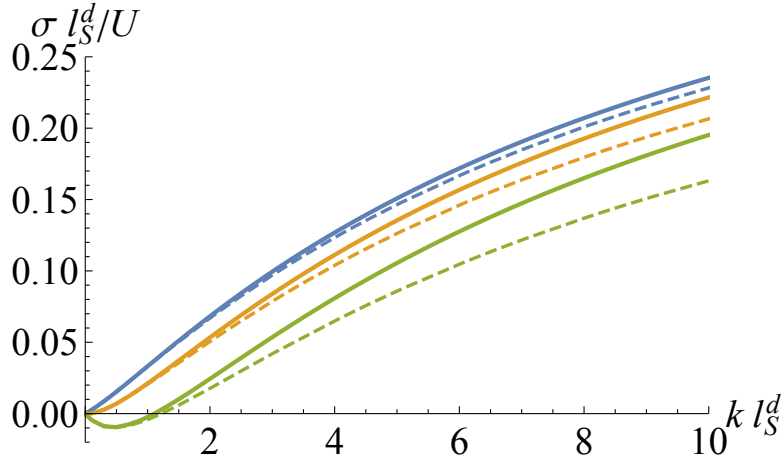


Figure 7.6: Dispersion curves for  $\Lambda = 10$ ,  $H \rightarrow 0$ ,  $W = 0.1$ , and  $\varrho = 2, 1, 0.5$  (top to bottom). The numerical solutions (solid lines) are close to the small- $W$  approximate ones (dashed lines; Eq. (7.95)), especially in the small- $k$  part of the spectrum.

so in the case of negligible dispersion, long-wave perturbations destabilize the front. Note that an opposite result was derived in case of the standard reactive-infiltration instability, Eq. (3.83). The complete dispersion curves for various  $\varrho$  are shown in Fig. 7.6. Note that the small- $W$  analytical approximations are quite close to the numerical solutions which are available for arbitrary  $W$ . The overlap of these curves is especially remarkable for small  $k$ . Short-wave perturbations are unstable even if  $\varrho = 0.5 < 1$ . Such a behaviour of the front is fundamentally different from the one observed for a simple dissolution or precipitation front, where the front is always unstable for  $\varrho > 1$  ( $\kappa > 1$ ) and stable for  $\varrho < 1$  ( $\kappa < 1$ ) [19].

In the small- $W$  case the growth rate of short-wavelength perturbations can be found by studying the asymptotic behaviour of Eq. (7.95),

$$\lim_{\hat{k} \rightarrow \infty} \hat{\sigma} = W \frac{\Lambda(\Lambda\varrho + \varrho - 1)}{2(\Lambda + 1)\rho}, \quad (7.101)$$

which is positive whenever  $\varrho > (\Lambda + 1)^{-1}$ . In case of large  $W$  in the exponential permeability model, or in case of the cubic permeability model, the dispersion curves for  $H \rightarrow 0$  also have horizontal asymptotes at  $\hat{k} \rightarrow \infty$  (see Figs. 7.7–7.8). However, by analogy with the one-component dissolution, we expect that any finite dispersion ( $H > 0$ ) would stabilize short-wavelength perturbations.

Next, we analyze the influence of  $\Lambda$  on the system instability. As shown in Fig. 7.7, in case of the exponential permeability model, increasing the reaction rate contrast  $\Lambda$  destabilizes the front. Such an observation can be explained by noting that while the maximal porosity is constant (for constant  $v_P^{max}$ ), the minimal porosity is a decreasing function of  $\Lambda$  (cf. Eq. (7.58)). As a consequence, in our model an increase of  $\Lambda$  is associated with an increase of porosity and permeability contrasts across the front. In case of the cubic permeability model, the system behaves in a qualitatively similar manner (Fig. 7.8). However, in the latter case the instability is stronger ( $\max \sigma$  is higher). This observation can be explained by noting that the instability gets stronger for larger values of the permeability gain factor  $W$  (Eq. (7.53)). For the cubic permeability model,  $W$  is given by

$$W = W(\xi) = \frac{\hat{K}'(\hat{\varphi})}{\hat{K}(\hat{\varphi})} = \frac{3v_P^{max}}{\varphi(\xi)}. \quad (7.102)$$

If  $v_P^{max} = 0.5$  (as in Fig. 7.8),  $\max_{\xi} W = 3$ , which is larger than (constant)  $W = 1$  from

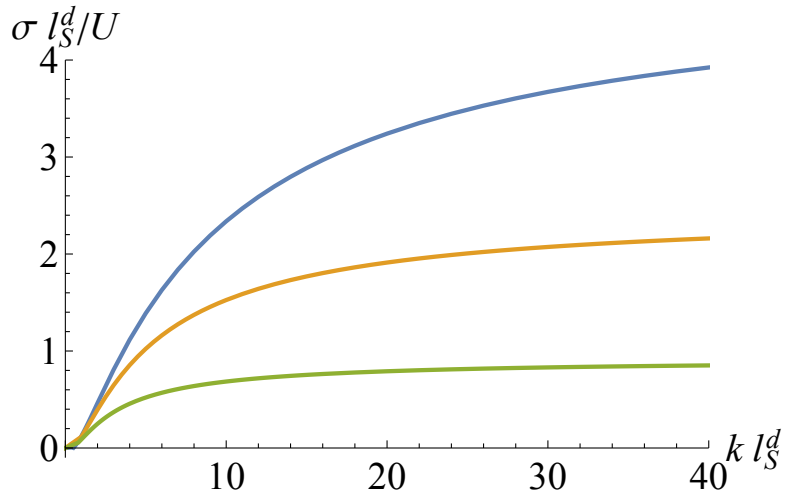


Figure 7.7: Dispersion curves for  $H \rightarrow 0$ ,  $\varrho = 1$ ,  $W = 1$ , and  $\Lambda = 10, 5, 2$  (top to bottom). The exponential permeability model was assumed. The higher  $\Lambda$ , the stronger is the instability.

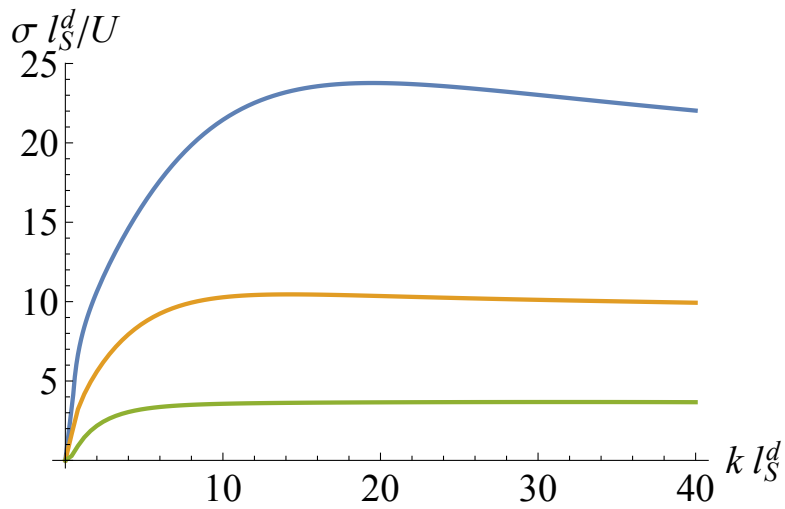


Figure 7.8: Dispersion curves for  $H \rightarrow 0$ ,  $\varrho = 1$ ,  $v_P^{max} = 0.5$ , and  $\Lambda = 10, 5, 2$  (top to bottom). The cubic permeability model was assumed. The higher  $\Lambda$ , the stronger is the instability.

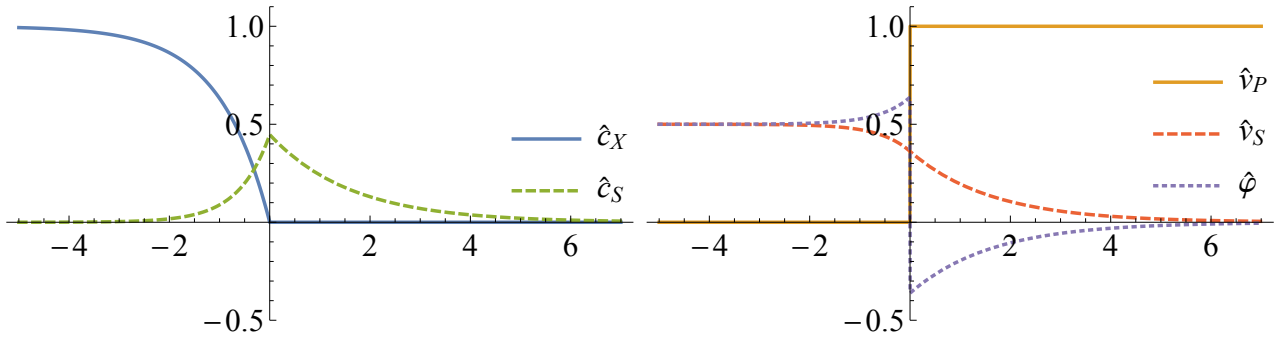


Figure 7.9: One-dimensional stationary solutions, Eqs. (7.103), of the infiltration-driven replacement model, Eqs. (7.18), for  $n_P = 1$ ,  $H = 1$ ,  $\Lambda \rightarrow \infty$ , and  $\varrho = 2$ . Left panel: concentrations. Right panel: specific volumes and porosity.

Fig. 7.7. Therefore we expect that the instability is stronger for the cubic permeability model from Fig. 7.8 than for the exponential one with  $W = 1$  from Fig. 7.7.

### 7.4.3 LSA in the limit of quick dissolution

#### Base solutions

In geochemical systems dissolution often occurs more rapidly than precipitation. The difference between these reaction rates can be even as high as a few orders of magnitude. In our model the relative rate of the reactions is controlled by the  $\Lambda$  parameter (see Eq. (7.20)). The assumption that dissolution is much faster than precipitation is thus equivalent to taking the limit  $\Lambda \rightarrow \infty$ . After noting that  $\Gamma_2 \sim \sqrt{\Lambda/H}$  for large  $\Lambda$ , one recovers the stationary profiles in this limit,

$$\hat{c}_X(\xi) = \begin{cases} 1 - e^{\xi/H}, & \xi < 0, \\ 0, & \xi > 0, \end{cases} \quad (7.103a)$$

$$\hat{c}_S(\xi) = \begin{cases} \frac{n_P}{\sqrt{1+4H}} e^{\Gamma_1^* \xi}, & \xi < 0, \\ \frac{n_P}{\sqrt{1+4H}} e^{-\Gamma_1 \xi}, & \xi > 0, \end{cases} \quad (7.103b)$$

$$\hat{v}_P(\xi) = \begin{cases} 0, & \xi < 0, \\ 1, & \xi > 0, \end{cases} \quad (7.103c)$$

$$\hat{v}_S(\xi) = \begin{cases} \varrho^{-1} \left( 1 - \frac{1}{2 + \Gamma_1^*} e^{\Gamma_1^* \xi} \right), & \xi < 0, \\ \varrho^{-1} \frac{1}{2 - \Gamma_1} e^{-\Gamma_1 \xi}, & \xi > 0. \end{cases} \quad (7.103d)$$

The front profile is illustrated in Fig. 7.9. Note that the X ion penetration length has dropped to zero and the primary mineral volume fraction profile is discontinuous at  $\xi = 0$ . Consequently, the porosity and permeability profiles are discontinuous as well. In the limit of  $\Lambda \rightarrow \infty$  one obtains an analytical solution for the minimal porosity:

$$\min_{\xi} \hat{\varphi} = \lim_{\xi \rightarrow 0^+} \hat{\varphi} = -\varrho^{-1} \frac{1}{2 - \Gamma_1}. \quad (7.104)$$

The (unscaled) minimal porosity in this regime is thus equal to

$$\min_{\xi} \varphi = 1 - v_P^{max} \left( 1 + \varrho^{-1} \frac{1}{2 - \Gamma_1} \right) = 1 - v_P(\xi \rightarrow \infty) - \frac{v_S(\xi \rightarrow -\infty)}{2 - \Gamma_1}. \quad (7.105)$$

Also, unlike in the finite- $\Lambda$  case, the first derivatives of the concentration profiles are discontinuous.

## Dynamics of the perturbations

Taking the limit  $\Lambda \rightarrow \infty$  effectively reduces the dissolution zone to a curve  $\xi = \zeta(\eta, \tau)$  in the  $(\xi, \eta)$  plane. The primary mineral volume fraction is therefore constant on either side of the front ( $\hat{v}_P = 0$  upstream and  $\hat{v}_P = 1$  downstream) and its perturbation vanishes,  $\tilde{v}_P = 0$ . As a result, the equations for the perturbations, Eqs. (7.51), look the same both upstream and downstream,

$$\partial_\xi \tilde{u}_\xi + \partial_\eta \tilde{u}_\eta = 0 \quad (7.106a)$$

$$\tilde{u}_\xi = \hat{K}(\hat{\varphi}) \partial_\xi \tilde{p} + \hat{K}'(\hat{\varphi}) \tilde{\varphi} \partial_\xi \hat{p} \quad (7.106b)$$

$$\tilde{u}_\eta = \hat{K}(\hat{\varphi}) \partial_\eta \tilde{p} \quad (7.106c)$$

$$\partial_\xi \tilde{c}_S + \tilde{u}_\xi \partial_\xi \hat{c}_S - H \partial_\xi^2 \tilde{c}_S + H \hat{k}^2 \tilde{c}_S = -\tilde{c}_S \quad (7.106d)$$

$$\partial_\xi \tilde{c}_X + \tilde{u}_\xi \partial_\xi \hat{c}_X - H \partial_\xi^2 \tilde{c}_X + H \hat{k}^2 \tilde{c}_X = 0 \quad (7.106e)$$

$$\partial_\tau \tilde{v}_S - \partial_\xi \tilde{v}_S = \frac{1}{n_P \rho} \tilde{c}_S \quad (7.106f)$$

$$-\tilde{\varphi} = \tilde{v}_S. \quad (7.106g)$$

All the perturbation amplitudes except for  $f_{c_X}$  can be expressed as the  $f_{v_S}$  amplitude under certain differential operators,

$$f_\varphi = -f_{v_S} \quad (7.107a)$$

$$f_{c_S} = n_P \rho (\hat{\sigma} - \partial_\xi) f_{v_S} \quad (7.107b)$$

$$f_{u_\xi} = \left( -\frac{1}{\hat{c}'_S} \right) (1 + \partial_\xi - H(\partial_\xi^2 - \hat{k}^2)) f_{c_S} \quad (7.107c)$$

$$f_p = \frac{1}{\hat{k}^2 \hat{K}(\hat{\varphi})} \partial_\xi f_{u_\xi}. \quad (7.107d)$$

Eqs. (7.106a–d,f–g) can then be grouped together to yield a single, 5th order ODE for the secondary mineral volume fraction perturbation amplitude,

$$\left( \frac{1}{W} (\partial_\xi^2 - \hat{k}^2) - \hat{\varphi}' \partial_\xi \right) \left( -\frac{n_P}{\hat{c}'_S} \right) (1 + \partial_\xi - H(\partial_\xi^2 - \hat{k}^2)) (\hat{\sigma} - \partial_\xi) f_{v_S}^\pm = \frac{\hat{k}^2}{\rho} f_{v_S}^\pm. \quad (7.108)$$

The  $\pm$  indexes have been introduced to emphasize that in fact two separate ODEs have to be solved: the ODE for  $f_{v_S}^-$  ( $f_{v_S}^+$ ) is valid in the upstream (downstream) region,  $\xi < 0$  ( $\xi > 0$ ), and should satisfy vanishing boundary conditions at  $\xi \rightarrow -\infty$  ( $\xi \rightarrow \infty$ ):

$$\lim_{\xi \rightarrow \pm\infty} f_{v_S}^\pm = \lim_{\xi \rightarrow \pm\infty} \partial_\xi f_{c_S}^\pm = \lim_{\xi \rightarrow \pm\infty} f_{u_\xi}^\pm = 0. \quad (7.109)$$

They can be written as boundary conditions for  $f_{v_S}^\pm$  using relations (7.107).

## Continuity conditions

The upstream and downstream amplitudes should be matched across the front. The appropriate continuity conditions can be determined by the linearization procedure analogous to the one applied in Sec. 7.4.2. Continuity of pressure yields

$$f_p^-(0) = f_p^+(0) + \left( \frac{1}{\hat{K}_+} - \frac{1}{\hat{K}_-} \right) \zeta_0, \quad (7.110)$$

where  $\hat{K}_\pm = \hat{K}(\lim_{\xi \rightarrow 0^\pm} \hat{\varphi})$  are the permeability values in the vicinity of the dissolution zone. Note that due to the porosity (and permeability) discontinuity, the right-hand side term in Eq. (7.110) does not vanish. Next, the normal component of the Darcy velocity should be continuous across the front, which gives

$$f_{u_\xi}^-(0) = f_{u_\xi}^+(0). \quad (7.111)$$

Also the secondary ion concentration should be continuous, as well as the secondary mineral volume fraction, which gives

$$f_{c_S}^-(0) = f_{c_S}^+(0) - \frac{n_P}{H} \zeta_0, \quad f_{v_S}^-(0) = f_{v_S}^+(0). \quad (7.112)$$

In order to solve two coupled fifth-order ODEs (7.108) up to the arbitrary front perturbation amplitude  $\zeta_0$ , one needs to use three boundary conditions at  $\xi \rightarrow -\infty$ , three at  $\xi \rightarrow \infty$ , and four continuity conditions, Eqs. (7.110–7.112). The solution will depend on two parameters,  $H$  and  $\rho$ , as well as on the choice of the permeability model (both through the permeability gain function  $W$ , and the near-front permeability ratio  $\hat{K}_+/\hat{K}_-$ ). Similarly as in the  $H \rightarrow 0$  case (Sec. 7.4.2), the  $n_P$  parameter reduces after inserting the explicit formula for  $\hat{c}_S(\xi)$  into the ODEs and the boundary conditions.

This is however insufficient to get the dispersion relation. In order to relate  $\hat{\sigma}$  with  $\hat{k}$ , additional information should be utilized. In the derivation of Eqs. (7.108), we did not use neither the equation for the upstream perturbation of the solvent concentration (7.106e), nor the primary mineral volume fraction evolution equation, which is nontrivial only exactly at the front in the quick dissolution limit. Noting that the normal velocity of the (infinitely thin) dissolution front is proportional to the incoming solvent flux (see Eqs. (3.29) and (3.43), plus the discussion around these equations),

$$\hat{U}_n = (\hat{c}_X \hat{\mathbf{u}} - H \hat{\nabla} \hat{c}_X) \cdot \mathbf{e}_n, \quad (7.113)$$

and perturbing  $\hat{U}$ ,  $\hat{c}_X$ ,  $\hat{\mathbf{u}}$ , and  $\mathbf{e}_n$  in the above relation, one obtains <sup>1</sup>

$$\tilde{U} = (1 - H \partial_\xi) \tilde{c}_X|_{\xi \rightarrow 0^-}. \quad (7.119)$$

---

<sup>1</sup> The same result can be obtained in an alternative, more formal way. Reducing the dissolution reaction term, the primary mineral volume fraction evolution equation can be combined with the solvent transport equation,

$$(\partial_\tau - \hat{U} \partial_\xi) \hat{v}_P = \hat{\nabla} \cdot (\hat{c}_X \hat{\mathbf{u}} - H \hat{\nabla} \hat{c}_X). \quad (7.114)$$

Note that Eq. (7.114) is valid in the whole domain. Perturbing  $\hat{v}_P$ ,  $\hat{c}_X$ ,  $\hat{\mathbf{u}}$ , and  $\hat{U}$  in Eq. (7.114) gives

$$\hat{\sigma} \tilde{v}_P - \partial_\xi \tilde{v}_P - \tilde{U} \hat{v}'_P = \partial_\xi \tilde{c}_X + \tilde{u}_\xi \partial_\xi \hat{c}_X - H \partial_\xi^2 \tilde{c}_X + H \hat{k}^2 \tilde{c}_X. \quad (7.115)$$

Both sides of Eq. (7.115) are then integrated from  $\xi = \zeta - \epsilon$  to  $\xi = \zeta + \epsilon$ ,

$$\int_{\zeta - \epsilon}^{\zeta + \epsilon} d\xi \left( \hat{\sigma} \tilde{v}_P - \partial_\xi \tilde{v}_P - \tilde{U} \hat{v}'_P \right) = \int_{\zeta - \epsilon}^{\zeta + \epsilon} d\xi \left( \partial_\xi \tilde{c}_X + \tilde{u}_\xi \partial_\xi \hat{c}_X - H \partial_\xi^2 \tilde{c}_X + H \hat{k}^2 \tilde{c}_X \right). \quad (7.116)$$

$$\int_{\zeta - \epsilon}^{\zeta + \epsilon} \hat{\sigma} \tilde{v}_P d\xi - \tilde{v}_P|_{\zeta - \epsilon}^{\zeta + \epsilon} - \tilde{U} \hat{v}_P|_{\zeta - \epsilon}^{\zeta + \epsilon} = \tilde{c}_X|_{\zeta - \epsilon}^{\zeta + \epsilon} + \tilde{u}_\xi \hat{c}_X|_{\zeta - \epsilon}^{\zeta + \epsilon} - \int_{\zeta - \epsilon}^{\zeta + \epsilon} \hat{c}_X \partial_\xi \tilde{u}_\xi d\xi - H \partial_\xi \tilde{c}_X|_{\zeta - \epsilon}^{\zeta + \epsilon} + H \hat{k}^2 \int_{\zeta - \epsilon}^{\zeta + \epsilon} \tilde{c}_X d\xi, \quad (7.117)$$

Since  $\tilde{v}_P$  vanishes both upstream ( $\xi < \zeta$ ) and downstream ( $\xi > \zeta$ ), while  $\tilde{c}_X$  downstream, Eq. (7.117) reduces to

$$-\tilde{U} = -\tilde{c}_X|_{\xi = \zeta - \epsilon} - \tilde{u}_\xi \hat{c}_X|_{\xi = \zeta - \epsilon} - \int_{\zeta - \epsilon}^{\zeta} \hat{c}_X \partial_\xi \tilde{u}_\xi d\xi + H \partial_\xi \tilde{c}_X|_{\xi = \zeta - \epsilon} + H \hat{k}^2 \int_{\zeta - \epsilon}^{\zeta} \tilde{c}_X d\xi, \quad (7.118)$$

Lastly, taking the limit  $\epsilon \rightarrow 0^+$  and neglecting terms which are quadratic in the perturbations yields Eq. (7.119).

On the other hand, the dissolution front velocity perturbation is the time derivative of the front perturbation, Eq. (7.46),

$$\tilde{U} = \partial_\tau \zeta = \hat{\sigma} \zeta. \quad (7.120)$$

Additionally, the perturbed solvent concentration should be zero at the front,

$$\hat{c}_X + \tilde{c}_X|_{\xi \rightarrow \zeta^-} = 0, \quad (7.121)$$

and  $\tilde{c}_X$  should vanish at  $\xi \rightarrow -\infty$ . Simplifying Eqs. (7.106e) and (7.119–7.121) and expressing them in terms of the perturbation amplitudes yields

$$(\partial_\xi - H\partial_\xi^2 + H\hat{k}^2)f_{c_X}^- = \frac{1}{H}e^{\xi/H}f_{u_\xi}^-, \quad \xi < 0 \quad (7.122a)$$

$$(1 - H\partial_\xi)f_{c_X}^-(0) = \xi_0\hat{\sigma} \quad (7.122b)$$

$$f_{c_X}^-(0) = \xi_0/H \quad (7.122c)$$

$$f_{c_X}^-|_{\xi \rightarrow -\infty} = 0. \quad (7.122d)$$

Once Eqs. (7.108) are solved, the Darcy velocity perturbation can be found as

$$f_{u_\xi}^-(\xi) = -\frac{n_{P0}}{\hat{c}'_S}(1 + \partial_\xi - H(\partial_\xi^2 - \hat{k}^2))(\hat{\sigma} - \partial_\xi)f_{v_S}^-(\xi). \quad (7.123)$$

Then, two boundary conditions (7.122c–d) are sufficient to solve Eq. (7.122a) up to the perturbation amplitude  $\zeta_0$ , and the third one, Eq. (7.122b), allows one to find the dispersion relation  $\hat{\sigma} = \hat{\sigma}(\hat{k})$ . In fact, problem (7.122) can be solved analytically: the dispersion relation is given in the integral form

$$\hat{\sigma} = -\Gamma_3 + \frac{1}{H} \int_{-\infty}^0 d\xi \exp(\Gamma_3^* \xi) f_{u_\xi}^-(\xi), \quad (7.124)$$

where  $\Gamma_3 = \frac{\sqrt{1 + 4H^2\hat{k}^2} - 1}{2H}$  and  $\Gamma_3^* = \frac{\sqrt{1 + 4H^2\hat{k}^2} + 1}{2H}$ .

Similarly as in the zero-dispersion case, Eqs. (7.108) have to be solved numerically. The details of the applied numerical method are given in Appendix A. An approximate solution can be however derived in the limit of small and constant  $W$ .

### Expansion in small $W$

Analogously as in Sec. 7.4.2, we define the following differential operators,

$$\mathcal{S} = \hat{\sigma} - \partial_\xi \quad (7.125a)$$

$$\mathcal{P}^\pm = -\frac{n_P}{\hat{c}'_S}(1 + \partial_\xi - H\partial_\xi^2 + H\hat{k}^2) \quad (7.125b)$$

$$\mathcal{F}^\pm = -\hat{\varphi}'\partial_\xi \quad (7.125c)$$

$$\mathcal{L} = \partial_\xi^2 - \hat{k}^2 \quad (7.125d)$$

which allows us to shorten the notation. The  $\pm$  indexes indicate that different formulas for  $\hat{c}_S$  and  $\hat{\varphi}$  should be used for positive and negative  $\xi$ . Now Eqs. (7.108) with the appropriate

boundary and continuity conditions can be written as

$$\left(\frac{1}{W}\mathcal{L} + \mathcal{F}^\pm\right)\mathcal{P}^\pm\mathcal{S}f_{v_S}^\pm = \hat{k}^2\varrho^{-1}f_{v_S}^\pm, \quad \xi \geq 0 \quad (7.126a)$$

$$f_{v_S}^\pm|_{\xi \rightarrow \pm\infty} = 0 \quad (7.126b)$$

$$\mathcal{S}f_{v_S}^\pm|_{\xi \rightarrow \pm\infty} = 0 \quad (7.126c)$$

$$\mathcal{P}^\pm\mathcal{S}f_{v_S}^\pm|_{\xi \rightarrow \pm\infty} = 0 \quad (7.126d)$$

$$\partial_\xi\mathcal{P}^\pm\mathcal{S}f_{v_S}^\pm|_{\xi \rightarrow \pm\infty} = 0 \quad (7.126e)$$

$$e^{-W}\partial_\xi\mathcal{P}^-\mathcal{S}f_{v_S}^-(0) - \partial_\xi\mathcal{P}^+\mathcal{S}f_{v_S}^+(0) = \zeta_0\varrho^{-1}\hat{k}^2(e^{-W} - 1) \quad (7.126f)$$

$$\mathcal{P}^-\mathcal{S}f_{v_S}^-(0) - \mathcal{P}^+\mathcal{S}f_{v_S}^+(0) = 0 \quad (7.126g)$$

$$\mathcal{S}f_{v_S}^-(0) - \mathcal{S}f_{v_S}^+(0) = \zeta_0\varrho^{-1}H^{-1} \quad (7.126h)$$

$$f_{v_S}^-(0) - f_{v_S}^+(0) = 0, \quad (7.126i)$$

where we have used the fact that in the case of constant  $W$ , the near-front permeability ratio is

$$\frac{\hat{K}_+}{\hat{K}_-} = e^{-W}. \quad (7.127)$$

Once the problem (7.126) is solved, the dispersion relation can be found via Eq. (7.124),

$$\hat{\sigma} = -\Gamma_3 + \frac{1}{H} \int_{-\infty}^0 d\xi \exp(\Gamma_3^*\xi)\varrho\mathcal{P}^-\mathcal{S}f_{v_S}^-. \quad (7.128)$$

Expanding the perturbation amplitude and the growth rate in the powers of the small parameter  $W$ ,

$$f_{v_S} = f_0 + Wf_1 + W^2f_2 + \dots \quad (7.129)$$

$$\hat{\sigma} = \hat{\sigma}_0 + W\hat{\sigma}_1 + W^2\hat{\sigma}_2 + \dots, \quad (7.130)$$

allows one to solve Eqs. (7.126) analytically up to an arbitrary precision. In zeroth order the problem to solve is

$$\mathcal{L}\mathcal{P}^\pm\mathcal{S}f_0^\pm = 0, \quad \xi \geq 0 \quad (7.131a)$$

$$f_0^\pm|_{\xi \rightarrow \pm\infty} = 0 \quad (7.131b)$$

$$\mathcal{S}_0f_0^\pm|_{\xi \rightarrow \pm\infty} = 0 \quad (7.131c)$$

$$\mathcal{P}^\pm\mathcal{S}_0f_0^\pm|_{\xi \rightarrow \pm\infty} = 0 \quad (7.131d)$$

$$\partial_\xi\mathcal{P}^\pm\mathcal{S}_0f_0^\pm|_{\xi \rightarrow \pm\infty} = 0 \quad (7.131e)$$

$$\partial_\xi\mathcal{P}^-\mathcal{S}_0f_0^-(0) - \partial_\xi\mathcal{P}^+\mathcal{S}_0f_0^+(0) = 0 \quad (7.131f)$$

$$\mathcal{P}^-\mathcal{S}_0f_0^-(0) - \mathcal{P}^+\mathcal{S}_0f_0^+(0) = 0 \quad (7.131g)$$

$$\mathcal{S}_0f_0^-(0) - \mathcal{S}_0f_0^+(0) = \zeta_0\varrho^{-1}H^{-1} \quad (7.131h)$$

$$f_0^-(0) - f_0^+(0) = 0, \quad (7.131i)$$

where  $\mathcal{S}_0 = \hat{\sigma}_0 - \partial_\xi$ . The solutions are

$$f_0^\pm = \frac{\zeta_0}{\varrho\sqrt{4H^2\hat{k}^2 + 4H + 1}} \exp\left(\mp\xi\frac{\sqrt{4H^2\hat{k}^2 + 4H + 1} \mp 1}{2H}\right). \quad (7.132)$$

Since  $\mathcal{P}^- \mathcal{S}_0 f_0^- = 0$ , the leading (zeroth order) term in the dispersion relation is

$$\hat{\sigma}_0 = -\Gamma_3 = -\frac{\sqrt{1 + 4H^2 \hat{k}^2} - 1}{2H}. \quad (7.133)$$

At first order, after some simplifications we have

$$\mathcal{L}\mathcal{P}^\pm \mathcal{S}_0 f_1^\pm = \hat{k}^2 \varrho^{-1} f_0^\pm, \quad \xi \geq 0 \quad (7.134a)$$

$$f_1^\pm \Big|_{\xi \rightarrow \pm\infty} = 0 \quad (7.134b)$$

$$\mathcal{S}_0 f_1^\pm \Big|_{\xi \rightarrow \pm\infty} = 0 \quad (7.134c)$$

$$\mathcal{P}^\pm \mathcal{S}_0 f_1^\pm \Big|_{\xi \rightarrow \pm\infty} = 0 \quad (7.134d)$$

$$\partial_\xi \mathcal{P}^\pm \mathcal{S}_0 f_1^\pm \Big|_{\xi \rightarrow \pm\infty} = 0 \quad (7.134e)$$

$$\partial_\xi \mathcal{P}^- \mathcal{S}_0 f_1^-(0) - \partial_\xi \mathcal{P}^+ \mathcal{S}_0 f_1^+(0) = \zeta_0 \hat{k}^2 \varrho^{-1} \quad (7.134f)$$

$$\mathcal{P}^- \mathcal{S}_0 f_1^-(0) - \mathcal{P}^+ \mathcal{S}_0 f_1^+(0) = 0 \quad (7.134g)$$

$$\mathcal{S}_0 f_1^-(0) - \mathcal{S}_0 f_1^+(0) = 0 \quad (7.134h)$$

$$f_1^-(0) - f_1^+(0) = 0. \quad (7.134i)$$

In fact, since we are going to evaluate  $\hat{\sigma}$  only up to the first order, Eqs. (7.134) can be replaced by a simpler problem for  $g_1^\pm = \varrho \mathcal{P}^\pm \mathcal{S}_0 f_1^\pm$ . In fact,  $g_1^\pm$  is the first-order term in the expansion of the Darcy velocity perturbation amplitude,  $f_{u_\xi}^\pm = \varrho \mathcal{P}^\pm \mathcal{S} f_{v_S}^\pm$ , in  $W$  (the zeroth order is equal to zero,  $g_0^\pm = 0$ ). Such a simplification yields

$$\mathcal{L}g_1^\pm = \hat{k}^2 f_0^\pm, \quad \xi \geq 0 \quad (7.135a)$$

$$g_1^\pm \Big|_{\xi \rightarrow \pm\infty} = 0 \quad (7.135b)$$

$$\partial_\xi g_1^\pm \Big|_{\xi \rightarrow \pm\infty} = 0 \quad (7.135c)$$

$$\partial_\xi g_1^-(0) - \partial_\xi g_1^+(0) = \zeta_0 \hat{k}^2 \quad (7.135d)$$

$$g_1^-(0) - g_1^+(0) = 0. \quad (7.135e)$$

The upstream solution is

$$g_1^- = \frac{\hat{k} \left( (\hat{k} + 1)^{-1} (\hat{k} \varrho + \varrho - 1) \left( \Gamma_4^* + 2H \left( \Gamma_4^* + \hat{k}^2 \right) + 1 \right) e^{\hat{k}\xi} + 2H \hat{k} e^{\Gamma_4^* \xi} \right)}{2\varrho(\Gamma_4^* + 1)(2\Gamma_4^* H - 1)}, \quad (7.136)$$

where  $\Gamma_4^* = \frac{\sqrt{1 + 4H + 4H^2 \hat{k}^2} + 1}{2H}$ , and can be used via Eq. (7.124) to obtain the first-order term in the growth rate expansion,

$$\begin{aligned} \hat{\sigma}_1 &= \frac{1}{H} \int_{-\infty}^0 d\xi \exp(\Gamma_3^* \xi) g_1^-(\xi) = \\ &= \hat{k} \frac{\hat{k} \varrho + \varrho - 1}{H} + \frac{2 \left( (\hat{k} + 1) \varrho (\Gamma_3^* + \Gamma_4^*) \left( \Gamma_4^* + \hat{k}^2 \right) + (\hat{k} - \Gamma_4^*) \left( \Gamma_3^* + \Gamma_4^* + \hat{k}^2 + \hat{k} \right) \right)}{2\varrho(\hat{k} + 1)(2\Gamma_4^* H - 1)(\Gamma_3^* + \hat{k})}. \end{aligned} \quad (7.137)$$

Combining the two terms of the expansion, we eventually obtain

$$\begin{aligned} \hat{\sigma}(\hat{k}; H, \Lambda \rightarrow \infty, W, \varrho) &\approx -\frac{\sqrt{1 + 4H^2\hat{k}^2} - 1}{2H} \\ &+ W\hat{k} \frac{\frac{\hat{k}\varrho + \varrho - 1}{H} + \frac{2\left((\hat{k} + 1)\varrho(\Gamma_3^* + \Gamma_4^*)\left(\Gamma_4^* + \hat{k}^2\right) + (\hat{k} - \Gamma_4^*)\left(\Gamma_3^* + \Gamma_4^* + \hat{k}^2 + \hat{k}\right)\right)}{(\Gamma_4^* + 1)(\Gamma_3^* + \Gamma_4^*)}}{2\varrho(\hat{k} + 1)(2\Gamma_4^*H - 1)(\Gamma_3^* + \hat{k})}. \end{aligned} \quad (7.138)$$

Not surprisingly, taking the limit  $H \rightarrow 0$  in Eq. (7.138) is equivalent to taking  $\Lambda \rightarrow \infty$  of Eq. (7.95), and yields

$$\hat{\sigma}(\hat{k}; H \rightarrow 0, \Lambda \rightarrow \infty, W, \varrho) \approx W \frac{\hat{k}(\hat{k}\varrho + \varrho - 1)}{2(\hat{k} + 1)\varrho}. \quad (7.139)$$

### Discussion of the results

Similarly as in the limit of negligible dispersion (Eq. (7.68)), Eq. (7.124) does not have in general an analytical solution and have to be solved numerically. However, in case of the exponential permeability model, an approximate solution could be obtained for small  $W$ , Eq. (7.138).

To present the results, two different scalings are used. Spatial coordinates will be scaled either by  $l_S^d$  (Eq. (7.43)), which is the largest characteristic length for  $\Lambda > 1$  and  $H < 2$ , or by the diffusive length scale  $l_X^u$  (Eq. (7.40)). As the time scale we choose the one associated with the respective length scale, either  $l_S^d/U$ , or  $l_X^u/U$ , where  $U$  is the velocity of the planar front (Eq. (7.26)).

Similarly as in the case of  $H \rightarrow 0$ , perturbations of zero wavenumber are marginally stable,

$$\sigma(k = 0) = 0. \quad (7.140)$$

For small  $W$ , it can be shown that the stability of the front with respect to long-wave ( $\hat{k} \gtrsim 0$ ) perturbations depends on the far-field permeability contrast,

$$U^{-1} \left. \frac{d\sigma}{dk} \right|_{k=0} = W \frac{\varrho - 1}{2\varrho} \quad (7.141)$$

(cf. Eqs. (3.81–3.82) and (7.96–7.97)). For equal far-upstream and far-downstream porosities ( $\rho = 1$ ), we obtain  $\sigma'(k = 0) = 0$ , and one needs to study higher derivatives to assess the front stability. Taking the second derivative of the dispersion curve at  $\hat{k} = 0$  we obtain

$$\hat{\sigma}''(\hat{k} = 0) = -2H + W \frac{H(2\sqrt{4H+1} - 5) - 2}{(H-2)\sqrt{4H+1}}, \quad (7.142)$$

which reduces to Eq. (7.100) in the limit of  $H \rightarrow 0$ . It can be either positive or negative, depending on the interplay between the permeability gain factor  $W$  and the transport parameter  $H$ . For

$$W > W_{cr} = \frac{2(H-2)H\sqrt{4H+1}}{H(2\sqrt{4H+1} - 5) - 2} \approx 2H \quad (7.143)$$

long-wave perturbations are unstable. The analytical results are in agreement with numerical solutions (Figs. 7.10–7.6). Note that even for  $\varrho < 1$  and  $H > 0$ , there can be an intermediate range of wavelengths which are unstable. Again, this is fundamentally different from the one-component reactive-infiltration instability.

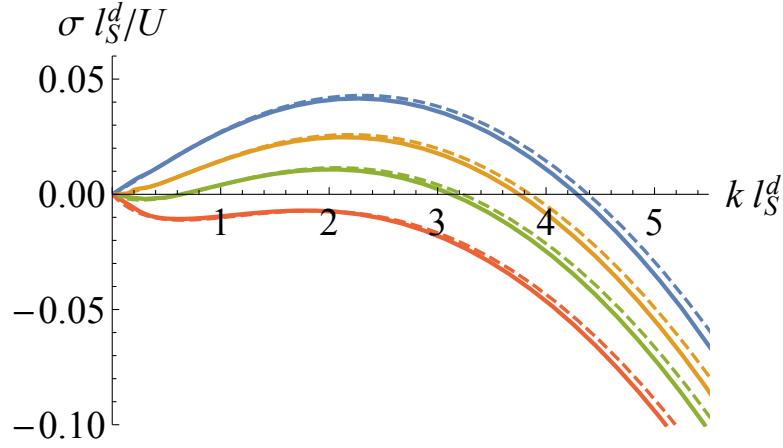


Figure 7.10: Dispersion curves for  $\Lambda \rightarrow \infty$ ,  $H = 0.01$ ,  $W = 0.1$ , and  $\varrho = 2, 1, 0.7, 0.5$  (top to bottom). The numerical solutions (solid lines) are practically indistinguishable from the small- $W$  approximate ones (dashed lines; Eq. (7.138)), especially in the small- $k$  part of the spectrum.

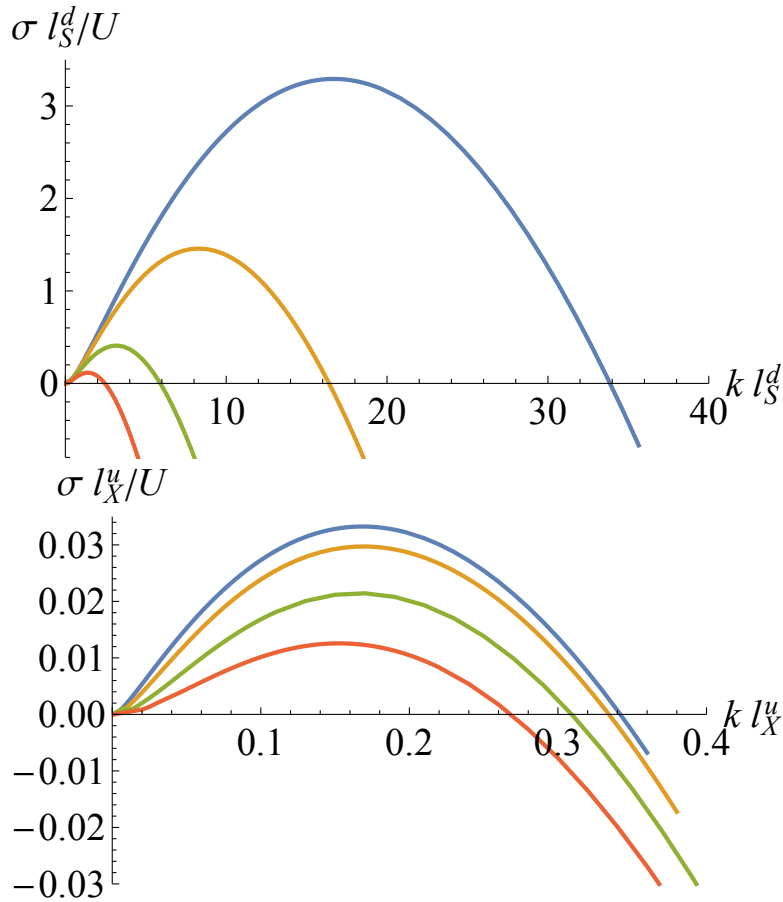


Figure 7.11: (Top) Dispersion curves for  $\Lambda \rightarrow \infty$ ,  $W = 1$ ,  $\varrho = 1$ , and  $H = 0.1, 0.05, 0.02, 0.01$  (top to bottom), obtained numerically. The curves collapse for  $k l_S^d \gtrsim 0$ . (Bottom) The same, but the upstream diffusive length  $l_X^u$  was used for scaling. The maxima of the curves are located at approximately the same place,  $k^* l_X^u \approx 0.16$ , or  $\lambda^* \approx 0.16 l_X^u / (2\pi)$ .

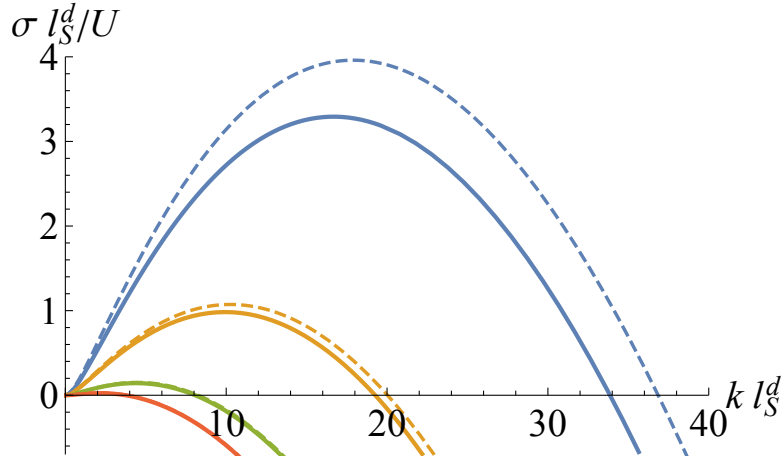


Figure 7.12: Dispersion curves for  $\Lambda \rightarrow \infty$ ,  $H = 0.01$ , and  $\varrho = 1$ , and  $W = 1, 0.5, 0.2, 0.1$  (top to bottom). The numerical solutions (solid lines) are accompanied by the small- $W$  approximate ones (dashed lines; Eq. (7.138)). Although the approximation was derived for  $W \ll 1$ , the approximate dispersion curve for  $W = 1$  is relatively close to the exact one.

It is the short-wave part of the spectrum which is mostly influenced by the value of  $H$ . As illustrated in Fig. 7.11 (top), the stronger dispersion (larger  $H$ ), the more stabilized are short-wave perturbations, while the long-wave spectrum remains intact while varying  $H$ . Also the maxima of the dispersion curves, which correspond to the fastest-growing modes, are shifted towards smaller  $k$  (longer waves) while increasing  $H$ . However, choosing a different length scale, the upstream diffusive one,  $l_X^u = D/u_0$ , causes a collapse of the maxima. A rough estimation of the most unstable mode is

$$k^* \approx 0.16 \frac{u_0}{D}, \quad \lambda^* \approx \frac{0.16 D}{2\pi u_0}. \quad (7.144)$$

The result, obtained in the quick dissolution limit, is similar to the one for a simple dissolution front (also in the quick dissolution, or thin front, limit), Eq. (3.91). The upper limit on the growth rate of short-wave perturbations can be found by studying dispersion curves in the  $H \rightarrow 0$  limit.

Despite certain similarities with the reactive-infiltration instability, the current system of interest has a richer family of parameters and factors which influence the character of the instability. One of them, which was not present in the analysis conducted in Chapter 3, is the relationship between the porosity and the permeability. From the point of view of linear stability, it is the permeability gain factor  $W$  (constant for the exponential permeability model), which characterizes the relative permeability gain for the given porosity increase. As expected, the instability is stronger for larger  $W$ . Both the range of unstable wavelengths and the maximal growth rate increase with  $W$  (Fig. 7.12).

## 7.5 Analogy to multilayer viscous fingering

In our hydrogeochemical models instability of a planar front is caused by positive feedbacks between the flow and permeability. Somewhat similar systems have been considered in the context of viscous fingering [80, 81, 82, 83]: a thin slice of fluid of viscosity  $\mu_2$  inserted in the fluid of viscosity  $\mu_1$  in a Hele-Shaw cell and subject to the pressure gradient. Here, feedbacks between the fluid flow and viscosity destabilize the front. There is no contrast of mobility in the far-field, and yet the system turns out to be unstable. Such a case is analogous to ours, for  $\rho = 1$ . This instability is interpreted by noting that out of the two interfaces between

the injected fluid and the bulk fluid, one is always unstable. When a more viscous solution is injected into a phase of lower viscosity, the rear interface of the injected slice becomes unstable while the frontal one is stable. Conversely, when a low viscosity sample plug is injected into a higher viscosity mobile phase then the viscous fingers develop at the frontal interface of the sample while the rear interface remains stable [80]. These conclusions have been subsequently verified experimentally in the studies [84] and [85].

Nevertheless, although the instability in our hydrogeochemical system is conceptually similar to the instability in a moving heterogeneous fluid with a nonmonotonic viscosity profile, caution should be taken while comparing these systems. In our case it is dispersion which stabilizes short-wave perturbations of the front, while for viscous fluids it is either diffusion (for miscible fluids) or surface tension (for immiscible fluids). In fact, as shown by [82], the characteristic width of the unstable wavenumber bandwidth, as well as the characteristic instability growth rate, are rather controlled by surface tension, and not by the width of the middle, more viscous layer. In our replacement system, the characteristic wavelength of the perturbation is comparable with the width of the longest length scale characterizing a planar front ( $l_S^d$  or  $l_X^u$ ). In the viscous fluid case, the width of the middle slice of fluid,  $L_m$ , has weak impact on the dynamics [82]. Here, the characteristic wavelength is a function of the viscosity jump at the interface, the fluid displacement velocity and the surface tension, similar to the Saffman-Taylor instability. In fact, the Saffman-Taylor instability is observed both in the limit  $L_m \rightarrow 0$  (with the effective surface tension equal to the sum of the two original ones) and  $L_m \rightarrow \infty$  (where the two fluid-fluid interfaces evolve separately)



# Chapter 8

## Nonlinear evolution of the replacement system

### 8.1 Numerical simulations

In Chapter 7 we have shown that dissolution-precipitation fronts are unstable for a broad range of control parameters ( $\varrho$ ,  $H$ ,  $\Lambda$ ). In the presence of noise, a planar replacement front breaks up and protrusions begin to grow. Subsequent stages of the evolution can be studied by numerical simulations, similarly as presented in Chapter 5 for a one-component dissolution system. All the simulations presented in this chapter were performed by solving a discretized version of Eqs. (7.18) on a  $1024 \times 1024$  rectangular grid, the lattice constant of which corresponds to  $0.1 L$  (see Eq. (7.11) for the length scale  $L$ ), or  $0.06 l_S^d$ . The direction of the externally imposed pressure gradient is from the top to the bottom. On the side walls, periodic boundary conditions were applied. The precipitation reaction of the form (7.45) was used to prevent the system from complete clogging. The initial state of the simulations was the stationary solution (7.39) perturbed with an uncorrelated Gaussian noise of zero mean and standard deviation equal to  $10^{-2} v_P^{max}$ .

In case of  $\rho > 1$  (permeability of the secondary phase higher than permeability of the primary phase), evolution of the replacement system is similar to the one-component dissolution (Fig. 5.1). Figs. 8.1–8.2 present the evolution of the dissolution-precipitation system for  $\varrho = 1.8$ . Soon the translational symmetry becomes broken and small protrusions spontaneously develop in the front. The protrusions grow and transform into small fingers. Due to competition for the available flow and solvent flux, the dynamics becomes nonlinear, dominated by screening and merging of the fingers. As a result, the fingers grow and coarsen, and their number decreases. The overall picture is very similar to the one observed for pure dissolution. Two morphological distinctions can be, however, noted. Firstly, the continuous region of decreased porosity in the vicinity of the reaction front persists in the nonlinear regime. Its presence affects the shape of the fingers, which are rather funnel-like than parabolic. Secondly, the secondary mineral is not evenly distributed far upstream. Instead, its distribution reflects the history of the sample. Indeed, paths of decreased  $v_S$  content (and increased porosity) can be distinguished at symmetry axes of individual fingers. They are traces of the trajectories of their tips.

In Chapter 7 it was proved that replacement fronts with  $\varrho < 1$  can be also unstable, which is a fundamentally different behaviour than that observed for one-component systems. The instability is caused by the nonmonotonicity of the steady-state porosity profile. Figs. 8.3–8.4 present the evolution of the replacement system for  $\varrho = 0.9$ . Indeed, the front breaks up spontaneously and small protrusions develop. However, the further evolution is markedly different from the case with  $\varrho > 1$ . Long, separate fingers do not develop. Instead, a wavy front begins to propagate. At the same time, the protrusions which have developed slowly coarsen.

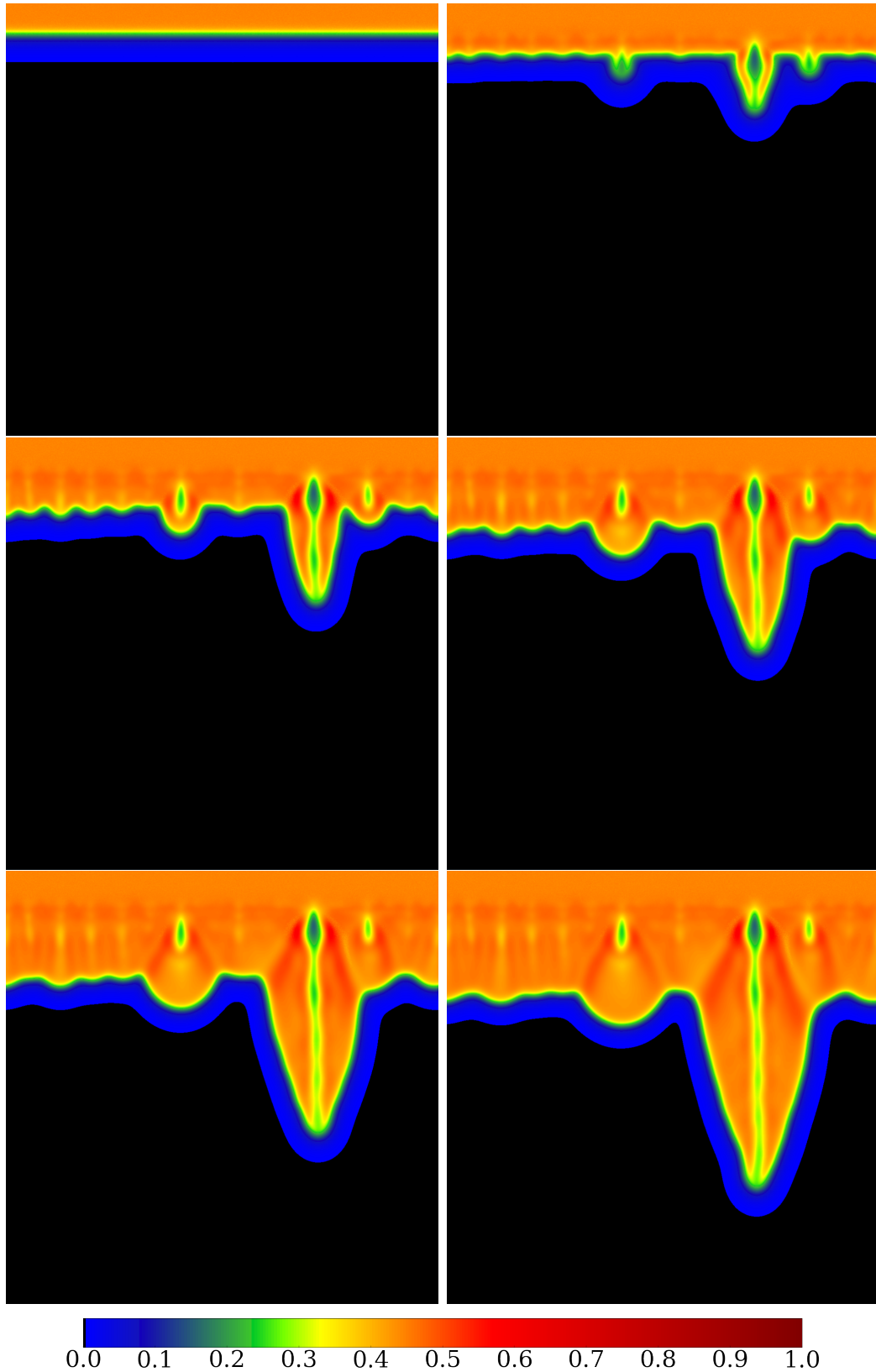


Figure 8.1: Nonlinear evolution of the replacement system, for  $n_{S,X,P} = 1$ ,  $\varrho = 1$ ,  $H = 1$ ,  $\Lambda = 10$ , and  $v_P^{max} = 0.8$ . The secondary mineral volume fraction  $v_S$  is presented. Subsequent stages of the evolution are shown:  $t/(T/v_P^{max}) = 0, 5, 10, 15, 20, 25$  (left to right and top to bottom).

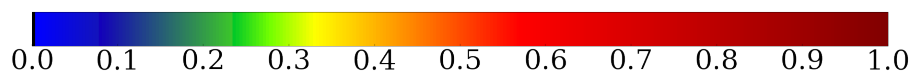
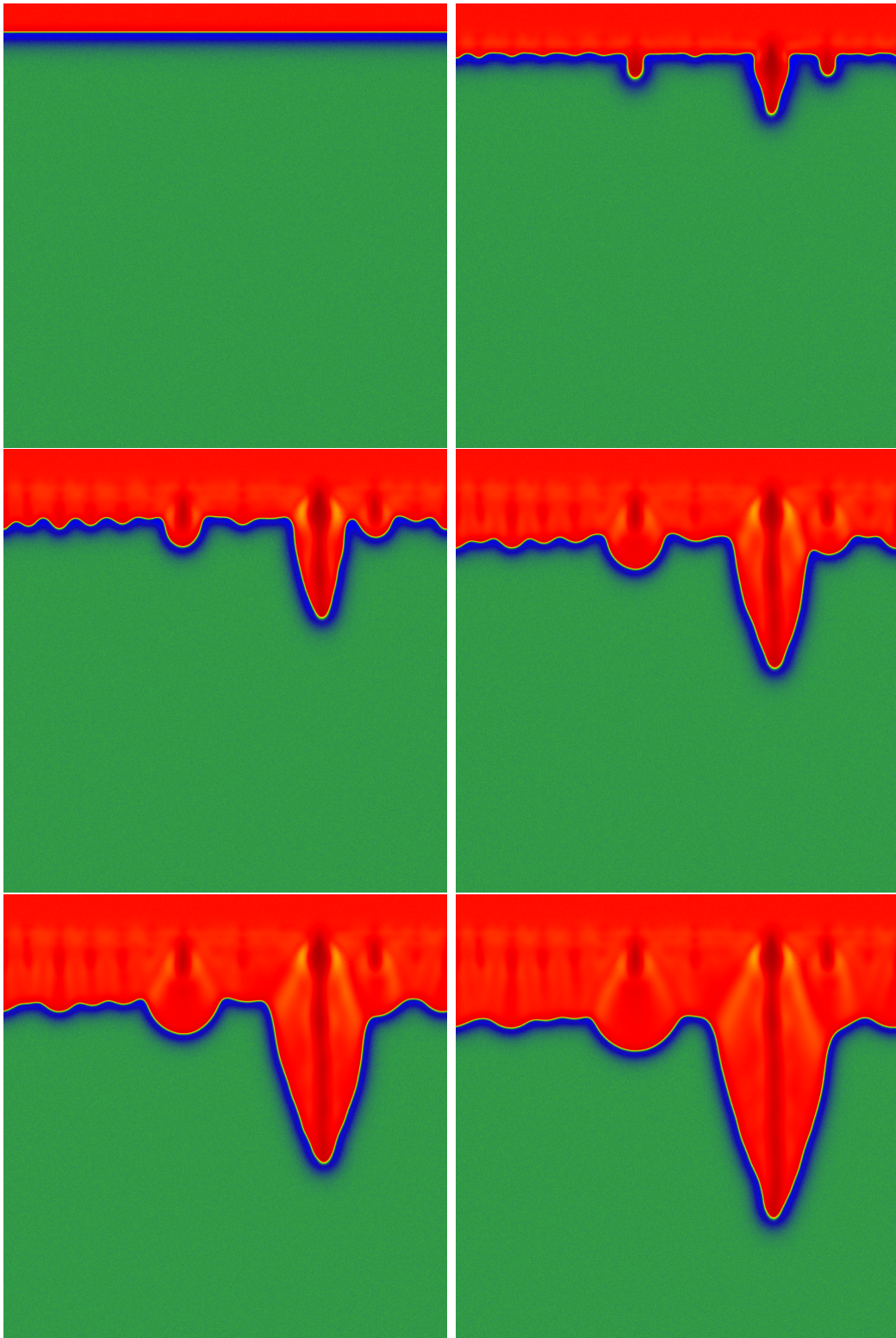


Figure 8.2: The same as in Fig. 8.1, but porosity  $\varphi$  is plotted.

Similarly as in the  $\varrho > 1$  case, the replacement zone is characterized by a porosity decrease, and paths of higher porosity remain in the secondary rock after the front has moved.

Lastly, let us consider the marginal case of  $\rho = 1$ . Here, the system dynamics is probably the most intriguing one. The steady front is unstable and its breakup leads to the development of an array of small protrusions, which grow into fingers. Soon one of them acquires a significant part of the total solvent flux and outgrows its neighbours. However, increased dissolution of the primary mineral is associated with the increased precipitation of the secondary one. The precipitate forms a weakly permeable wall near the tip of the fastest-growing finger, and its growth ceases. Then the fluid finds another dominant flow path, where the next fastest-growing finger develops, and the process continues in a sort of a loop. Consequently, a chaotic network of fingers is created. The body of each finger is more porous than its sides. The increased permeability of the finger network is neutralized by a “halo” of low permeability, surrounding all the fingers.

## 8.2 Comparison with natural patterns

As noted in the beginning of Chapter 7, dolomitization is a common mineral replacement process. It occurs when a calcite rock is infiltrated by a magnesium-rich brine. Calcium carbonate is then replaced by calcium magnesium carbonate,  $\text{Ca}_{1-x}\text{Mg}_x\text{CO}_3$ , which crystallizes as dolomite.

Calcium-to-dolomite replacement was studied by Sharp et al. [86], who were doing field observations in Zagros Mountains, Iran. Fig. 8.7 presents one of the outcrops. The boundary between the calcite and the dolomite is wavy and replacement fingers, filled with dolomite, are clearly seen. The size of the fingers is of the order of 10 m in length and width. It is much larger than the width of the replacement front, which cannot be deduced from the figure. The authors do not report any quantitative porosity or permeability measurements, but they note that some porosity was generated in course of the replacement. It agrees with our notion that large-scale fingers develop in porosity-generating ( $\varrho > 1$ ) replacement systems. Moreover, Sharp et al. observe porosity enhancement near the axes of some dolomite fingers: “Note visible vuggy porosity development in centre of dolomite body, and lack of porosity in adjacent limestone country rock” (Fig. 8.8). Obviously, this porosity could have been created in a number of possible scenarios. However, our results presented in Sec. 8.1 suggest that a similar porosity redistribution can be achieved solely as a consequence of nonlinear feedbacks between the chemical reactions, porous matrix evolution, and the fluid flow. Our findings thus give a simple and elegant explanation to the phenomenon reported in Ref. [86].

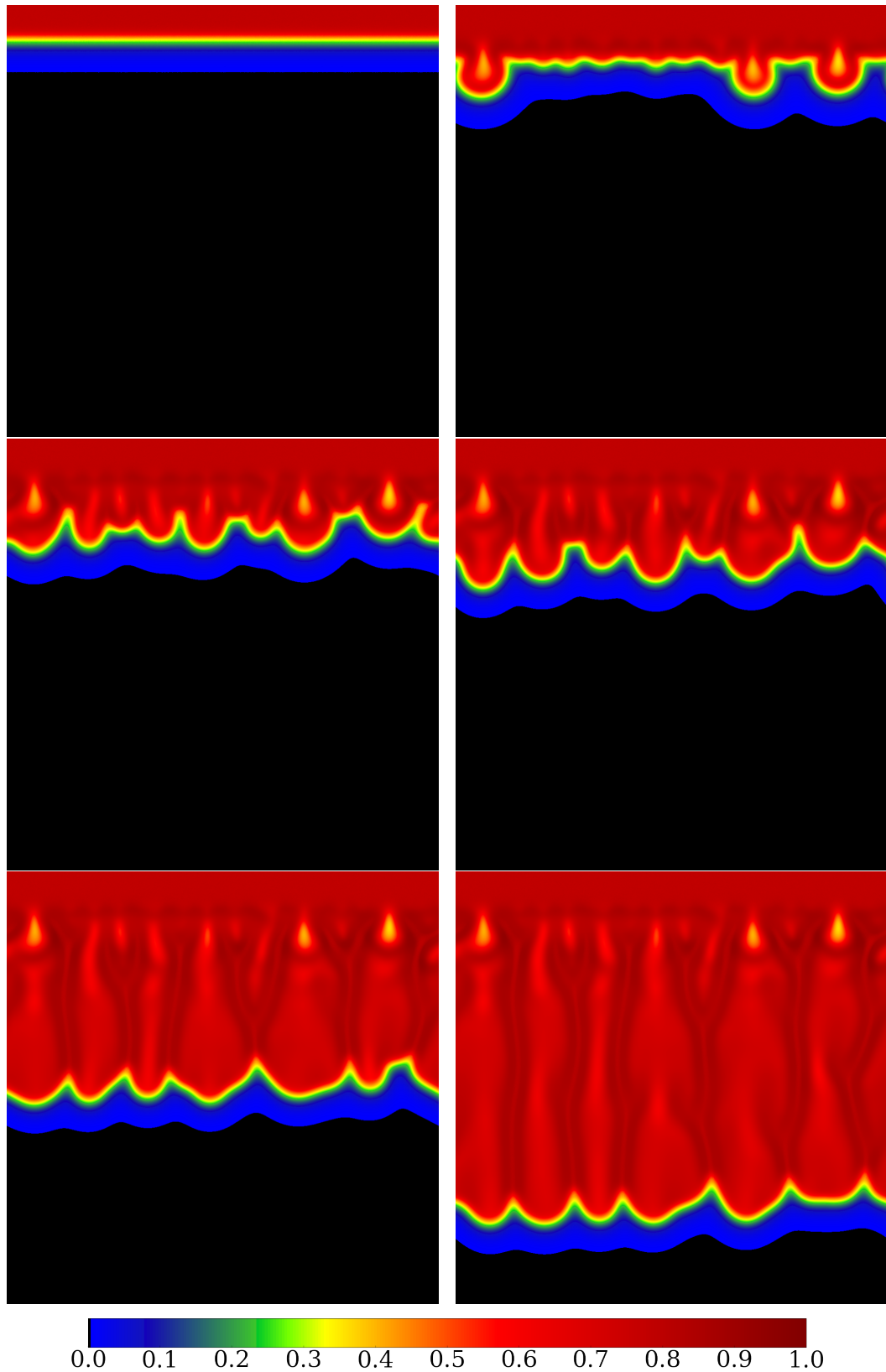


Figure 8.3: Nonlinear evolution of the replacement system, for  $n_{S,X,P} = 1$ ,  $\varrho = 0.9$ ,  $H = 1$ ,  $\Lambda = 2$ , and  $v_P^{max} = 0.7$ . The secondary mineral volume fraction  $v_S$  is presented. Subsequent stages of the evolution are shown:  $t/(T/v_P^{max}) = 0, 5, 10, 15, 30, 50$  (left to right and top to bottom).

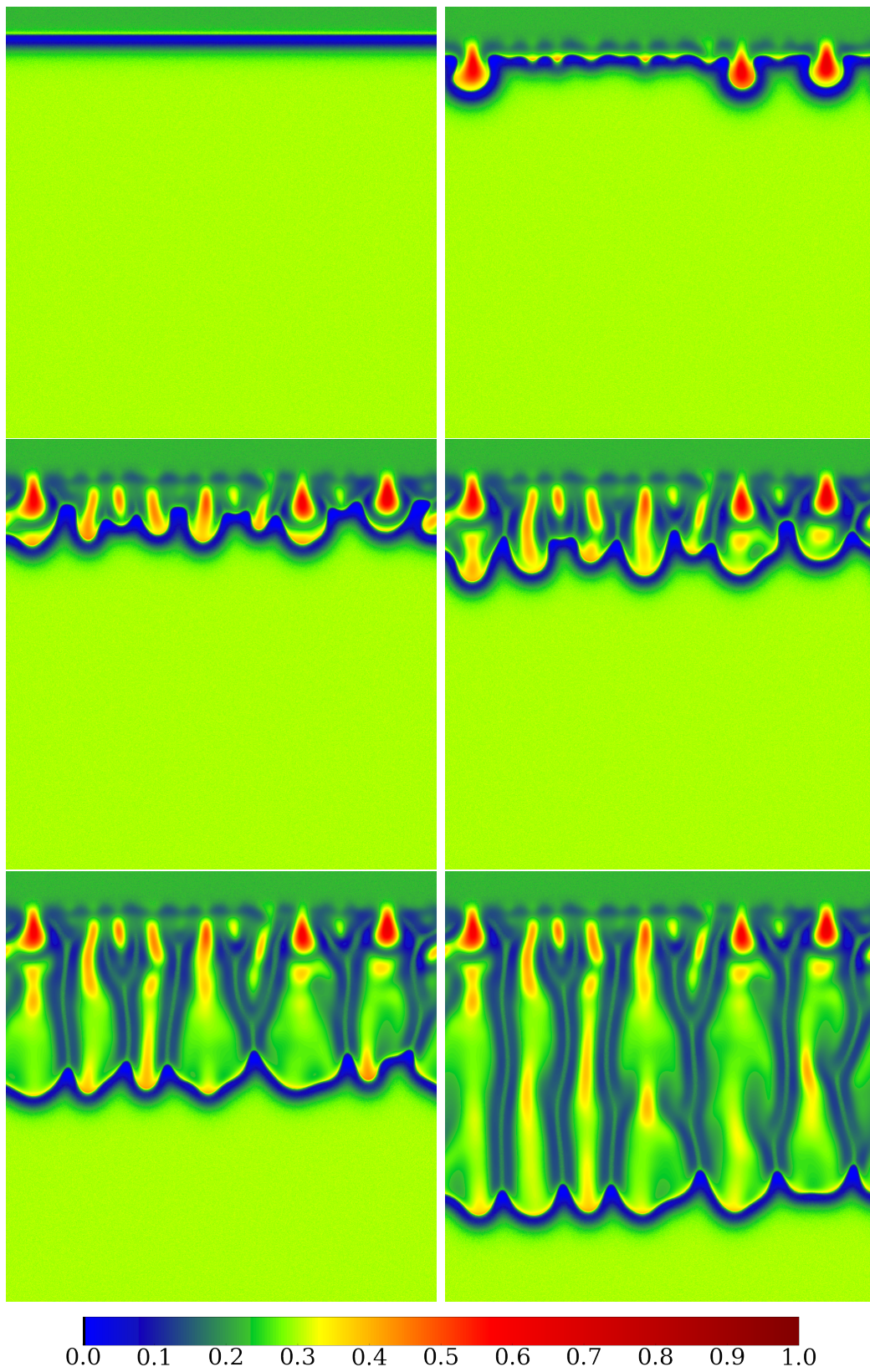


Figure 8.4: The same as in Fig. 8.3, but porosity  $\varphi$  is plotted.

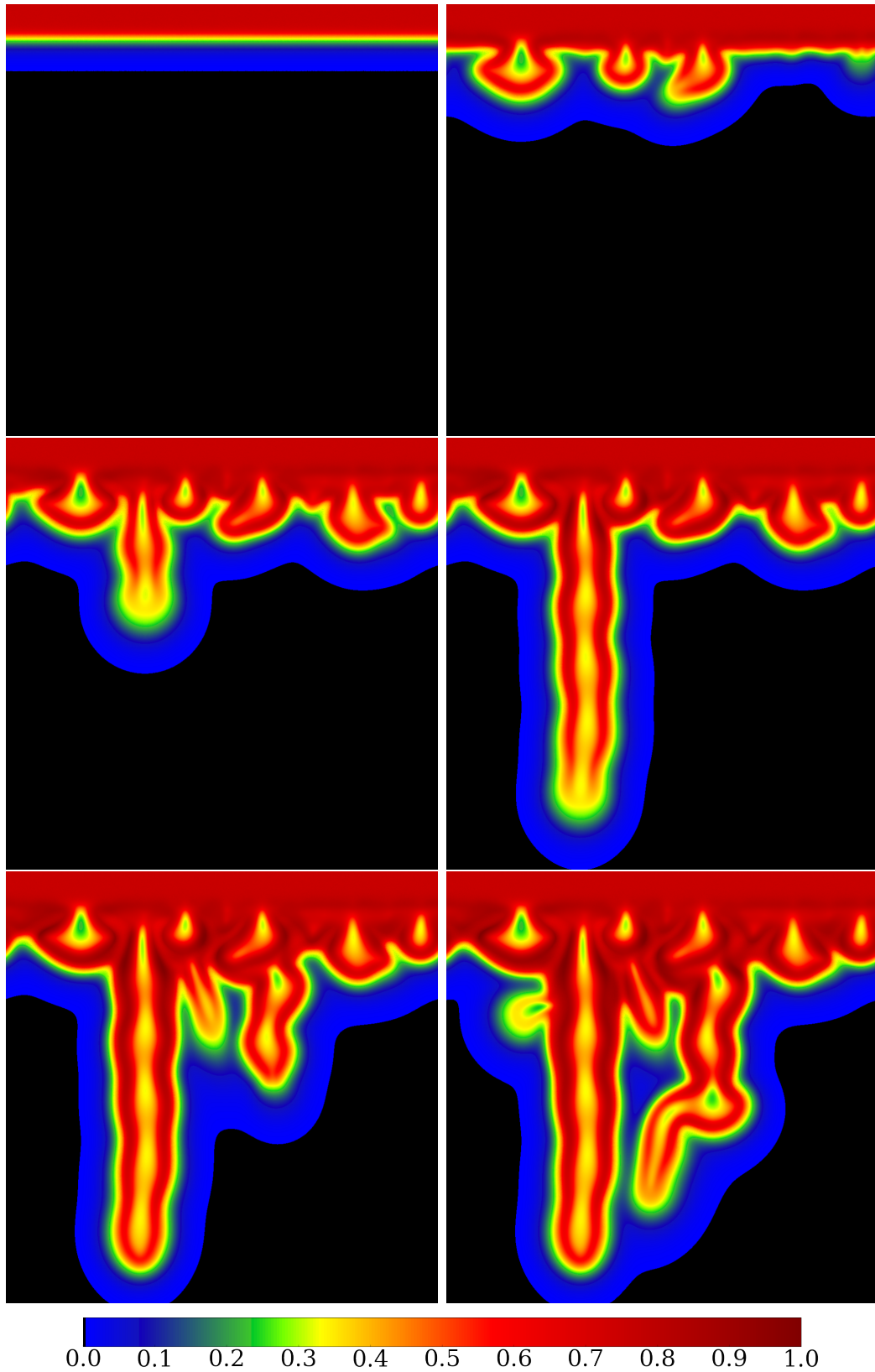
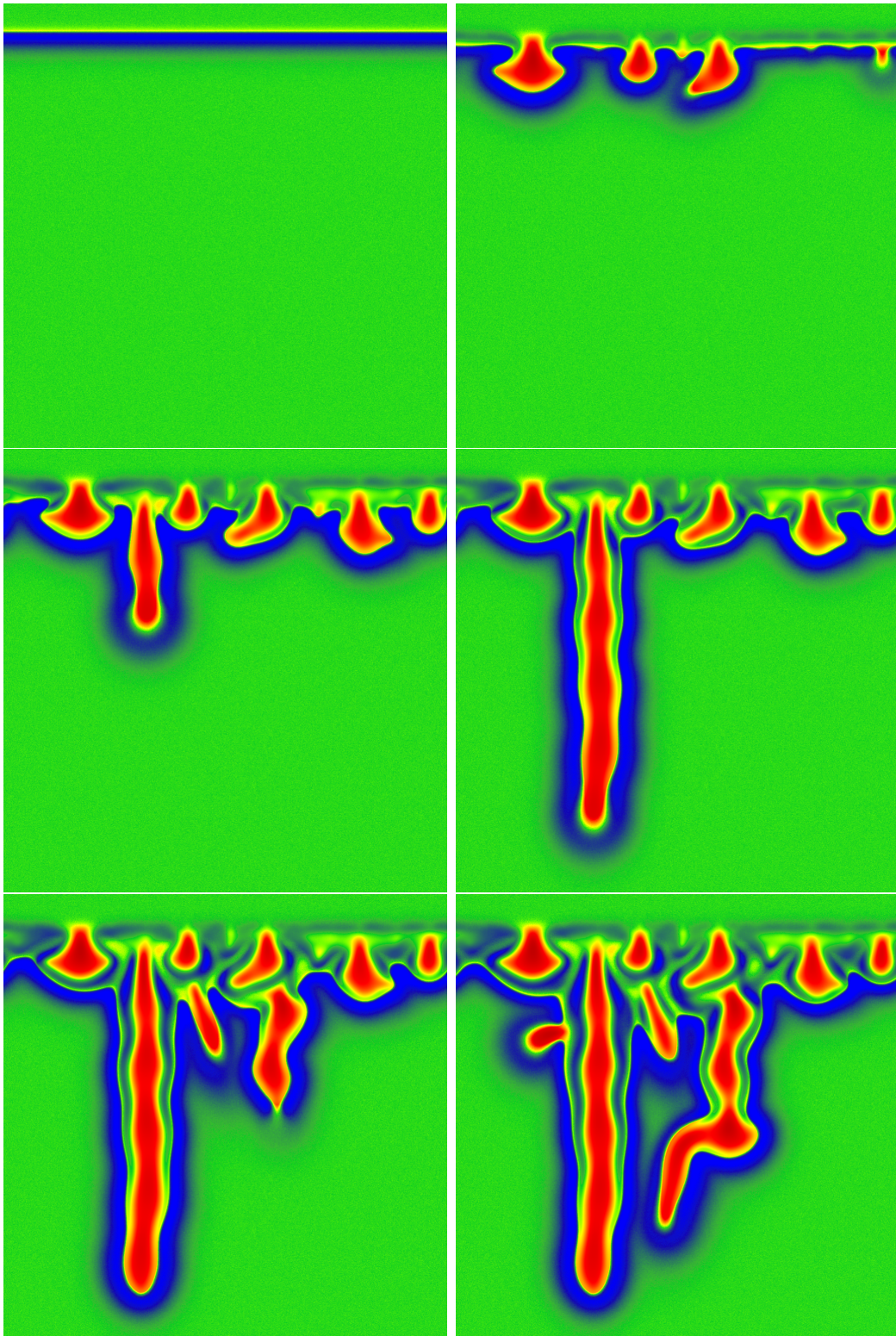


Figure 8.5: Nonlinear evolution of the replacement system, for  $n_{S,X,P} = 1$ ,  $\varrho = 1$ ,  $H = 1$ ,  $\Lambda = 2$ , and  $v_P^{max} = 0.75$ . The secondary mineral volume fraction  $v_S$  is presented. Subsequent stages of the evolution are shown:  $t/(T/v_P^{max}) = 0, 5, 10, 15, 20, 25$  (left to right and top to bottom).



0.0 0.1 0.2 0.3 0.4 0.5 0.6 0.7 0.8 0.9 1.0

Figure 8.6: The same as in Fig. 8.5, but porosity  $\varphi$  is plotted.

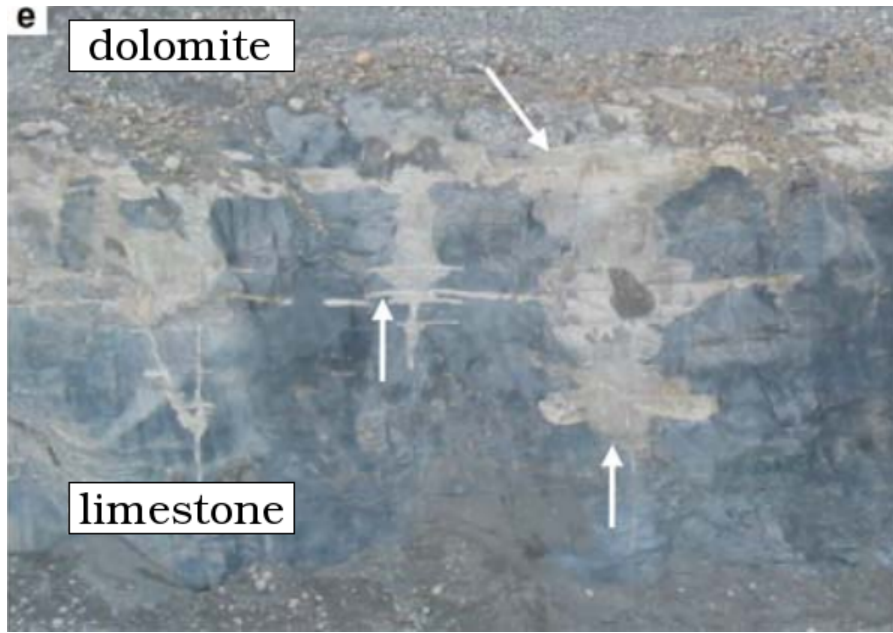


Figure 8.7: An outcrop figure modified from [86]. The width of the outcrop is approximately 100 m. The lengths of the dolomite fingers range from a few meters to about 25 m.



Figure 8.8: A dolomite finger figure adapted from [86]. The finger is marked with the white dashed line. The axis of the finger is clearly more porous than both the rest of the dolomite and the surrounding limestone.



# Chapter 9

## Summary

Nonlinear couplings between individual processes in nature often lead to spontaneous pattern formation. Patterns formed in the lithosphere are in many respects exceptional, since, once created, they can persist for millions of years, even if the original forces which brought them to existence are no longer active. The analysis of these patterns can provide valuable information about the environment in which they were formed.

In the present thesis specific pattern formation mechanisms were studied, which arise from positive feedbacks between the fluid flow through a porous medium, transport of reactive aqueous species in the flow, and chemical reactions which modify the rock.

As specified in Chapter 2, we are interested in length scales which are significantly larger than typical pore sizes in the rock, and time scales which are connected with changes in the porous matrix, via dissolution or precipitation of minerals. Therefore continuum models are adapted in our analysis, and Darcy's law is applied to account for the fluid flow.

In Chapter 3 we rederived some classic results of the reactive-infiltration instability, performing linear stability analysis of a planar dissolution front. We have adopted the thin-front approximation, in which the reaction is assumed to take place instantaneously with the reactants fully consumed at the dissolution front. In this way the problem becomes Stefan-like with the undissolved phase downstream and the fully dissolved phase upstream. We have shown that such a dissolution front is always unstable with respect to long-wavelength perturbations to the front position. Short-wavelength perturbations can be stabilized by dispersion. The results are well known, so their rederivation (in our notation) served just as a starting point for our own results.

Next, in Chapter 4 we analyzed the dissolution system from Chapter 3 in a weakly nonlinear regime. We applied a simplified approach and studied only the coupling between the harmonic mode which dominates in the linear regime, and its first subharmonic (i.e. twice the wavelength). Such an approach had proved to be successful in case of a simpler model of Laplacian growth [46]. The analysis allowed us to observe the first nonlinear effects which emerge during a spontaneous front breakup, namely the competition between individual protrusions, which results in screening of the shorter ones by the longer. In fact, the overall form of the equations (4.8), which govern the mode coupling in the weakly nonlinear regime, is analogous to the models of Laplacian growth.

As it has already become clear in Chapter 4, even for simplest hydrogeochemical systems only limited results can be obtained using solely analytical methods. Therefore in Chapter 5 a complementary approach was used: the dynamics of the system was studied using numerical simulations. Paying the price of strictness and generality, full evolution of the nonlinear system could be tracked. Numerical simulations are in agreement with analytical results in the first stages of the evolution. Next, they allow one to observe two phenomena, which play the major role during the later stages of the evolution: merging and screening of individual

dissolution fingers. As a result, an array of fingers develops, which resemble the ones observed in nature (Fig. 1.4).

In Chapter 6 we have been analyzing the geometry of dissolution forms, which are commonly found in soluble rocks. These are either convex forms, dubbed dissolution fingers (Sec. 6.1), or concave ones, roots (Sec. 6.2). We assumed that both forms approach a stationary shape in course of the evolution. In the thin-front limit we were investigating the problem of the existence and shape of steadily growing dissolution forms. Two potentially limiting assumptions have been made. First, we have adopted the Ivantsov ansatz (6.11), which has been successfully used in other studies of dendritic growth [59, 87, 60], usually leading to the parabolic forms of advancing dendrites. Moreover, we have assumed that the transformation  $(x, y) \rightarrow (\chi, \psi)$  from the original Cartesian coordinates to the coordinates spanned by the isolines and gradient lines of the reactant concentration field  $c$  is conformal. Both of these assumptions limit the class of solutions that can be found with this technique, leading however to significant simplifications in the analysis, since the Ivantsov equation (6.14) is conformally invariant and takes a particularly simple form (6.15) in the new coordinate system, where  $c = c(\chi)$ . The analysis of these equations leads to the conclusion that  $(\chi, \psi)$  are parabolic coordinates. Consequently, for both fingers and roots, we obtained a family of infinite forms, which are either parabolic (in two dimensions) or paraboloidal (in three dimensions). The flow within the finger, as well as within the root, turns out to be uniform, in agreement with the earlier studies on the refraction of groundwater flow on parabolic inclusions [69]. The magnitude of the flow is a function of the permeability ratio between the dissolved and undissolved matrix,  $\kappa$ . The concentration field can be expressed in terms of special functions (e.g. the imaginary error function for two-dimensional fingers, Eq. (6.40)). In case of the fingers, the parameter controlling the shape of the field lines is  $Pe'$ , defined as the ratio of convective to diffusive fluxes within the finger on the length scale of the radius of curvature of its tip. For the roots, the distribution of the solvent concentration is a function of both the Péclet number and the permeability contrast.

However, these simplifications come at a price, as we can only impose concentration boundary conditions on the lines of constant  $\chi$ , which limits the usefulness of these solutions. In regard to the fingers, the most relevant physically seems to be the case of large Péclet numbers, since in that case the concentration within the finger becomes uniform with an exception of a thin boundary layer near the reaction front itself. In this case the exact placement of the Dirichlet boundaries becomes irrelevant. In fact, the solution pipes shown in Fig. 1.4 seem to have been formed under such a regime. In case of the roots, the limitations on imposing the boundary conditions for the concentration are less important, since the inlet concentration can be imposed on a parabola which is infinitely far from the root.

The propagation velocity of both fingers and roots,  $U$ , is proportional to the acid capacity number, and the flow rate. In general, it also depends on the radius of curvature of the tip,  $\rho$ , and the permeability contrast between the dissolved and undissolved domains,  $\kappa$ . However, in the advection-dominated regime (large Péclet numbers) the propagation velocity of both forms is independent of the curvature,

$$U = \gamma u_{in}, \quad (9.1)$$

where  $u_{in}$  is the Darcy velocity of the fluid either inside the finger or the root. For small Péclet numbers, the propagation velocity is an increasing function of the tip curvature:  $U \propto \rho^{-1}$  for 2D and 3D fingers,  $U \propto \rho^{-1/2}$  for 2D roots, and  $U \propto (\rho \ln \rho)^{-1}$  for 3D roots.

The scale invariance of the problem leads to a dynamical indeterminacy. Any propagation velocity is permissible provided that the radius of curvature of the finger (root) is appropriately tuned. There is no selection principle to fix the tip curvature and the finger (root) propagation velocity independently. Finding such a selection principle is a highly nontrivial task [88] and involves the introduction of an additional length scale into the system. In the case of viscous fingering and dendritic growth this is achieved through short-scale regularization mechanisms

such as surface tension or kinetic undercooling. It is not clear what would be the physical origin of such a short-scale regularization in the present case. A candidate for the additional length scale could be the reaction front width, which in our analysis is zero, but remains finite in any physical case. Another possibility is that the additional length scale sought here is connected with the presence of other fingers, as it is always the case in natural systems (cf. Fig. 1.4). The full solution of the problem would then require matching the solution near the parabolic tip with that in the neighborhood of the root of the finger, where it joins with its companion.

Up to Chapter 6, single-component dissolution systems were studied. In Chapter 7 we studied more complicated systems, where dissolution of a primary mineral in the rock is accompanied by precipitation of a secondary one. After considering one-dimensional profiles of mineral volume fractions and concentrations, the linear stability of such solutions was analyzed. We have shown that replacement fronts, whose characteristic feature is a porosity (and permeability) decrease in the replacement zone, can be unstable for a wide range of parameters. The most striking observation is a possible destabilization of the front in the case when permeability of the secondary rock far upstream is lower than permeability of the primary rock far downstream ( $\varrho < 1$  in our notation). Such a destabilization of the front is caused by the presence of a zone of lower permeability in the vicinity of the replacement zone. In our analysis we were assuming very simple, linear chemical kinetics models. Although geological systems are characterized by a more complex chemical kinetics than that considered here, the qualitative features of the dispersion curves should remain the same, provided that a low-porosity zone is present.

Chapter 8 plays a similar role as Chapter 5. Here, we present numerical studies of the replacement system introduced in Chapter 7. Replacement systems with  $\varrho > 1$  behave similarly to dissolution systems. The initial instability causes the front breakup and the emergence of an array of protrusions. Due to nonlinear feedbacks, in course of the evolution some of the protrusions coarsen and grow into fingers, while others get screened and absorbed by their larger neighbours. However, there are some dissimilarities between the replacement and the dissolution systems. Firstly, in the replacement system the intermediate region between the primary and the secondary phases is characterized by a porosity decrease. Secondly, the secondary mineral is not evenly distributed. Instead, its volume fraction distribution reflects the history of the system. Paths of increased porosity in the secondary phase coincide with the former positions of finger tips. Interestingly, similar effects can be observed in some natural replacement systems, in particular during calcite-to-dolomite replacement. The case of  $\varrho < 1$  is also linearly unstable for a wide range of other parameters. After the initial breakup period, a wavy replacement front propagates through the porous rock and simultaneously reorganizes. However, large-scale fingers do not develop here. The distance between the leading and the trailing point at front remains approximately constant.

Obviously, the models presented in this thesis are just a few examples of possible scenarios of interactions and couplings observed in natural hydrogeochemical systems. For instance, the “driving force” of the replacement might not be dissolution, but precipitation [89]. Contrary to the replacement systems considered in this thesis, those are characterized by a porosity increase in the vicinity of the front. Such a class of replacement systems was studied by the author of this thesis in a similar manner [90]. Interestingly, they are also unstable for a broad range of control parameters, even if  $\varrho < 1$ .

The models which we have presented might seem seriously simplified when compared with natural phenomena. However, we believe that such a reductionistic approach can be still fruitful. With just a handful of parameters it is relatively easy to study the impact of each of them onto the behaviour of the system. On the other hand, as proved in this thesis, even apparently simple geophysical models might exhibit a broad class of nonintuitive, complex phenomena. Modeling is in fact a kind of art, since usually it is not straightforward to assess

which components of a modeled system are of fundamental importance, and which can be (in the desired approximation) omitted. We hope that our analysis of simple hydrogeochemical models has provided us with some insight into the Nature.

# Bibliography

- [1] N. Wetzler. *Examination of Kelvin-Helmholtz Instability as a Mechanism of Deformation in the Lisan Formation, Dead Sea Basin*. PhD thesis, Tel Aviv University, 2009.
- [2] P. Meakin and B. Jamtveit. Geological pattern formation by growth and dissolution in aqueous systems. *Proc. Roy. Soc. A*, 466(2115):659–694, 2010.
- [3] B. Jamtveit and Ø. Hammer. Sculpting of rocks by reactive fluids. *Geochem. Persp.*, 1(3):341–342, 2012.
- [4] I. Morawiecka and P. Walsh. A study of solution pipes preserved in the Miocene limestones (Staszów, Poland). *Acta Carsologica*, 20:337–350, 1997.
- [5] P. Walsh and I. Morawiecka-Zacharz. A dissolution pipe palaeokarst of mid-Pleistocene age preserved in Miocene limestones near Staszów, Poland. *Palaeogeography, Palaeoclimatology, Palaeoecology*, 174(4):327–350, 2001.
- [6] R.J. Schaetzl and S. Anderson. *Soils: Genesis and Geomorphology*. Cambridge University Press, 2005.
- [7] E. Merino and A. Canals. Self-accelerating dolomite-for-calcite replacement: Self-organized dynamics of burial dolomitization and associated mineralization. *Am. J. Sci.*, 311:572–607, 2011.
- [8] A. Beinlich, O. Plümper, J. Hövelmann, H. Austrheim, and B. Jamtveit. Massive serpentine carbonation at Linnajavri, N-Norway. *Terra Nova*, 24(6):446–455, 2012.
- [9] A. Putnis. Mineral Replacement Reactions. *Rev. Mineral. Geochem.*, 70(1):87–124, 2009.
- [10] A. Hofmann. Chromatographic theory of infiltration metasomatism and its application to feldspars. *Am. J. Sci.*, 272(1):69–90, 1972.
- [11] P. Ortoleva, G. Auchmuty, J. Chadam, J. Hettmer, E. Merino, C.H. Moore, and E. Ripley. Redox front propagation and banding modalities. *Physica D*, 19:334–354, 1986.
- [12] M. Bickle and J. Baker. Migration of reaction and isotopic fronts in infiltration zones: assessments of fluid flux in metamorphic terrains. *Earth Planet. Sci. Lett.*, 98(1):1–13, 1990.
- [13] L.W. Lake, S.L. Bryant, and A.N. Araque-Martinez. *Geochemistry and Fluid Flow*. Elsevier, 2002.
- [14] G. Daccord and R. Lenormand. Fractal patterns from chemical dissolution. *Nature*, 325:41–43, 1987.
- [15] M.L. Hoefner and H.S. Fogler. Pore evolution and channel formation during flow and reaction in porous media. *AIChE J.*, 34:45–54, 1988.

- [16] P. Ortoleva, J. Chadam, E. Merino, and A. Sen. Geochemical Self-Organization II: The Reactive-Infiltration Instability. *Amer. J. Sci.*, 287(10):1008–1040, 1987.
- [17] J.N. Jennings. *Karst geomorphology*. Blackwell Oxford, 1985.
- [18] A.N. Palmer. Origin and morphology of limestone caves. *Geol. Soc. Am. Bull.*, 103:1–21, 1991.
- [19] A.W. Woods. *Flow in Porous Rocks*. Cambridge University Press, 2014.
- [20] P.C. Lichtner and N. Waber. Redox front geochemistry and weathering : theory with application to the Osamu Utsumi uranium mine. *J. Geochem. Exploration*, 45:521–564, 1992.
- [21] J.N. Dewynne, A.C. Fowler, and P.S. Hagan. Multiple Reaction Fronts in the Oxidation-Reduction of Iron-Rich Uranium Ores. *SIAM J. Appl. Math.*, 53(4):971–989, 1993.
- [22] M. Wangen. Stability of reaction-fronts in porous media. *Appl. Math. Model.*, 37(7):4860–4873, 2013.
- [23] H. Darcy. *Les fontaines publiques de la ville de Dijon*. 1856.
- [24] O.M. Phillips. *Geological fluid dynamics: sub-surface flow and reactions*. Cambridge University Press, 2009.
- [25] E. Boeker and R. Van Grondelle. *Environmental physics: sustainable energy and climate change*. John Wiley & Sons, 2011.
- [26] J. Bear. *Dynamics of fluids in porous media*. Courier Corporation, 2013.
- [27] C. Noiriél, B. Madé, and P. Gouze. Impact of coating development on the hydraulic and transport properties in argillaceous limestone fracture. *Water Resources Res.*, 43(9), 2007. W09406.
- [28] J. Kozeny. About capillaries conducting water in the earth. *Sitzber. Akd. Wiss. Wien, Math. Naturv. Kasse*, 136:271–306, 1927.
- [29] E. J. Hinch and B. S. Bhatt. Stability of an acid front moving through porous rock. *J. Fluid Mech.*, 212(-1):279, 1990.
- [30] S. Whitaker. Diffusion and dispersion in porous media. *AIChE J.*, 13(3):420–427, 1967.
- [31] A.E. Scheidegger. General theory of dispersion in porous media. *J. Geophys. Res.*, 66(10):3273–3278, 1961.
- [32] F. Golfier, C. Zarcone, B. Bazin, R. Lenormand, D. Lasseux, and M. Quintard. On the ability of a Darcy-scale model to capture wormhole formation during the dissolution of a porous medium. *J. Fluid Mech.*, 457:213–254, 2002.
- [33] A.C. Lasaga. Chemical kinetics of water-rock interactions. *J. Geophys. Res.*, 89(B6):4009–4025, 1984.
- [34] A.C. Lasaga. *Kinetic Theory in the Earth Sciences*. Princeton University Press, 2014.
- [35] J.L. Palandri and Y.K. Kharaka. A compilation of rate parameters of water-mineral interaction kinetics for application to geochemical modeling. Technical report, DTIC Document, 2004.

- [36] A.A. Jeschke, K. Vosbeck, and W. Dreybrodt. Surface controlled dissolution rates of gypsum in aqueous solutions exhibit nonlinear dissolution kinetics. *Geochim. Cosmochim. Acta*, 65(1):27–34, 2001.
- [37] J. Colombani and J. Bert. Holographic interferometry study of the dissolution and diffusion of gypsum in water. *Geochim. Cosmochim. Acta*, 71(8):1913–1920, 2007.
- [38] A.A. Jeschke and W. Dreybrodt. Dissolution rates of minerals and their relation to surface morphology. *Geochim. Cosmochim. Acta*, 66(17):3055–3062, 2002.
- [39] P. Kondratiuk, H. Tredak, A.J.C. Ladd, and P. Szymczak. Synchronization of dissolution and precipitation fronts during infiltration-driven replacement in porous rocks. *Geophys. Res. Lett.*, 42(7):2244–2252, 2015.
- [40] P. Szymczak and A.J.C. Ladd. Reactive infiltration instabilities in rocks. Part 2. Dissolution of a porous matrix. *J. Fluid Mech.*, 738:591–630, 2014.
- [41] F. Osselin, P. Kondratiuk, A. Budek, O. Cybulski, P. Garstecki, and P. Szymczak. Microfluidic observation of the onset of reactive-infiltration instability in an analog fracture. *Geophys. Res. Lett.*, 43:6907–6915, 2016.
- [42] P. Szymczak and A.J.C. Ladd. Interacting length scales in the reactive-infiltration instability. *Geophys. Res. Lett.*, 40(12):3036–3041, 2013.
- [43] J. Chadam, D. Hoff, E. Merino, P. Ortoleva, and A. Sen. Reactive infiltration instabilities. *IMA J. Appl. Math.*, 36(3):207–221, 1986.
- [44] C. Noiriel, P. Gouze, and D. Bernard. Investigation of porosity and permeability effects from microstructure changes during limestone dissolution. *Geophys. Res. Lett.*, 31(24), 2004. L24603.
- [45] J. Chadam, P. Ortoleva, and A. Sen. A Weakly Nonlinear Stability Analysis of the Reactive Infiltration Interface. *SIAM J. Appl. Math.*, 48(6):1362–1378, 1988.
- [46] Y. Huang, G. Ouillon, H. Saleur, and D. Sornette. Spontaneous generation of discrete scale invariance. *Phys. Rev. E*, 55(6):6433–6447, 1997.
- [47] J.A. Miranda and M. Widom. Weakly nonlinear investigation of the Saffman-Taylor problem in a rectangular Hele-Shaw cell. *Int. J. Mod. Phys. B*, 12(9):42, 1998.
- [48] N. Kalia and V. Balakotaiah. Modeling and analysis of wormhole formation in reactive dissolution of carbonate rocks. *Chem. Eng. Sci.*, 62(4):919 – 928, 2007.
- [49] P. Maheshwari, R.R. Ratnakar, N. Kalia, and V. Balakotaiah. 3-d simulation and analysis of reactive dissolution and wormhole formation in carbonate rocks. *Chem. Eng. Sci.*, 90:258–274, 2013.
- [50] K.M. Hung, A.D. Hill, and K. Spehrnoori. A mechanistic model of wormhole growth in carbonate acidizing and acid fracturing. *J. Pet. Tech.*, 41:59–66, 1989.
- [51] M.A. Buijse. Understanding wormholing mechanisms can improve acid treatments in carbonate formations. *SPE Prod. and Facilities*, 8:168–175, 2000.
- [52] C. Cohen, D. Ding, M. Quintard, and B. Bazin. From pore scale to wellbore scale: Impact of geometry on wormhole growth in carbonate acidization. *Chem. Eng. Sci.*, 63:3088–3099, 2008.

- [53] R.H. Nilson and S.K. Griffiths. Wormhole growth in soluble porous materials. *Phys. Rev. Lett.*, 65(13):1583–1586, 1990.
- [54] S.D. Howison. A note on the two-phase Hele-Shaw problem. *J. Fluid. Mech.*, 409:243–249, 2000.
- [55] D.G. Crowdy. Exact solutions to the unsteady two-phase Hele-Shaw problem. *Quart. J. Mech. Appl. Math.*, 59(4):475–485, 2006.
- [56] E. Nakouzi, R.E. Goldstein, and O. Steinbock. Do dissolving objects converge to a universal shape? *Langmuir*, 31(14):4145–4150, 2014.
- [57] L.M. Cummings, Yu.E. Hohlov, S.D. Howison, and K. Kornev. Two-dimensional solidification and melting in potential flows. *J. Fluid Mech.*, 378:1–18, 1999.
- [58] P. Kondratiuk and P. Szymczak. Steadily translating parabolic dissolution fingers. *SIAM J. Appl. Math.*, 75(5):2193–2213, 2015.
- [59] G.P. Ivantsov. Temperature field around a spheroidal, cylindrical and acicular crystal growing in a supercooled melt. *Dokl. Akad. Nauk SSSR*, 58:567, 1947.
- [60] M. Adda-Bedia and M. Ben Amar. Investigations on the dendrite problem at zero surface tension in 2D and 3D geometries. *Nonlinearity*, 7(3):765, 1994.
- [61] M.Z. Bazant, J. Choi, and B. Davidovitch. Dynamics of conformal maps for a class of non-Laplacian growth phenomena. *Phys. Rev. Lett.*, 91(4):045503, 2003.
- [62] M. Z. Bazant. Conformal mapping of some non-harmonic functions in transport theory. *Proc. Roy. Soc. A*, 460(2045):1433–1452, 2004.
- [63] J. Choi, D. Margetis, T.M. Squires, and M.Z. Bazant. Steady advection-diffusion around finite absorbers in two-dimensional potential flows. *J. Fluid Mech.*, 536:155–184, 2005.
- [64] V.A. Maksimov. On the determination of the shape of bodies formed by solidification of the fluid phase of the stream: PMM vol. 40, no. 2, 1976, pp. 289–297. *J. Appl. Math. Mech.*, 40(2):264–272, 1976.
- [65] M.E. Goldstein and R.L. Reid. Effect of fluid flow on freezing and thawing of saturated porous media. *Proc. R. Soc. Lond. A Mat.*, 364(1716):45–73, 1978.
- [66] K. Kornev and G. Mukhamadullina. Mathematical theory of freezing for flow in porous media. *Proc. R. Soc. Lond. A Mat.*, 447(1930):281–297, 1994.
- [67] L.J. Cummings and K. Kornev. Evolution of flat crystallisation front in forced hydrodynamic flow—some explicit solutions. *Physica D*, 127(1):33–47, 1999.
- [68] M.Z. Bazant. Interfacial dynamics in transport-limited dissolution. *Phys. Rev. E*, 73(6):060601, 2006.
- [69] A.R. Kacimov and Yu.V. Obnosov. Steady water flow around parabolic cavities and through parabolic inclusions in unsaturated and saturated soils. *J. Hydrol.*, 238(1-2):65–77, 2000.
- [70] S.D. Poisson. *Second mémoire sur la théorie du magnétisme*. Imprimerie Royale, 1825.
- [71] J.C. Maxwell. *A treatise on electricity and magnetism*, volume 2. Clarendon Press, Oxford, 1881.

- [72] H.S. Carslaw and J.C. Jaeger. *Heat in solids*. Clarendon Press, Oxford, 1959.
- [73] E. Jońca. Studnie krasowe w Smerdynie. *Czasopismo Geograficzne*, 34:61–66, 1963.
- [74] J. Dzierżek. *Paleogeografia wybranych obszarów Polski w czasie ostatniego zlodowacenia*, volume 95 of *Acta Geographica Lodziensia*. Łódzkie Tow. Naukowe, 2009.
- [75] S.N. Ehrenberg, G.P. Eberli, M. Keramati, and S.A. Moallemi. Porosity-permeability relationships in interlayered limestone-dolostone reservoirs. *AAPG Bulletin*, 90(1):91–114, 2006.
- [76] L. Jonas, T. Müller, R. Dohmen, L. Baumgartner, and B. Putlitz. Transport-controlled hydrothermal replacement of calcite by Mg-carbonates. *Geology*, 43(9):779–783, 2015.
- [77] B. Jamtveit, M. Krotkiewski, M. Kobchenko, F. Renard, and L. Angheluta. Pore-space distribution and transport properties of an andesitic intrusion. *Earth Planet. Sci. Lett.*, 400:123–129, 2014.
- [78] J.P. Boyd. Orthogonal rational functions on a semi-infinite interval. *J. Comp. Phys.*, 88:63–88, 1987.
- [79] J.P. Boyd. *Chebyshev and Fourier Spectral Methods*. Dover Publications, Inc., 2000.
- [80] A. De Wit, Y. Bertho, and M. Martin. Viscous fingering of miscible slices. *Phys. Fluids*, 17(5):054114, 2005.
- [81] M. Mishra, M. Martin, and A. De Wit. Differences in miscible viscous fingering of finite width slices with positive or negative log-mobility ratio. *Phys. Rev. E.*, 78(6):066306, 2008.
- [82] P. Daripa. Studies on stability in three-layer hele-shaw flows. *Phys. Fluids*, 20(11):112101, 2008.
- [83] S. Pramanik and M. Mishra. Viscosity scaling of fingering instability in finite slices with Korteweg stress. *EPL*, 109(6):64001, 2015.
- [84] H.J. Catchpoole, R.A. Shalliker, G.R. Dennis, and G. Guiochon. Visualising the onset of viscous fingering in chromatography columns. *J. Chromatogr. A*, 1117(2):137–145, 2006.
- [85] R.A. Shalliker, H.J. Catchpoole, G.R. Dennis, and G. Guiochon. Visualising viscous fingering in chromatography columns: high viscosity solute plug. *J. Chromatogr. A*, 1142(1):48–55, 2007.
- [86] I. Sharp, P. Gillespie, D. Morsalnezhad, C. Taberner, R. Karpuz, J. Verges, A. Horbury, N. Pickard, J. Garland, and D. Hunt. Stratigraphic architecture and fracture-controlled dolomitization of the Cretaceous Khami and Bangestan groups: an outcrop case study, Zagros Mountains, Iran. *Geol. Soc., London, Special Publications*, 329(1):343–396, 2014.
- [87] G. Horvay and J.W. Cahn. Dendritic and spheroidal growth. *Acta Metall.*, 9(7):695–705, 1961.
- [88] P. Pelcé. *New visions on form and growth: fingered growth, dendrites, and flames*. Oxford University Press, 2004.
- [89] A. Banerjee and E. Merino. Terra Rossa Genesis by Replacement of Limestone by Kaolinite. III. Dynamic Quantitative Model. *J. Geol.*, 119(3):259–274, 2011.

- [90] P. Kondratiuk, H. Tredak, V. Upadhyay, A.J.C. Ladd, and P. Szymczak. Instabilities and finger formation in mineral replacement fronts due to localized porosity increase. Submitted to *J. Geophys. Res. Solid Earth*, 2017.
- [91] P. Szymczak and A.J.C. Ladd. Reactive-infiltration instabilities in rocks. Fracture dissolution. *J. Fluid Mech.*, 702:239–264, 2012.

# Appendix A

## Spectral method

In Sec. 7.4.2 we have derived the ordinary differential equation (7.68), which, supplied by appropriate boundary conditions allows one to find the dispersion relation between the wavenumber characterizing the sinusoidal perturbation of the reaction front and its growth rate. Eq. (7.68) was valid in the  $\xi > 0$  domain, and the boundary conditions were either set at  $\xi = 0$ , or at  $\xi \rightarrow \infty$ . Similarly, in Sec. 7.4.3 two coupled ODEs (7.124) were derived, one of them valid for  $\xi < 0$ , and another one for  $\xi > 0$ . Those were accompanied by far-field boundary conditions (at  $\xi \rightarrow -\infty$  and  $\xi \rightarrow \infty$ ), as well as by four continuity conditions at  $\xi = 0$ . We have mentioned that these problems cannot be in general solved analytically, and a numerical solution is required. Here, we shall give some more details regarding the applied numerical integration method.

Following Szymczak & Ladd [91], who were studying instabilities in fracture dissolution, we have applied the pseudospectral, boundary-bordering method [78, 79]. In the case of a single ODE valid in the  $\mathcal{R}_+ = (0, \infty)$  domain,

$$\mathcal{H}f(\xi) = 0, \quad \xi > 0, \quad (\text{A.1})$$

where  $\mathcal{H}$  represents a linear differential operator, its solution  $f(\xi)$  is expanded as a linear combination of  $N$  basis functions,

$$f(\xi) = \sum_{j=0}^{N-1} f_j \Psi_j(\xi), \quad (\text{A.2})$$

where  $f_j$  are unknown coefficients. The basis functions are rational Chebyshev polynomials,

$$\Psi_n(\xi) = T_n \left( \frac{\xi - L}{\xi + L} \right), \quad (\text{A.3})$$

where  $T_n(t)$ , with  $n = 0, 1, 2, \dots$ , is a Chebyshev polynomial of the first kind, and  $L > 0$  is a parameter. By variable change one can show that rational Chebyshev polynomials are orthogonal with respect to the weight  $\frac{\sqrt{L}}{\sqrt{\xi}(\xi + L)}$ , and with the inner product equivalent to integration over  $(0, \infty)$ ,

$$\int_0^{\infty} \Psi_i(\xi) \Psi_j(\xi) \frac{\sqrt{L} d\xi}{\sqrt{\xi}(\xi + L)} = \int_{-1}^1 T_i(t) T_j(t) \frac{dt}{\sqrt{1-t^2}} = \begin{cases} 0, & i \neq j, \\ \pi/2, & i = j \neq 0, \\ \pi, & i = j = 0. \end{cases} \quad (\text{A.4})$$

The  $f_j$  coefficients in Eq. (A.2) can be found by solving a linear system

$$\mathbf{H}\mathbf{f} = \mathbf{g}, \quad (\text{A.5})$$

where  $\mathbf{f} = [f_0, \dots, f_{N-1}]^T$ , and  $\mathbf{H}$  is a real  $N \times N$  matrix. The first  $b$  rows of  $\mathbf{H}$  are used to impose  $b$  boundary conditions at  $\xi = 0$ , which are sufficient to solve the problem (in our case  $b = 3$ ). The boundary conditions, which are of the form

$$\mathcal{B}_i f|_{\xi=0} = \alpha_i, \quad i = 0, 1, \dots, b-1, \quad (\text{A.6})$$

where  $\mathcal{B}_i$  are linear differential operators, are thus translated into  $b$  rows of  $\mathbf{H}$  and  $\mathbf{g}$ ,

$$H_{ij} = \mathcal{B}_i \Psi_j(\xi)|_{\xi=0}, \quad g_i = \alpha_i, \quad i = 0, 1, \dots, b-1. \quad (\text{A.7})$$

The remaining matrix elements are found by evaluating  $\mathcal{H}$  acting on the basis functions,

$$H_{i+b,j} = \mathcal{H} \Psi_j(\xi)|_{\xi=\xi_i}, \quad g_{i+b} = 0; \quad i = 0, \dots, N-1-b; \quad j = 0, \dots, N-1; \quad (\text{A.8})$$

where  $\xi_i$  are preselected collocation points,

$$\xi_i = L \cot^2 \left( \frac{\pi(2i+1)}{4(N-b)} \right), \quad i = 0, 1, \dots, N-1-b. \quad (\text{A.9})$$

After solving (A.5) for  $\mathbf{f}$ , the last boundary condition at  $\xi = 0$ ,

$$\mathcal{B}_b f(\xi)|_{\xi=0} = \alpha_b, \quad (\text{A.10})$$

can be used to find the dispersion relation. In practice, one should vary the growth rate  $\hat{\sigma}$  until the discretized version of Eq. (A.10),

$$\sum_{j=0}^{N-1} f_j \mathcal{B}_b \Psi_j(\xi)|_{\xi=0} = \alpha_b, \quad (\text{A.11})$$

is satisfied.

Note that boundary conditions at  $\xi \rightarrow \infty$  are not explicitly used in this numerical method. As one can strictly prove, the general asymptotic solution of  $f(\xi)$  is a linear combination of exponentially growing and exponentially decaying functions, the former to be cut off by boundary conditions at  $\xi \rightarrow \infty$ . Thus, since

$$\lim_{\xi \rightarrow \infty} \Psi_n(\xi) = 1 < \infty, \quad (\text{A.12})$$

the boundary conditions at infinity can be automatically satisfied by the choice of basis functions. However, one has to assure that the solutions which are singular at  $\xi \rightarrow \infty$  are automatically cut off for all parameters, and it might be necessary to modify the problem a bit, replacing the  $f(\xi)$  function by a product of another unknown function  $\bar{f}(\xi)$  and an exponential factor<sup>1</sup>. An asymptotic analysis of Eq. (7.68) reveals that in order to satisfy the latter, one should rather search for  $\bar{f}_{v_P}(\xi) = e^{\Lambda \xi} f_{v_P}(\xi)$  instead of the original function  $f_{v_P}(\xi)$ .

<sup>1</sup> For instance, consider the following problem,

$$(\partial_\xi^2 - u^2)e^\xi f(\xi) = 0, \quad \xi > 0, \quad (\text{A.13a})$$

$$f(\xi = 0) = 1, \quad (\text{A.13b})$$

$$\lim_{\xi \rightarrow \infty} e^\xi f(\xi) = 0, \quad (\text{A.13c})$$

where  $u$  is a positive parameter. The general solution of Eq. (A.13a) is

$$f(\xi) = C_1 e^{-(u+1)\xi} + C_2 e^{(u-1)\xi}. \quad (\text{A.14})$$

The boundary condition (A.13c) sets  $C_2 = 0$ , and then (A.13b) yields  $C_1 = 1$ . However, for  $u < 1$  both parts of solution (A.14) are exponentially decreasing, and neither of them can be cut off choosing rational Chebyshev

A similar method can be used to solve Eqs. (7.124). Here, however, the problem is a bit more complicated, since two coupled differential equations,

$$\mathcal{H}^- f^-(\xi) = 0, \quad \xi < 0, \quad (\text{A.16})$$

$$\mathcal{H}^+ f^+(\xi) = 0, \quad \xi > 0, \quad (\text{A.17})$$

have to be solved simultaneously. The basis functions are rational Chebyshev polynomials (A.3) as well, but one has to take a positive  $L$  to expand  $f^+$ , and a negative one for  $f^-$ . In vector  $\mathbf{f}$ , the coefficients of the expansion of both  $f^-$  and  $f^+$  are stacked,

$$\mathbf{f} = [f_0^-, \dots, f_{N^- - 1}^-, f_0^+, \dots, f_{N^+ - 1}^+]^T, \quad (\text{A.18})$$

and the  $\mathbf{H}$  matrix consists of several submatrices,

$$\mathbf{H} = \begin{bmatrix} \mathbf{B}^- & \mathbf{B}^+ \\ \mathbf{H}^- & \mathbf{0} \\ \mathbf{0} & \mathbf{H}^+ \end{bmatrix}, \quad (\text{A.19})$$

where the  $R^\pm \times N^\pm$  matrices  $\mathbf{H}^\pm$  are discretized  $\mathcal{H}^\pm$  operators, and  $b \times N^\pm$  matrices  $\mathbf{B}^\pm$  originate from  $b$  continuity conditions at  $\xi = 0$ , which are of the form

$$\mathcal{B}_i^- f^-(\xi) + \mathcal{B}_i^+ f^+(\xi) = \alpha_i, \quad i = 0, 1, \dots, b - 1. \quad (\text{A.20})$$

There is some freedom in choosing the sizes of the submatrices, but one has to make sure that

$$R^- + R^+ + b = N^- + N^+, \quad (\text{A.21})$$

so that  $\mathbf{H}$  is a square matrix.

Again, the boundary conditions at  $\xi \rightarrow \pm\infty$  are automatically satisfied, if one modifies the original problem a bit. In both the ODEs (7.124) and the continuity conditions,  $f_{v_S}^-$  should be replaced by  $e^{\Gamma_1^+ \xi} \bar{f}_{v_S}^-$ , and  $f_{v_S}^+$  by  $e^{-\Gamma_1 \xi} \bar{f}_{v_S}^+$ .

In our case, 40–50 base functions for each ODE were typically sufficient to obtain the desired accuracy. The parameter  $L$  is in principle arbitrary, but the method proved to be least error-prone for  $L = 5$  or  $L = 10$  ( $L = -5, -10$  for the negative domain). Taking larger  $N$  and  $L$  was sometimes necessary to resolve the long-wave ( $\hat{k} \gtrsim 0$ ) part of a dispersion curve.

---

polynomials as basis functions. A slight modification of problem (A.13) is necessary: the unknown function  $f(\xi)$  has to be replaced by  $e^{-\xi} \bar{f}(\xi)$ . A problem equivalent to (A.13) is then constructed,

$$(\partial_\xi^2 - u^2) \bar{f}(\xi) = 0, \quad \xi > 0, \quad (\text{A.15a})$$

$$\bar{f}(\xi = 0) = 1, \quad (\text{A.15b})$$

$$\lim_{\xi \rightarrow \infty} \bar{f}(\xi) = 0, \quad (\text{A.15c})$$

which can be solved by the presented numerical method.